Controlling Local Quantum Fluctuations of Light Using Four-Wave Mixing in an Atomic Vapour

by

Christopher Embrey

A thesis submitted to
The University of Birmingham
for the degree of
DOCTOR OF PHILOSOPHY

Ultracold Atoms Group
School of Physics and Astronomy
College of Engineering and Physical Sciences
The University of Birmingham

July 2015

Abstract

Light is used in many measurement systems. These measurement systems are often limited in precision by the quantum noise present in all light. This quantum noise is imposed by the Heisenberg uncertainty principle. The principle governs the total noise on the phase and amplitude, called quadratures, of a light field. The limit imposed on the precision of measurements by the quantum noise is generally known as the quantum noise limit (QNL). The noise of one quadrature of a light field can be reduced at the expense of the noise on the other quadrature, a process known as squeezing. The use of squeezed light can greatly improve the accuracy of many measurements.

This work introduces the theory behind the generation of squeezed light, both in two mode squeezed states (TMSSs) and single mode squeezed states (SMSSs). This work explains how the properties of squeezed states can be described by correlations between quantum fluctuations, and how such properties can be measured using a homodyne detector, with either a monochromatic or bichromatic local oscillator (MLO or BLO).

This work employs a four-wave mixing (4WM) gain process that to experimentally generate squeezed light. The 4WM process produces correlations between the quantum fluctuations of a probe and conjugate field, separated in frequency by approximately 6 GHz, generating a squeezed light state. The thesis investigates the properties of this squeezed light, through the use of homodyne detection with a BLO. The thesis further investigates how the squeezed quadrature changes from amplitude to phase over a range of 40 MHz.

The spatial character of the noise on a light field affects its usefulness both for imaging purposes and for quantum information transport. The reduction of noise, across multiple spatial modes, has long been an experimental goal within the field of quantum optics. However, attempts to generate such light experimentally have met with only limited success. Such multi-spatial-mode (MSM) squeezed light can significantly improve the properties of an imaging system, and can be used for improved resolution imaging, below the QNL.

This work progresses to focus on the direct investigation of the MSM nature of a squeezed light field generated through the 4WM process. The field is shown to contain at least 75 squeezed spatial modes in the frequency domain, each squeezed at a level of up to -2.5 dB. The thesis continues to develop techniques to measure the fluctuations on a light field in the time domain. The fluctuations are calculated over a series of images. The fluctuations of a coherent light source are measured at the shotnoise level, and the extra noise introduce through a 4WM gain process is investigated. The technique is shown to be a promising candidate for investigating the MSM nature of a squeezed light field in the time domain.

ACKNOWLEDGEMENTS

I would like to thank the University of Birmingham for providing the funding for my studies, allowing me the opportunity to investigate the properties of multi-spatial-mode squeezed light, as reported in this thesis. I would like to thank my supervisor Dr. Vincent Boyer for his direction and help throughout my studies. I would also like to thank the squeezing project team for their ongoing help, and the wider Cold Atoms research group for many interesting discussions, and helpful ideas.

Additionally, I would like to thank my family and friends for their help and support throughout this work. I would like to acknowledge the physics teachers at King Edward VI Aston School for inspiring my interest in physics, and starting me down this path.

Finally, I acknowledge the work that Alexander Franzen has put in to create the optical component symbol library that I have used in the experimental diagrams. The library can be found on the web at `http://www.gwoptics.org/ComponentLibrary`.

Acronym	Meaning
AOM	Acousto-Optical Modulator
BLO	Bichromatic Local Oscillator
CCD	Charge-Coupled Device
EIT	Electromagnetically Induced Transparency
FF	Far Field
LO	Local Oscillator
MLO	Monochromatic Local Oscillator
MSM	Multi-Spatial Mode
NEP	Noise Ellipse Phase
NF	Near Field
PDC	Parametric Down Conversion
QNL	Quantum Noise Limit
QNR	Quantum Noise Reduction
RF	Radio Frequency
RGR	Restricted Gain Region
SMSS	Single Mode Squeezed State; here mode refers to the propagation mode
SN	Shot Noise
SQL	Standard Quantum Limit
SSM	Single Spatial Mode
TMSS	Two Mode Squeezed State; here mode refers to the propagation mode
4WM	Four Wave Mixing

Table 1: Table of acronyms

CONTENTS

LIST OF FIGURES

LIST OF TABLES

CHAPTER 1

INTRODUCTION

The scientific community is constantly searching for more accurate measurement methods [1]. Some key areas of progress have been improvements in time measurements with experiments running atomic clocks [2–4], improved gravity measurements with atom interferometry [5], and the struggle to improve the accuracy of detectors in an attempt to measure gravitational waves [6–9]. Experiments in many fields rely on complex imaging systems, with results being limited by the resolution of the system in use. A significant amount of work has been done in improving these imaging systems with complex optical designs and post-processing to beat the diffraction limit [10–16]. In fact, the area of imaging with improved resolution is of such interest and importance that the 2014 Nobel prize for chemistry was awarded to Erik Betzig, Stefan W. Hell and W. E. Moerner for their work on development of super-resolution fluorescence microscopy [17].

Fundamentally all of these experiments are limited by noise. They are either nearing, or are already at, the uncertainty limits imposed by quantum mechanics. In 1927 Heisenberg introduced this concept of a quantum mechanical limit to the minimum level of noise obtainable [18], known as the uncertainty principle. Later that year Kennard derived the formal inequality [19]. However the inequality only requires that the total noise on two non-commuting operators $(\hat{A}, \hat{B})$ is larger than half their commutator $\Delta\hat{A}\Delta\hat{B} \geq \frac{1}{2}\left|\left[\hat{A}, \hat{B}\right]\right|$ [20]. This statement theoretically allows the reduction of noise on one observable at the expense of an increased noise on the other observable, a process known as squeezing [21].

In the case of light, its quadratures are the operators that are confined by the Uncertainty Principle. When the quadratures are of equal noise, and the inequality is saturated, the light field is said to be at the quantum noise limit (QNL) [22]. An example of such light is a perfect coherent field, produced by an ideal laser. In 1976 Kimble [23] and Carmichael [24] independently proposed the idea of photon anti-bunching, corresponding to a reduction in the time variance of photon number, and in 1977 Kimble experimentally

demonstrated this phenomenon [25]. The interest in this area continued with Reid proposing the idea of producing squeezing through atomic coherence in 1985 [26]. Squeezing was experimentally observed shortly afterwards, using four-wave mixing (4WM) in sodium vapour [27].

As work continued, in 1987 Maeda measured reductions in noise of 4% [28], and Raizen measured improved reductions at 30% [29]. At a similar time, investigations began into generating squeezed light with parametric down conversion (PDC). In 1986 Wu et al. saw reductions in quantum mechanical fluctuations of 65% [30].

The majority of squeezed light sources employ nonlinear crystals to achieve PDC following a similar design to Wu's experiment. Such systems act as a phase preserving amplifier and produce a pair of twin entangled light fields with a very low gain. The twin entangled fields can be converted into a single squeezed field by the use of a beam splitter. The low gain of such sources (section 3.3) means that their use in free space is confined to the single photon regime.

In order for PDC crystals to be used in the continuous variable regime, the gain must be increased by the use of a cavity. This increase in gain also increases the entanglement and consequently the squeezing proportionally. After these early measurements of squeezed light were made, the flood gates opened and many groups began experimental studies producing squeezing at ever increasing levels, culminating in the current best squeezing measurements of 12.7dB in light of wavelength 532nm by Eberle [31], and 12.3dB in 1550nm light by Mehment [32].

In the early 1980s there was some discussion on the time fluctuations of interferometric signals. At this time, it was suggested the interferometric signal could be stabilised by coupling in a squeezed state on the unused input port to the interferometer [33]. This has been somewhat successful, and is in constant use in gravitational waves detectors [8, 31, 34, 35]. However the interferometers were found to be limited by the radiation pressure noise at low frequencies, and by photon shotnoise (SN) at high frequencies [36]. A conventional quadrature squeezed field reduces the radiation pressure noise at the expense of photon SN, or vice versa. As such, applying a conventional quadrature squeezed field cannot reduce the noise limit at all frequencies.

In 1983 Unruh proposed that an interferometer might be made to display reduced quantum noise at many frequencies [37]. This requires that a squeezing source could be found where the squeezed quadrature changes with the frequency of the light; the phase noise should be reduced at low frequencies, and the amplitude noise reduced at high frequencies. The concept of quantum limits on the stability of an interferometry measurement was further discussed in the 1990s [6, 38]. In 2001 Kimble et al. analysed the effect of using quantum states of light as inputs to various interferometers [39]. Since then, there have been proposals made by various groups

based on the use of pre-filtering cavities, as proposed by Kimble [40–42]. In 2013 Horrom et al. demonstrated an example of frequency dependent phase rotation using EIT [43]. In 2013 Corzo et al. investigated a 4WM system, inferring the angle of the squeezed noise ellipse generated [44], and indicated a change of squeezed quadrature with frequency. In this paper, the authors lock the relative phase of a local oscillator (LO) and a squeezed vacuum field. They then compare the noise measured with locked phases to that with a scanned LO phase. From this they infer how the squeezed quadrature changes with frequency. In 2014 Chua et al. produced an in depth discussion, including the direct benefits of using such frequency-dependent squeezing over frequency-independent squeezing [9].

In the experimental section (section 4.4) of this thesis, I use 4WM to produce a quadrature squeezed state and directly measure the phase rotation of the frequency components caused by the gain medium. In this way, I evidence the ability to concurrently measure quantum noise reduction (QNR) on the phase quadrature at one frequency, whilst measuring QNR on the amplitude quadrature at a different frequency.

At the present time, there are many groups that have created sources of squeezed light. There are even some groups that have created a compact squeezing source [45–47]. Such squeezing sources can be categorised as either working in the continuous variable regime, or in the single photon regime. However, so far, the majority of the generation and use of squeezed light has been in a single-spatial mode (SSM). In such light any small region within the field will not independently be squeezed. In 1989 Kolobov and Sokolov discussed the possibility of multi-spatial-mode (MSM) squeezed light [48]. A MSM squeezed field is one where any point within the field is independently quadrature squeezed. This paper was the start of studies into MSM squeezed light, where Kolobov and Sokolov continued with further works [49–51].

In 1991 Irani studied super-resolution techniques [52], and found that many of the techniques are not very effective when high levels of noise are present. This led to a great interest in the use of squeezed light to reduce this noise, and hence to improve image resolution, and image reconstruction. To be useful for such imaging purposes, a squeezed state of light must be made up of many independently quadrature squeezed modes, such as those states proposed by Kolobov and Sokolov.

There are two main types of experiment that have been under significant investigation. The first technique is useful for imaging faint objects in the photon counting regime, proposed by Kolobov in 1993 using entangled light from PDC [53]. It relies upon the use of MSM entangled fields at the single photon level, where the correlations between the two images allow for imaging below the QNL.

In 2004 Sokolov and Kolobov proposed a source of MSM entanglement light suitable for superresolving microscopy [54]. Since then, there have many reported measurements of such MSM entangled photons. These

began in 2004 with work by Jedrkiewicz [55], and progressed with many further measurements [56–61].

In 2008 Brambilla proposed a similar scheme for super-resolution [62]. In 2009 and 2010 Brida used this very scheme to measure correlations using a charge-couple device (CCD) [63, 64], and extended this to show clearly the improvement of this correlation technique over the use of classical light for imaging [65, 66]. A second similar method has been proposed theoretically by Lloyd [67] and Tan [68], and also experimentally investigated by Lopaeva [69]. Further advances have been made in imaging a living cell by Taylor [70], and Lu [71]. In all these cases, entangled photons are used to image weak objects at low light levels.

The second type of super resolution involves the use of bright MSM quadrature squeezed light. In 1999 Kolobov [51] considered the spatial effects within a single quadrature squeezed field. In 2000 Fabre [72] first considered the possible use of MSM squeezed light for improving resolution. Later Kolobov and Fabre together investigated the quantum limits on super-resolution techniques [73]. In 2008 Kolobov published another work on a similar theme, focusing on the difference between the imaging of the discrete and continuous objects [74]. Since then the interest in the field of improving super-resolution with MSM squeezed light has continued, with many different studies into these techniques. However, despite the availability of MSM entangled light sources, at the single photon level, there has previously been no reported MSM quadrature squeezed light source in the continuous variable regime, where many spatial modes are independently squeezed.

In a PDC system, in order to generate a continuous variable quadrature squeezed state, a cavity is required to increase the gain. This cavity confines the amplifier to operate on only a single spatial mode. In theory these cavities can be made degenerate across multiple spatial modes, and used to generate MSM quadrature squeezed fields. Experimentally this proves difficult, and has only met with limited success. Early achievements were to operate cavities on both the TEM01 and TEM10 [75–78]. In 2011 Chalopin measured squeezing on three spatial modes with a self-imaging cavity [79]. However, a PDC source has not been used to generate continuous variable MSM squeezing, with a large number of modes, and a good level of squeezing.

4WM proves to be a promising alternative to PDC for the production of continuous variable MSM squeezing on bright fields. The main advantage for 4WM comes from the higher levels of gain. Thus there is no need to enclose the gain medium in a cavity. 4WM research has continued in a relatively small number of groups alongside the PDC research. Key achievements have included the initial revival of 4WM experiments by Mccormick et al. in 2007 [80]. The technique has since been used to demonstrate slow light propagation [81]. In 2008 the same system was used to produce entangled images, evidencing the MSM nature of the system [82].

In 2011 Glorieux used a similar system to demonstrate amplitude difference squeezing of 9.2 dB [83],

proving that this technique can be used to generate squeezing nearing the levels achieve by PDC. Quadrature squeezing has also been generated, with QNR of 4 dB [44]. In the same group Corzo et al. measured correlations on a few symmetric spatial modes, leading to a reduced quantum noise [84]. The system has also been used by Marino et al. to generate twin MSM entangled fields [85] and used for an imaging system similar to those proposed by Brambilla [62]. These results show 4WM to be a more promising method of generating bright continuous variable MSM quadrature squeezed light than PDC.

In the experimental section (section 4.5) of this thesis, I use 4WM to produce a quadrature squeezed state and directly characterise its MSM nature. I prove that it contains many arbitrary spatial modes that are independently squeezed. The results have also been published [86].

In 2002 Treps investigated a technique of mixing a squeezed vacuum field with a coherent field, and creating an increased beam pointing stability [87]. In the final chapter of this thesis (chapter 5), I set out work to measure the quantum noise on light in the time domain, using a CCD camera. This allows for a similar experiment, investigating the many spatial modes present in the squeezed field. Such an experiment paves the way for a MSM quadrature squeezed state to be used, in super-resolution systems, to achieve resolution below the QNL.

1.1 Layout of Thesis

In **chapter 2** I will introduce the theory behind the generation of squeezed and entangled light using generic amplifiers, following examples laid out by Kolobov [88]. I will introduce the relationship between squeezed and entangled light. I will also introduce the concepts behind the use of squeezed light for improved image resolution and improved stability of interferometry signals.

Nonlinear optical systems such as PDC and 4WM can be used as the phase preserving amplifiers necessary to generate entanglement. In **chapter 3** I will introduce the theory behind nonlinear optics, and the use of rubidium as a 4WM gain medium. The 4WM medium generates entanglement across probe and conjugate fields separated in frequency by 6 GHz, and has an associated phase matching condition. I will also discuss the complications that arise out of these requirements, and the methods used to detect squeezed light.

In **chapter 4** I shall discuss how the squeezed state is produced experimentally, and the optimisation of the numerous parameters that affect the gain of the 4WM system and the squeezing measured. In **section 4.4** I present an experiment that measures how the squeezed quadrature changes with frequency throughout the squeezing region. In **section 4.5** I present an investigation into the MSM character of the squeezed vacuum field by direct measurement.

In **chapter 5** I discuss the use of a high quantum efficiency camera for imaging the quantum noise. I introduce the control and noise analysis processes necessary to measure the spatial character of the noise by direct comparison of a sequence of images, and to create a spatial spectrum analyser.

In **chapter 6** I conclude the thesis, discussing the significance of the measured results, and the future work for the experiment.

CHAPTER 2

QUANTUM OPTICS AND IMAGING

2.1 Introduction

In this chapter, I will introduce the concepts of quantum optics and squeezed light, further descriptions can be found in the literature [89]. I will introduce single mode squeezed states (SMSS), also called quadrature squeezed states, and two mode squeezed states (TMSS), also called entangled modes, their theoretical generation and their relationship. I will also discuss the difference between thin and thick amplifiers and the implication on the transverse spatial modes of the squeezed states. Finally, I shall elaborate on the use of SSM quadrature squeezed light for improving the accuracy of interferometric measurements, beyond the quantum noise limit (QNL), and the use of MSM quadrature squeezed light for improved resolution imaging, beyond the QNL.

Classically light is treated as electromagnetic waves described by the electric field E, oscillating at a given frequency ω. Light has both amplitude, A, and phase, ϕ. Light sources can either be coherent, eg. a laser, where all light emitted from the source has a single well defined phase, or incoherent, eg. an incandescent bulb, where light is emitted with many phases. A coherent classical field can be described by $E = A\exp^{i(\omega t+\phi)}$, where t is time. Equally, a classical field can be described by quadrature values, X and Y, in the form $E = X\cos\omega t + Y\sin\omega t$. Light can be split into different modes, such modes can be distinguished by wavelength, λ, propagation direction, phase, spatial location and polarisation. In this thesis the modes of the TMSS and SMSS are considered to be primarily defined by spatial location and propagation direction. As such a SMSS is a state where the squeezing exists at a single spatial location and propagation direction, and a TMSS is a state where the squeezing exists across two spatial locations and propagation directions.

A single light field, with a single defined propagation direction and spatial location, can also have its

transverse spatial profile broken down into many spatial modes. There are many equivalent basis sets that can be used to analyse these transverse spatial modes. In particular in laser optics, where cavities have a significant role, light is often split into many Gauss-Hermite modes [90]. An alternative break down of the spatial modes might be into square regions, of a given size, located at a position x, y, such as might be considered for pixels on a camera. The use of these many transverse spatial modes, within a single light field, can allow that light field to be used to image a object. It is the local fluctuations within these many transverse spatial modes that are primarily discussed in this thesis.

Quantum mechanically light is treated as a series of photons. As such, the classical electric field becomes a quantum mechanical operator, $E \rightarrow \hat{E}$. Equivalently In quantum optics the field operator can be replaced by quadrature operators, $\hat{X}$ and $\hat{Y}$, according to

$$\hat{E} = \hat{X} \cos \omega t + \hat{Y} \sin \omega t. \tag{2.1}$$

In turn, the quadrature operators can be expressed in terms of photon creation, $\hat{a}^\dagger$, and annihilation, $\hat{a}$, operators

$$\hat{X} = \frac{1}{2} \left(\hat{a}^\dagger + \hat{a} \right) \tag{2.2}$$

$$\hat{Y} = \frac{i}{2} \left(\hat{a}^\dagger - \hat{a} \right). \tag{2.3}$$

A generalised light field can be represented by its quadrature values on a quadrature diagram, this is also a quasi-probability distribution [91], as shown in figure 2.1(a). This is similar to representing a classical field amplitude and phase on an Argand diagram. In general the phase ϕ is represented by the angle away from the $\hat{X}$ axis, and the amplitude $|\alpha|$ is represented by the length of the line.

Since the absolute phase of a field cannot be measured, a choice of a global phase can be made such that, for a single field, $\left\langle \hat{\phi} \right\rangle = 0$ by definition. This choice maps the $\hat{X}$ and $\hat{Y}$ quadratures into amplitude, $\hat{A}$, and phase, $\hat{\phi}$, quadratures, provided that the field has a large amplitude. These few operators form the basics of the quantum mechanical description of light. In addition to these operators there are a number of practical components that are very important for experimental quantum optics. These components include lenses, used for the manipulation of mode shapes and sizes, mirrors, used for control of field propagation directions, and, perhaps the most important optical component, beam splitters, which can be used to overlap and combine different fields. I will introduce the quantum mechanical description of the beam splitter later in section 2.6.2.

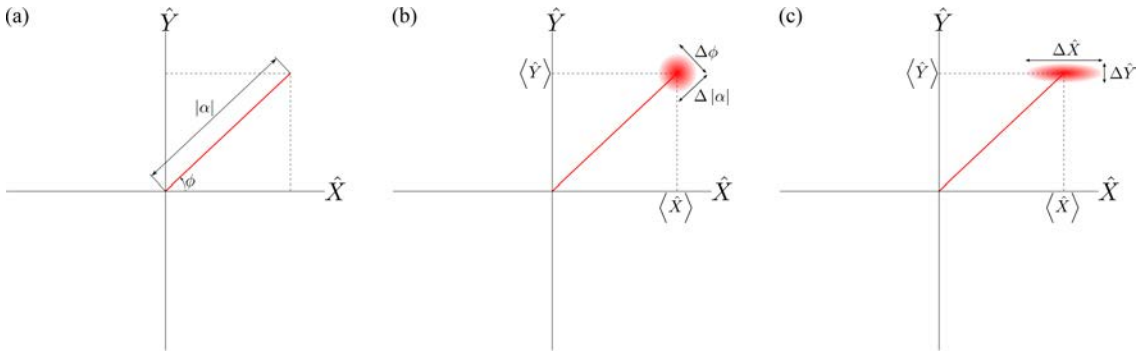

Figure 2.1: The quadrature picture of light. (a) shows a noiseless coherent state. (b) shows a coherent state at the QNL with phase noise $\Delta\phi$ and amplitude noise $\Delta|\alpha|$. The mean value of the quadratures are given by $\left\langle\hat{X}\right\rangle$ and $\left\langle\hat{Y}\right\rangle$. (c) shows a squeezed coherent state, squeezed on the $\Delta\hat{Y}$ quadrature at the expense of excess noise on the $\Delta\hat{X}$ quadrature.

In the rest of this chapter, I will use these quantum mechanical operators to describe the quantum noise on light fields. I will describe the generation of states of light that display reduced quantum noise, and the generation of correlated states of light. Next I will discuss how the length of the medium controls the MSM properties of these states. I will then discuss the similarity between the TMSS and SMSS, and methods to convert one state of light into the other. Finally I will discuss some of the uses of such light, with a particular focus on interferometry and quantum imaging.

2.2 Quantum noise and squeezing

In general the mean value of any observable described by an operator, eg. $\hat{n}$ is given by the expectation value of that operator, eg. $\langle\hat{n}\rangle$. All observables also have some intrinsic fluctuations, which can be found with

$$\left\langle\Delta\hat{n}^2\right\rangle = \left\langle\hat{n}^2\right\rangle - \langle\hat{n}\rangle^2 . \tag{2.4}$$

In a similar way the fluctuations on the quadrature operators can be calculated, as $\left\langle\Delta\hat{X}^2\right\rangle = \left\langle\hat{X}^2\right\rangle - \left\langle\hat{X}\right\rangle^2$ and $\left\langle\Delta\hat{Y}^2\right\rangle = \left\langle\hat{Y}^2\right\rangle - \left\langle\hat{Y}\right\rangle^2$. Here I am interested in the standard deviation rather than the variance, and for ease of writing I define $\Delta\hat{X} = \sqrt{\left\langle\Delta\hat{X}^2\right\rangle}$.

In quantum mechanics, two observables can only be known at the same time if the operators commute. The quadrature operators of a light field do not commute and as such the quadratures must obey a Heisenberg uncertainty relationship, $\Delta\hat{X}\Delta\hat{Y} \geq \frac{1}{4}$, causing all states of light to have a minimum quantum noise. When the inequality is saturated, the state is said to be a minimum uncertainty state. A coherent state is an

example of such a minimum uncertainty state, where the quadrature uncertainties are equal, $\Delta\hat{X} = \Delta\hat{Y} = \frac{1}{2}$. Such a state is said to be at the QNL, and the noise on each quadrature is called the shotnoise (SN). A coherent state, at the QNL, is then represented by a region on the quadrature diagram, of minimum area 1/4, rather than a single point, as shown in figure 2.1(b).

It is possible to improve on the QNL and reduce the noise on one quadrature, say $\Delta\hat{Y} < 1/2$ at the expense of an equal increase in noise on the second quadrature $\Delta\hat{X} = 1/\left(4\Delta\hat{Y}\right) > 1/2$. In this case, the $\hat{Y}$ quadrature is said to display quantum noise reduction (QNR), and the state is said to be squeezed, now appearing as an ellipse on the quadrature diagram (figure 2.1(c)). This is referred to as the noise ellipse. It has a phase defined by the minor axis, called the noise ellipse phase (NEP) in this thesis. Here the state remains a minimum uncertainty state, with the ellipse representing the fluctuations occupying the same area as that of the coherent state.

The QNR is defined as the ratio between the shotnoise, $\mathcal{N}_{sn}$, and the noise of the squeezed quadrature, $\mathcal{N}_{squ}$,

$$\text{QNR} = \frac{\mathcal{N}_{squ}}{\mathcal{N}_{sn}}, \tag{2.5}$$

in general this is reported in logarithmic units (dB), defined as

$$QNR_{dB} = 10\log_{10}\left(\frac{\mathcal{N}_{squ}}{\mathcal{N}_{sn}}\right) \text{ dB}. \tag{2.6}$$

It should be noted that this is not quite the same as the squeezing parameter, s, defined later, due to the difference between the base of the logarithms. Throughout this thesis, the measured QNR will be reported in this way as squeezing or relative noise.

Figure 2.2: A single channel phase-sensitive amplifier that can be used to generate squeezed light.

2.3 Single mode squeezed state generation

Consider a phase sensitive amplifier, with input annihilation and creation operators $\hat{a}$ and $\hat{a}^\dagger$ and output annihilation and creation operators $\hat{b}$ and $\hat{b}^\dagger$, as depicted in figure 2.2. The amplifier performs the operation

$$\hat{b} = U\hat{a} + V\hat{a}^\dagger. \tag{2.7}$$

We choose $U = \cosh s$ and $V = \sinh s$ to ensure that the operation is unitary, ie. that $|U|^2 - |V|^2 = 1$, and s is real and positive, $s > 0$.

Phase sensitive amplifier; coherent state input. Consider the case where the input to the amplifier is a bright coherent state described by $\langle\hat{a}\rangle = \alpha$. In this case the expectation value at the output from the amplifier is

$$\left\langle\hat{b}\right\rangle = \alpha\cosh s + \alpha^*\sinh s. \tag{2.8}$$

When α is real, ie. the phase of the coherent state is 0 or π, and thus $\alpha^* = \alpha$, then the intensity on the output is given by

$$\left|\left\langle\hat{b}\right\rangle\right|^2 = \left|\cosh s + \sinh s\right|^2 \left|\langle\hat{a}\rangle\right|^2 \tag{2.9}$$

$$= e^{2s}\left|\langle\hat{a}\rangle\right|^2. \tag{2.10}$$

When α is imaginary, ie. the phase of the coherent state is $\pm\pi/2$, and thus $\alpha^* = -\alpha$, then the intensity on the output is given by

$$\left|\left\langle\hat{b}\right\rangle\right|^2 = e^{-2s}\left|\langle\hat{a}\rangle\right|^2. \tag{2.11}$$

Thus phase of the input state controls the amplification, and the amplifier is phase-sensitive.

SMSS generator; vacuum state input. When the input state on the amplifier is a vacuum state, $|0\rangle$, then the system can be characterised by its quadratures

$$\hat{X}_{in} = \frac{\hat{a}^\dagger + \hat{a}}{2} \qquad \hat{Y}_{in} = \frac{i\left(\hat{a}^\dagger - \hat{a}\right)}{2} \tag{2.12}$$

$$\hat{X}_{out} = \frac{\hat{b}^\dagger + \hat{b}}{2} \qquad \hat{Y}_{out} = \frac{i\left(\hat{b}^\dagger - \hat{b}\right)}{2}. \tag{2.13}$$

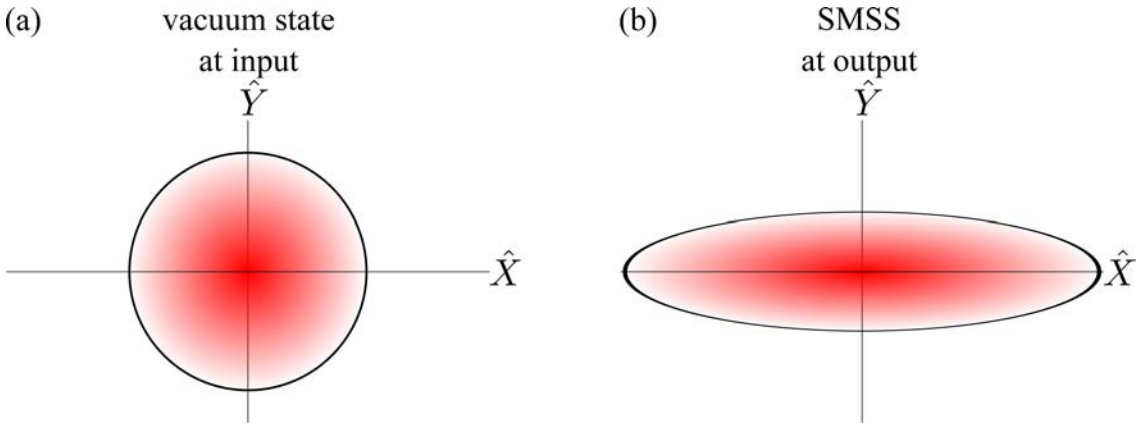

Figure 2.3: The states at the input and output of the phase-sensitive amplifier. (a) shows the input vacuum state, with vacuum fluctuations at the QNL. (b) shows the output squeezed state, with the noise on the $\hat{Y}$ quadrature reduced, at the expense of excess noise on the $\hat{X}$ quadrature.

Using the input/output relationship in equation (2.7), the relationship between $\hat{X}_{in}$ and $\hat{X}_{out}$ can be derived:

$$\hat{X}_{out} = \frac{U\hat{a}^{\dagger} + V\hat{a} + U\hat{a} + V\hat{a}^{\dagger}}{2} \tag{2.14}$$

$$= U\hat{X}_{in} + V\hat{X}_{in} \tag{2.15}$$

$$= e^{s}\hat{X}_{in}, \tag{2.16}$$

and similarly for the $\hat{Y}$ quadratures,

$$\hat{Y}_{out} = e^{-s}\hat{Y}_{in}. \tag{2.17}$$

From these equations it can be seen the $\hat{X}$ quadrature of the input state is amplified, whilst the $\hat{Y}$ quadrature of the state is deamplified. The fluctuations of the quadrature values are similarly amplified ($\Delta\hat{X}_{out} = e^{s}\Delta\hat{X}_{vac}$) and deamplified ($\Delta\hat{Y}_{out} = e^{-s}\Delta\hat{Y}_{vac}$). Figure 2.3(a) shows the input vacuum state at the QNL on a quadrature diagram. The output of such an amplifier is a squeezed vacuum state, also called a SMSS (figure 2.3(b)). In this form, s is defined as the squeezing parameter.

2.4 Two mode squeezed state generation

Classically, the state of all objects can be described independently. Quantum mechanically, it is possible to introduce correlations to a pair, or a group, of objects such that the quantum state of no individual member of the group can be described independently. This pair, or group, of particles can then be said to be entangled. It is possible to entangle the positions, the time of generation, and the polarisation of photons

Figure 2.4: A two channel amplifier, which can be phase sensitive or insensitive dependent on the input. If the input states are vacuum states then the amplifier produces a pair of entangled fields at the output.

or electric fields. In our case we shall consider a system whereby continuous variable entanglement of a pair of light fields is produced. Experimentally this can be evidenced by correlation counting of photon pairs or by intensity correlations in bright fields.

An entangled state can be generated using an amplifier similar to the squeezed state generator (figure 2.2). Such an amplifier must have two input modes and two output modes, as shown in figure 2.4. This amplifier will have a pair of input annihilation operators $\hat{a}_1$ and $\hat{a}_2$ and a pair of output annihilation operators $\hat{b}_1$ and $\hat{b}_2$. The amplifier must cross couple the outputs, and perform the operation

$$\hat{b}_1 = U_1\hat{a}_1 + V_1\hat{a}_2^\dagger \tag{2.18}$$

$$\hat{b}_2 = U_2\hat{a}_2 + V_2\hat{a}_1^\dagger. \tag{2.19}$$

Again the operation must be unitary, which now requires that $|U_i|^2 - |V_i|^2 = 1$, and $U_1V_2 = U_2V_1$. We choose $U_1 = U_2 = U = \cosh s$ and $V_1 = V_2 = V = \sinh s$ to meet this requirement. Again s is real and positive, $s > 0$.

Phase insensitive amplifier; one coherent state input, one vacuum state input. Consider the case where the input on channel 1 is a coherent state $\langle\hat{a}_1\rangle = \alpha$, and the input on channel 2 is a vacuum state, $|\hat{a}_2\rangle = |0\rangle$. The output from the amplifier is given by

$$\left\langle\hat{b}_1\right\rangle = \alpha\cosh s \tag{2.20}$$

$$\left\langle\hat{b}_2\right\rangle = \alpha^*\sinh s, \tag{2.21}$$

and the intensities on the output are given by

$$\left|\left\langle\hat{b}_1\right\rangle\right|^2 = \alpha^2\cosh^2 s = G\alpha^2 \tag{2.22}$$

$$\left|\left\langle\hat{b}_2\right\rangle\right|^2 = \alpha^2\sinh^2 s = (G-1)\,\alpha^2, \tag{2.23}$$

where we have defined the gain, G, as a function of the squeezing parameter given by $G = \cosh^2 s$.

In this case the amplifier is phase insensitive, and the outputs have different intensities given by $i_- = \left|\left\langle \hat{b}_1 \right\rangle\right|^2 - \left|\left\langle \hat{b}_2 \right\rangle\right|^2 = \alpha^2$. This difference is due to seeding the process on only one input. In the limit of large gain, this difference becomes negligible compared to the overall intensity in each field.

The output fields here will also display intensity difference squeezing. In this case the total power in the output fields is given by $(2G-1)\alpha^2$, leading to a SN of $(2G-1)\mathcal{N}_\alpha$. The intensity difference i_- will be given by $\langle \Delta i_- \rangle = \mathcal{N}_\alpha$, where $\mathcal{N}_\alpha$ is the input SN. Thus the output signals will show an intensity difference squeezing given by

$$\begin{aligned} QNR &= \frac{\mathcal{N}_\alpha}{(2G-1)\mathcal{N}_\alpha} \\ &= \frac{1}{2G-1}. \end{aligned} \tag{2.24}$$

Phase sensitive amplifier; coherent state at both inputs. In the case where the same coherent state is applied to both input channels, $\langle \hat{a}_1 \rangle = \langle \hat{a}_2 \rangle = \alpha$, the output fields are also equal and are given by

$$\left\langle \hat{b}_1 \right\rangle = \left\langle \hat{b}_2 \right\rangle = \alpha \cosh s + \alpha^* \sinh s. \tag{2.25}$$

Both outputs now take the same form as in equation (2.10) and the phase-sensitive nature of the amplifier is regained [92].

TMSS generator; vacuum state at both inputs. When both input states to the amplifier are vacuum states, $|0\rangle$, once again we describe the system by the quadrature operators,

$$\hat{X}_{j,in} = \frac{\hat{a}_j^\dagger + \hat{a}_j}{2} \qquad \hat{Y}_{j,in} = \frac{i\left(\hat{a}_j^\dagger - \hat{a}_j\right)}{2} \tag{2.26}$$

$$\hat{X}_{j,out} = \frac{\hat{b}_j^\dagger + \hat{b}_j}{2} \qquad \hat{Y}_{j,out} = \frac{i\left(\hat{b}_j^\dagger - \hat{b}_j\right)}{2}, \tag{2.27}$$

where $j \in 1, 2$. Using the input/output relationship in equations (2.18) and (2.19), with $U_1 = U_1 = U$ and $V_1 = V_2 = V$, the relationship between $\hat{X}_{in}$ and $\hat{X}_{out}$ can be derived:

$$\hat{X}_{j,out} = \frac{U\left(\hat{a}_j^\dagger + \hat{a}_j\right) + V\left(\hat{a}_k + \hat{a}_k^\dagger\right)}{2}, \tag{2.28}$$

Similarly for the $\hat{Y}$,

$$\hat{Y}_{j,out} = \frac{iU\left(\hat{a}_j^\dagger - \hat{a}_j\right) - iV\left(\hat{a}_k^\dagger - \hat{a}_k\right)}{2}, \tag{2.29}$$

where $k \in 1, 2$, and $k \neq j$. Entanglement can be evidenced by correlations between these operators, or reduced noise on their combinations. The sum and difference of the output quadratures can be calculated as

$$\hat{X}_{-,out} = \hat{X}_{1,out} - \hat{X}_{2,out} = \frac{(U-V)\left(\hat{a}_1 - \hat{a}_2 + \hat{a}_1^\dagger - \hat{a}_2^\dagger\right)}{2} \tag{2.30}$$

$$\hat{Y}_{-,out} = \hat{Y}_{1,out} - \hat{Y}_{2,out} = \frac{i\,(U+V)\left(\hat{a}_1^\dagger - \hat{a}_2^\dagger - \hat{a}_1 + \hat{a}_2\right)}{2} \tag{2.31}$$

$$\hat{X}_{+,out} = \hat{X}_{1,out} + \hat{X}_{2,out} = \frac{(U+V)\left(\hat{a}_1 + \hat{a}_2 + \hat{a}_1^\dagger + \hat{a}_2^\dagger\right)}{2} \tag{2.32}$$

$$\hat{Y}_{+,out} = \hat{Y}_{1,out} + \hat{Y}_{2,out} = \frac{i\,(U-V)\left(\hat{a}_1 + \hat{a}_2 - \hat{a}_1^\dagger - \hat{a}_2^\dagger\right)}{2}. \tag{2.33}$$

The noise on these joint quadrature operators can then be calculated, following equation (2.4), as

$$\Delta\hat{X}_{-,out} = \frac{e^{-s}}{\sqrt{2}} \tag{2.34}$$

$$\Delta\hat{Y}_{-,out} = \frac{e^{s}}{\sqrt{2}} \tag{2.35}$$

$$\Delta\hat{X}_{+,out} = \frac{e^{s}}{\sqrt{2}} \tag{2.36}$$

$$\Delta\hat{Y}_{+,out} = \frac{e^{-s}}{\sqrt{2}}. \tag{2.37}$$

In order for the noise reductions apparent in $\hat{X}_{-,out}$ to occur, then, when $\hat{X}_1$ is higher than the mean value, $\hat{X}_2$ must be lower than the mean value. Similarly for the $\hat{Y}_{-,out}$ to show an increased noise, then, whilst $\hat{Y}_1$ is larger than average, then $\hat{Y}_2$ must also be larger than average. As such this output state is entangled [93]. In the case of the joint quadrature operators $\hat{Y}_\pm$ and $\hat{X}_\mp$ commute, and so can exhibit simultaneous QNR, whilst $\hat{Y}_\pm$ and $\hat{X}_\pm$ do not commute and so are constrained by the uncertainty principle [20].

2.5 Thin and thick gain media

A MSM squeezed field is defined as one where many different spatial regions of the field are independently squeezed. An infinitely thin gain medium will produce a MSM-squeezed field where any region, of the size of the wavelength, within the field would independently display squeezing.

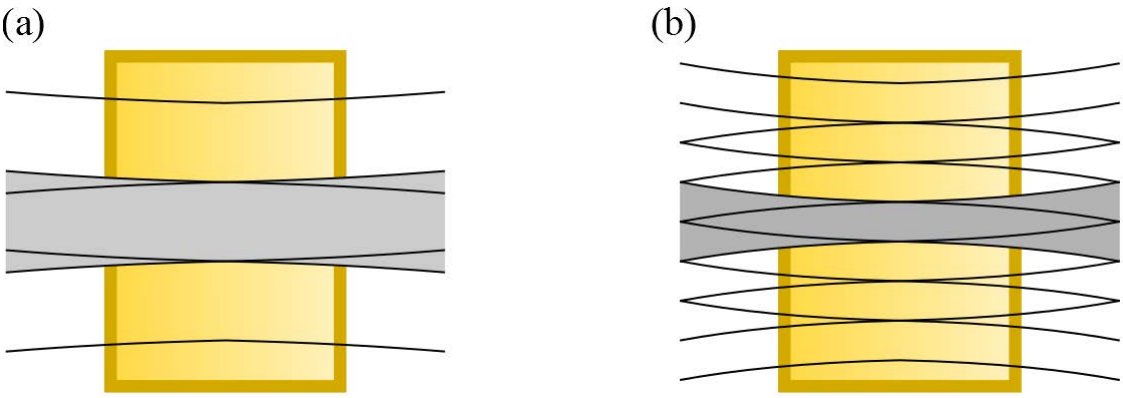

Figure 2.5: The evolution of adjacent Gaussian modes within the gain medium. The grey mode is shaded for clarity, showing the overlap with adjacent modes. (a) An example when the mode waist is larger than l_{coh}. Here the modes only slightly overlap at the end of the gain medium. The modes are not coupled by the medium, and localised squeezing can be measured on these modes. (b) An example when the mode waist is smaller than l_{coh}. Here the waist is small enough that the modes will expand such that they are significantly cross-coupled by the gain medium, and no squeezing is present in the mode. In this case the mode waist is by definition l_{coh}.

Experimentally no amplifier can truly be thought of as a thin medium. Instead the amplifier must have some defined length. Any Gaussian mode will expand as it travels through a thick gain medium. This expansion means that adjacent modes will have some overlap at either end of the medium (figure 2.5(a)). These modes then become coupled by the medium. The smaller the waist size of a Gaussian mode, the quicker it will expand. Thus there exists a smallest mode size where independent local squeezing can be observed, called the coherence length l_{coh}.

The coherence area is defined as the mode size where there is no longer any measurable squeezing [94]. An estimate of the coherence area can be calculated by considering the packing of Gaussian modes within the gain medium. The coherence length is the size of a mode waist where the width expands to be a factor of $\sqrt{2}$ larger at each end of the cell, compared to its waist, in the centre of the gain medium. Modes of this size can be cross-coupled by the gain medium (figure 2.5(b)), and, as such, these modes cannot support squeezing. This expansion is exactly that which occurs over the Rayleigh distance, given by $Z_r = \pi\omega^2(0)/\lambda$, where $\omega(0)$ is the waist size of the Gaussian mode [95]. Thus, the coherence length, l_{coh}, is the waist size of a Gaussian mode with a Rayleigh distance equal to the length of the gain medium, l_g. This limit has also been described theoretically by Lopez et al. [96] using mode decomposition and an interaction kernel, resulting in the same coherence length of

$$l_{coh} = \sqrt{\frac{\lambda l_g}{\pi n_s}}, \tag{2.38}$$

where λ is the wavelength of the light, l_g is the length of the gain region, and n_s is the index of refraction

of the medium. The coherence length accurately derived by Lopez et al. is exactly that estimated using the expansion of Gaussian modes.

The ratio of the coherence area to a given pump size can be used to calculate a theoretical maximum number of independent modes for which squeezing could be observed:

$$\begin{aligned} \text{number of modes} &= \frac{\omega_p^2}{l_{coh}^2} \\ &= \frac{\omega_p^2 \pi n_s}{\lambda l_g}, \end{aligned} \tag{2.39}$$

where ω_p is the pump waist size. This theoretical limit can only be reached if the whole of the emission spectrum of the gain medium is collected.

The number of modes produced can be further restricted. In continuous variable PDC systems a cavity is required to increase the gain of the system, such that strong quadrature squeezing can be produced. In general these cavities operate on only one transverse spatial mode. As such, only a single spatial mode of quadrature squeezed light can be generated. There have been some experiments where this limit has been increased up to three spatial modes, by the use of confocal cavities [75, 78, 79, 97].

To achieve a large number of spatial modes the system must be operated in free space with only a single pass gain. This configuration requires a much larger single pass gain to generate strong quadrature squeezing. The gain in a 4WM process in hot atomic vapours can reach this level. Previously Corzo et al. have measured multi-mode squeezing on an estimated 12 symmetric modes using hot rubidium vapour as the gain medium [84]. We have also generated and characterised a highly multimode squeezed vacuum field, containing 75 modes [86], which will be discussed later in this thesis.

2.6 The relationship between entanglement and squeezing

Entanglement and squeezing are intrinsically linked, as can be seen from the similarities between equations (2.16)-(2.17) and (2.34)-(2.37). In fact the processes of generating entanglement and squeezing are entirely equivalent. Two fields are said to be entangled when correlations exist within the joint quadratures such that one has reduced fluctuations at the expense of the other eg. $\hat{X}_- < 1/2$ and $\hat{Y}_- > 1/2$. In a squeezed field these correlations exist within a single propagation mode. As such, the entanglement and squeezing can be said to be identical, with only a change of mode definition. As an extension of this, propagation, causing a change of mode, can be used to transform a squeezed state into an entangled state. In this section, I will

first describe the necessary mode transformation between entanglement and squeezing theoretically. I will then introduce the beam splitter and its quantum mechanical operation, and show that this operation will transform between SMSS and TMSS. I will also show how propagation can perform the same transformation. I will explain how they are related to the experimental generation of squeezed light as undertaken in this thesis.

2.6.1 Mode transformation

Consider the process of a two mode amplifier as used for generating entanglement, and described in equations (2.18) and(2.19). If we apply the mode transformations

$$\hat{a_+}' = \frac{1}{\sqrt{2}}\left(\hat{a}_1 + \hat{a}_2\right) \qquad \hat{a_-}' = \frac{1}{\sqrt{2}}\left(\hat{a}_1 - \hat{a}_2\right) \tag{2.40}$$

$$\hat{b_+}' = \frac{1}{\sqrt{2}}\left(\hat{b}_1 + \hat{b}_2\right) \qquad \hat{b_-}' = \frac{1}{\sqrt{2}}\left(\hat{b}_1 - \hat{b}_2\right), \tag{2.41}$$

the system, described by equations (2.18) and (2.19), can be described by

$$\hat{b_+}' = U\hat{a_+}' + V\hat{a_+}'^{\dagger} \qquad \hat{b_-}' = U\hat{a_-}' - V\hat{a_-}'^{\dagger}, \tag{2.42}$$

where the mode associated with $\hat{b_+}'$ takes exactly the form resulting from the single mode amplifier, which generates squeezing as described in equation (2.7). The mode associated with $\hat{b_-}'$ also takes the same form, but where the sign of the squeezing parameter is switched, $s \to -s$. This mode transformation highlights the equivalence between squeezed states and entangled states. For this reason, an entangled state is often referred to as a two mode squeezed state (TMSS).

In experimental quantum optics it is natural to define a set of modes by the position and/or direction of propagation of a state. This leads to an experimental distinction between a TMSS and a single mode squeezed state (SMSS). Fortunately there are some experimental techniques which allow the conversion between a TMSS and a SMSS. In this section I will describe the use of beam splitters and propagation to achieve this conversion.

2.6.2 beam splitters

When placed in a single field, a beam splitter transmits some light, and reflects the rest. Consider a beam splitter, such as that shown in figure 2.6, with transmittance t and reflectance r. Classically (figure 2.6(a))

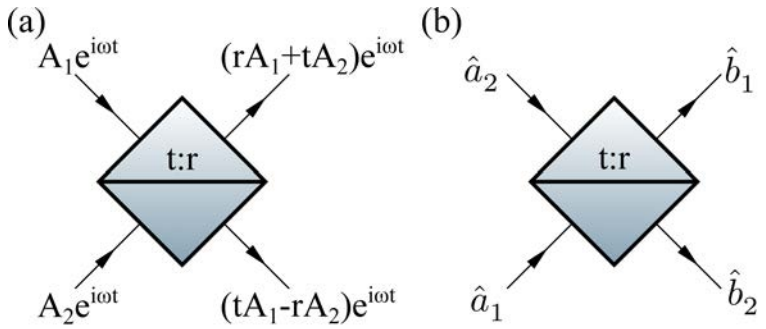

Figure 2.6: A beam splitter, with transmission t and reflectivity r. (a) shows the classical case where each input light field is split into two outputs. (b) shows the quantum mechanical case with input annihilation operators $\hat{a}_1$ and $\hat{a_2}$, and output operators $\hat{b}_1$ and $\hat{b}_2$. The operator transformations are given in equations (2.43) and (2.44).

each incident field is split according to the transmittance and reflectance. Quantum mechanically (figure 2.6(a)) incident field operators $\hat{a}_1$ and $\hat{a}_2$, transform into the output fields operators $\hat{b}_1$ and $\hat{b}_2$ according to the reversible transformations

$$\hat{b}_1 \leftrightarrow t\hat{a}_1 + r\hat{a}_2 \tag{2.43}$$

$$\hat{b}_2 \leftrightarrow t\hat{a}_2 - r\hat{a}_1. \tag{2.44}$$

Conservation of energy at the beam splitter requires that $t^2+r^2 = 1$. When two fields are interfered, normally a 50:50 beam splitter is used, where $t = r = 1/\sqrt{2}$.

It is also instructive to consider the quadrature operators. These are defined on the input and output as

$$\hat{X}_{j,in} = \frac{\hat{a}_j^\dagger + \hat{a}_j}{2} \qquad \hat{Y}_{j,in} = \frac{i\left(\hat{a}_j^\dagger - \hat{a}_j\right)}{2} \tag{2.45}$$

$$\hat{X}_{j,out} = \frac{\hat{b}_j^\dagger + \hat{b}_j}{2} \qquad \hat{Y}_{j,out} = \frac{i\left(\hat{b}_j^\dagger - \hat{b}_j\right)}{2} \tag{2.46}$$

where $j \in 1, 2$. Using these definitions, and the operator transformations given in equations (2.43) and (2.44), and taking t and r to be real, we can determine that

$$\hat{X}_{1,out} = t\hat{X}_{1,in} + r\hat{X}_{2,in} \qquad \hat{Y}_{1,out} = t\hat{Y}_{1,in} + r\hat{Y}_{2,in} \tag{2.47}$$

$$\hat{X}_{2,out} = t\hat{X}_{1,in} - r\hat{X}_{2,in} \qquad \hat{Y}_{2,out} = t\hat{Y}_{1,in} - r\hat{Y}_{2,in}, \tag{2.48}$$

The mode transformations that allow the TMSS amplifier (section 2.4) to be treated as a SMSS amplifier

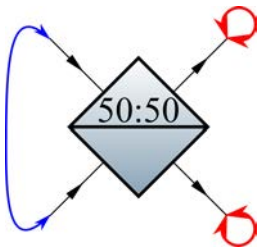

Figure 2.7: A beam splitter, with an TMSS on the inputs produces a pair of individually SMSS on the outputs. The blue double arrow on the input symbolises the entanglement between the two modes that make up the TMSS on the input, and the red double arrows on the output symbolise the two independent squeezed states. This convention is retained throughout this thesis.

(section 2.3) can be exactly reproduced by a 50:50 beam splitter where the input/output mode relationship (equations (2.43) and (2.44)) becomes

$$\hat{b}_1 \leftrightarrow \frac{1}{\sqrt{2}}\left(\hat{a}_1 + \hat{a}_2\right) \tag{2.49}$$

$$\hat{b}_2 \leftrightarrow \frac{1}{\sqrt{2}}\left(\hat{a}_2 - \hat{a}_1\right). \tag{2.50}$$

These transformations implicitly assume that input modes, with associated operators $\hat{a}_1$ and $\hat{a}_2$, are perfectly overlapped. As such, in experimental optics a great deal of care needs to be taken to ensure that any modes are perfectly overlapped on any beam splitters.

In this configuration the beam splitter defines precisely the mode transformation needed to convert between a TMSS and two SMSSs undertaken in equations (2.41) and (2.40). Consider the case where one half of a TMSS is on each input of a 50:50 beam splitter (figure 2.7). The variances of the quadratures on the output fields of the beam splitter can be derived

$$\Delta\hat{X}_{1,out} = \frac{1}{\sqrt{2}}\Delta\left(\hat{X}_{1,in} + \hat{X}_{2,in}\right) = \frac{e^s}{2} \tag{2.51}$$

$$\Delta\hat{Y}_{1,out} = \frac{1}{\sqrt{2}}\Delta\left(\hat{Y}_{1,in} + \hat{Y}_{2,in}\right) = \frac{e^{-s}}{2} \tag{2.52}$$

$$\Delta\hat{X}_{2,out} = \frac{1}{\sqrt{2}}\Delta\left(\hat{X}_{1,in} - \hat{X}_{2,in}\right) = \frac{e^{-s}}{2} \tag{2.53}$$

$$\Delta\hat{Y}_{2,out} = \frac{1}{\sqrt{2}}\Delta\left(\hat{Y}_{1,in} - \hat{Y}_{2,in}\right) = \frac{e^s}{2}. \tag{2.54}$$

Thus each of the two outputs from the beam splitter will show reduced noise on one quadrature and increased noise on the other. Thus, here, the incident entanglement is converted into squeezing. As with all beam splitter processes this is entirely reversible, and a beam splitter can also be used to convert squeezed light

into entangled light.

These derivations are assuming a SSM system, where the two modes of the TMSS perfectly overlapped on the beam splitter. In an experiment such precise alignment is difficult to achieve. Any deviation from the perfect alignment will mean a lower level of QNR in the output squeezed state.

2.6.3 Propagation

In sections 2.3 and 2.4 I described the operation of an amplifier on a given mode structure before and after the gain medium. In these examples the mode structure is taken immediately after the gain medium, without any propagation considered. In order to use the squeezed state outputs from these gain media for any practical use the states must be allowed to propagate in space. In particular, if the squeezed state is to be used for quantum imaging, the state must propagate in space and be brought onto the object being imaged. As such it is very important to consider how these states change when propagating in free space. Under this free space propagation the momentum of the SMSS, produced from an amplifier as discussed in section 2.4, is converted into position. Thus the propagation performs a unitary mode transformation, converting the SMSS in the near field into a TMSS in the far field. In this section I investigate this free space propagation of such a squeezed state.

Consider an amplifier that generates a single mode squeezed state, $\hat{b}'_+$, in the near field. This state can be treated as that generated by the two-mode amplifier as described in equations (2.18) and (2.19), where in the near field, modes $\hat{b}_1$ and $\hat{b}_2$ are perfectly overlapped. As the field propagates to the far field its near-field operators, $\hat{b}_1(x)$ and $\hat{b}_2(x)$, where x defines the near-field position, transform according to the Fourier transforms,

$$\hat{b}_1(q) = \mathcal{F}\left[\hat{b}_1(x)\right] \tag{2.55}$$

$$\hat{b}_2(q) = \mathcal{F}\left[\hat{b}_2(x)\right] \tag{2.56}$$

$$\hat{b}_1^\dagger(q) = \mathcal{F}\left[\hat{b}_1^\dagger(-x)\right] \tag{2.57}$$

$$\hat{b}_2^\dagger(q) = \mathcal{F}\left[\hat{b}_2^\dagger(-x)\right], \tag{2.58}$$

where $\hat{b}_i(q)$ and $\hat{b}_i^\dagger(q)$ are the corresponding far-field operators. q is the Fourier conjugate variable of x, and

describes the position in the far-field. From this we can calculate the quadrature operators in the far field,

$$\hat{X}_j(q) = \frac{\hat{b}_j^\dagger(q) + \hat{b}_j(q)}{2} \tag{2.59}$$

$$= \frac{1}{2}\mathcal{F}\left[\hat{b}_j^\dagger(-x) + \hat{b}_j(x)\right] \tag{2.60}$$

$$\hat{Y}_j(q) = \frac{i\left(\hat{b}_j^\dagger(q) - \hat{b}_j(q)\right)}{2} \tag{2.61}$$

$$= \frac{i}{2}\mathcal{F}\left[\hat{b}_j^\dagger(-x) - \hat{b}_j(x)\right]. \tag{2.62}$$

Note that these far-field quadrature operators are not the simple Fourier transforms of the near-field quadrature operators. This difference between the propagation of the field operators and the quadrature operators gives rise to an interesting property. Consider the far-field joint quadrature operators between symmetric modes located at q and $-q$. These can be derived in terms of the near-field operators as

$$\begin{aligned}\hat{X}_-(q) &= \hat{X}_1(q) - \hat{X}_2(-q) \\ &= \frac{1}{2}\mathcal{F}\left[\hat{b}_1^\dagger(-x) + \hat{b}_1(x) - \hat{b}_2^\dagger(-x) - \hat{b}_2(x)\right] \\ &= \frac{1}{2}\mathcal{F}\left[\hat{X}_-(x) + \hat{X}_-(-x)\right] \end{aligned} \tag{2.63}$$

$$\begin{aligned}\hat{Y}_-(q) &= \hat{Y}_1(q) - \hat{Y}_2(-q) \\ &= \frac{i}{2}\mathcal{F}\left[\hat{b}_1^\dagger(-x) - \hat{b}_1(x) - \hat{b}_2^\dagger(-x) + \hat{b}_2(x)\right] \\ &= \frac{i}{2}\mathcal{F}\left[\hat{Y}_-(x) + \hat{Y}_-(-x)\right] \end{aligned} \tag{2.64}$$

$$\begin{aligned}\hat{X}_+(q) &= \hat{X}_1(q) + \hat{X}_2(-q) \\ &= \frac{1}{2}\mathcal{F}\left[\hat{b}_1^\dagger(-x) + \hat{b}_1(x) + \hat{b}_2^\dagger(-x) + \hat{b}_2(x)\right] \\ &= \frac{1}{2}\mathcal{F}\left[\hat{X}_+(x) + \hat{X}_+(-x)\right] \end{aligned} \tag{2.65}$$

$$\begin{aligned}\hat{Y}_+(q) &= \hat{Y}_1(q) + \hat{Y}_2(-q) \\ &= \frac{i}{2}\mathcal{F}\left[\hat{b}_1^\dagger(-x) - \hat{b}_1(x) + \hat{b}_2^\dagger(-x) - \hat{b}_2(x)\right] \\ &= \frac{i}{2}\mathcal{F}\left[\hat{Y}_+(x) + \hat{Y}_+(-x)\right]. \end{aligned} \tag{2.66}$$

Each of these symmetric mode joint quadrature operators are formed from the Fourier transform of a superposition of two near-field quadrature operators. In each case both near-field quadratures have the same reduced or increased quantum noise. This leads to each far-field joint quadrature being similarly squeezed

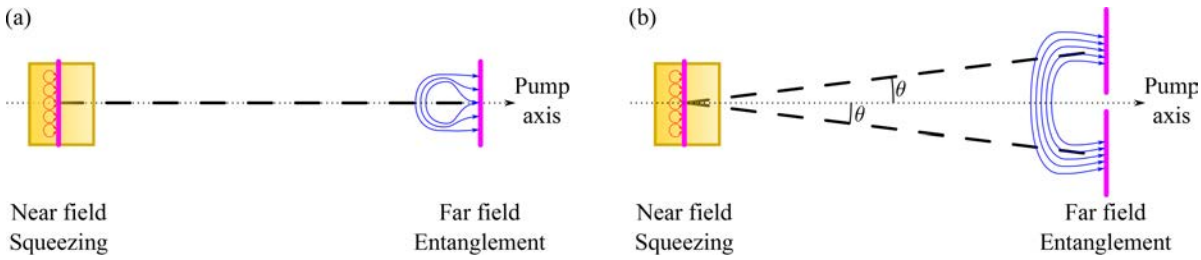

Figure 2.8: A gain system creating squeezing in the near field, as correlations between two modes, depicted by red loops. (a) Shows the transformation into squeezing on symmetric modes where the modes propagate along the same direction. (b) Shows the transformation to entanglement in the far field, where the two modes propagate at a small angle $\pm\theta$ to the pump axis. In both cases the state is a SMSS in the near field and a TMSS in the far field.

or anti-squeezed. Thus it can be seen that, with propagation, the field changes from being a SMSS into a TMSS, exhibiting correlations symmetrically about the central propagation axis.

When the twin entangled modes are rigorously co-propagating, the two modes of the TMSS, formed in the far field, fully overlap each other (figure 2.8(a)). As with all squeezed states, reductions in quantum noise fluctuations can only be measured within a given mode structure. In this case the squeezing can be measured in radially symmetric modes about the pump axis. A similar system has been previously investigated by Corzo et al. [84], who measured squeezing on up to 12 symmetric modes.

In some situations the gain medium can impose a phase matching condition, which requires that the two near-field modes $\hat{b}_1$ and $\hat{b}_2$ propagate along slightly different directions separated by a small angle 2θ (figure 2.8(b)). Again the SMSS, that is present in the near field, transforms into a TMSS in the far field. However, in this case, the two modes of the TMSS are spatially separated. Theoretically, these regions from an annulus around the pump axis. Experimentally, due to the horizontal overlap process, the regions are restricted to two areas located on the horizontal axis, shown in green in figure 2.9. These two distinct far-field gain regions are referred to as the restricted gain regions (RGRs) [86].

In both the case where the RGRs propagate with a small angle, and where the RGRs are rigorously co-propagating, the propagation transforms the SMSS in the near field to a TMSS in the far field.

2.6.4 Returning to squeezed light after propagation

The beam splitter transformations are entirely reversible, and as such it is relatively trivial to convert from a SMSS to a TMSS and back. In principal propagation is entirely reversible, and indeed an imaging system can be used to image the near field, and regain the SMSS in the image plane.

The far-field gain spectrum also imposes limits on which spatial frequencies might be squeezed. In the case

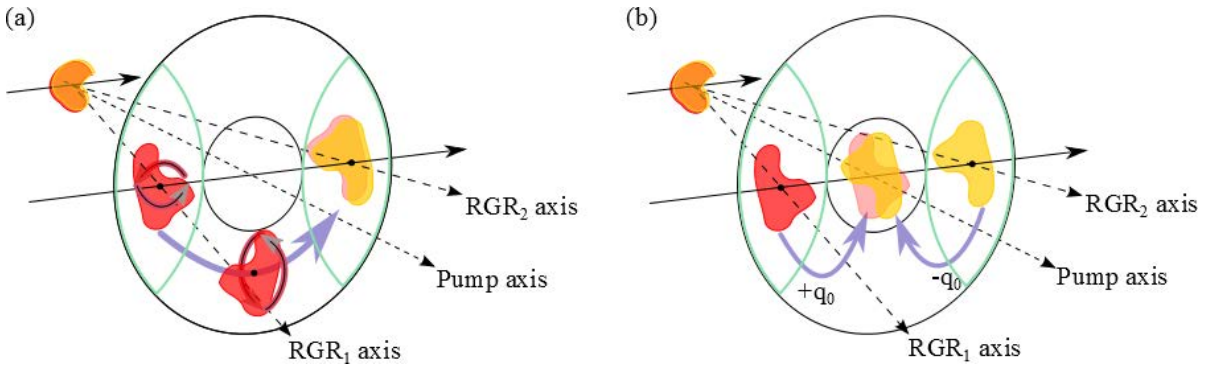

Figure 2.9: The gain of the system, with modes shown in the near field, and far field. (a) shows the translation and flipping required to investigate the squeezing in the far field. (b) shows the translation used for investigating the near-field squeezing properties. The black circles represent the conical emission of the amplifier. The green regions represent restricted gain regions (RGRs) that are overlapped in the experiment.

of overlapped co-propagating RGRs (figure 2.8(a)), this limit is in the form of a maximum spatial frequency that can be squeezed, corresponding to the near-field coherence length. Thus such an imaging system can be used to convert back to a squeezed state, with only a limit on the maximum spatial frequency that can be squeezed. However, in the case of the RGRs propagating at a small angle (figure 2.8(b)), the far field gain spectrum has a region at low spatial frequencies with low gain. This area cannot be used for squeezed light, both due to low gain and to the strong pump causing contamination on this axis. In a three dimensional picture, this results in a gain annulus as shown in figure 2.9. This imposes both a lower and upper limit to the spatial frequencies that can be squeezed. In the near field, this corresponds to both a lower and upper limit on the size of the features a mode can have, if it is to be squeezed. This results in any mode containing large bright regions not being squeezed. As such, the SMSS will have a complicated mode structure.

To avoid using this strange mode structure, we can use the knowledge that entangled states can be transformed into squeezed states using a beam splitter (section 2.6). As such, it is possible to convert between TMSS and SMSS in the far field.

The pairs of correlated modes must be perfectly overlapped on the beam splitter for a successful conversion without a loss of squeezing. This must be achieved for all spatial modes present in the field. In the context of figure 2.8(b) this corresponds to overlapping the two ends of each blue arrow. Geometrically, in a three-dimensional system, this involves one of the RGRs being flipped both horizontally and vertically with respect to the other, as shown in figure 2.9(a). In practice, even with this manipulation, the two modes of the TMSS are likely to have expanded slightly differently, due to differing Kerr lensing affects in the gain medium, or slight differences in propagation path. Consequently, precise control of the mode shape would be very

difficult in such an experiment. Nonetheless, previously our group has measured some squeezing using this method [98].

Instead it is possible to combine the two methods, and investigate the squeezing in the near field. The RGRs can be overlapped in the far field, removing the hole in the spatial frequency spectrum. The combined field will then form a rigorously co-propagating TMSS, exactly as that of the TMSS in figure2.8(a). It can then be imaged as a SMSS in the near field. In this experiment, the overlap process is equivalent to a translation in the Fourier plane, and is shown in figure 2.9(b).

To verify that the squeezing is retained when overlapping in the far field and measuring in the near field the translation, by $\pm q_0$, must be added to the far-field operators. They become

$$\hat{b}_1'(q) = \hat{b}_1(q + q_0) \tag{2.67}$$

$$\hat{b}_2'(q) = \hat{b}_2(q - q_0). \tag{2.68}$$

When these operators are transformed back into the near field, using the reverse of the transformations in equations (2.55)-(2.58), the translation becomes equivalent to an additional phase in the near field as described by

$$\hat{b}_1'(x) = \hat{b}_1(x) e^{-i\theta} \tag{2.69}$$

$$\hat{b}_2'(x) = \hat{b}_2(x) e^{+i\theta}, \tag{2.70}$$

where $\theta = \mathbf{q_0}.\mathbf{x}$. Similarly the transformation of the creation operators can be calculated as

$$\hat{b}_1^{\dagger\prime}(x) = \hat{b}_1^{\dagger}(x) e^{i\theta} \tag{2.71}$$

$$\hat{b}_2^{\dagger\prime}(x) = \hat{b}_2^{\dagger}(x) e^{-i\theta}. \tag{2.72}$$

Using these transformations and retaining the TMSS description, even after overlapping the correlated fields,

we can calculate the new quadrature operators as,

$$\hat{X}_1'(x) = \hat{X}_1(x)\cos\theta + \hat{Y}_1(x)\sin\theta \tag{2.73}$$

$$\hat{Y}_1'(x) = \hat{Y}_1(x)\cos\theta - \hat{X}_1(x)\sin\theta \tag{2.74}$$

$$\hat{X}_2'(x) = \hat{X}_2(x)\cos\theta - \hat{Y}_2(x)\sin\theta \tag{2.75}$$

$$\hat{Y}_2'(x) = \hat{Y}_2(x)\cos\theta + \hat{X}_2(x)\sin\theta. \tag{2.76}$$

The modified joint quadrature operators can be calculated in terms of the original joint quadrature operators,

$$\hat{X}_-'(x) = \hat{X}_-(x)\cos\theta + \hat{Y}_+(x)\sin\theta \tag{2.77}$$

$$\hat{Y}_-'(x) = \hat{Y}_-(x)\cos\theta - \hat{X}_+(x)\sin\theta \tag{2.78}$$

$$\hat{X}_+'(x) = \hat{X}_+(x)\sin\theta + \hat{Y}_-(x)\cos\theta \tag{2.79}$$

$$\hat{Y}_+'(x) = \hat{Y}_+(x)\cos\theta - \hat{X}_-(x)\sin\theta. \tag{2.80}$$

Since the linear superposition of two squeezed quantities is also a squeezed quantity we can confirm that the squeezing in $\hat{X}_-$ and $\hat{Y}_+$ is retained through the translation process. Similarly the anti-squeezing, in $\hat{X}_+$ and $\hat{Y}_-$, is retained. As such, overlapping in the far field, and detecting in the near field will accurately investigate the nature of the squeezed light. This method has the advantage of being able to control accurately, and to image, the mode shape of the squeezed field being measured.

2.7 Applications of squeezed light

Squeezed light is fundamentally a reduction of the quantum noise of either phase or amplitude (or any quadrature in between), at the expense of excess noise on the other. In many experiments where light is used as a measurement tool, the accuracy of the measurement is limited by the SN on either the amplitude or the phase of the light. The signal-to-noise ratio in such systems can be improved by using more powerful light. However, the intensity required to achieve sufficiently accurate measurements may damage the systems being measured. It is here that squeezed light can help. The reduced level of the quantum noise improves the signal-to-noise ratio of measurement without changing the overall light power. Thus, the measurement accuracy is improved without risking any damage to the sample.

TMSS, or entangled states, can be used for secure communication in quantum key distribution schemes [99,

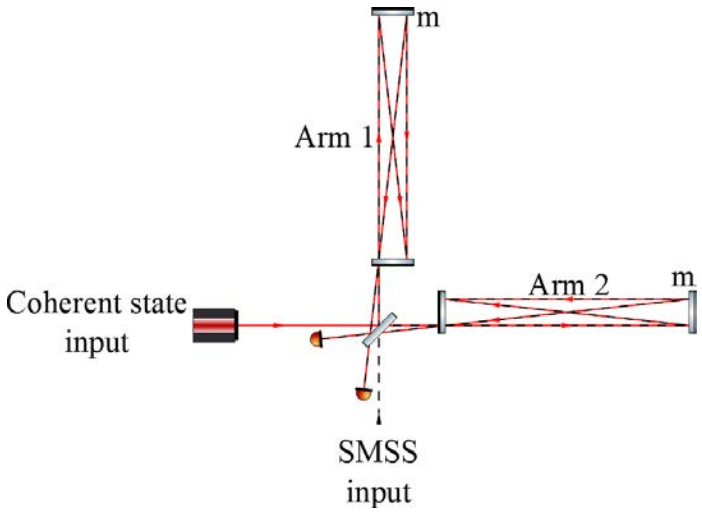

Figure 2.10: An interferometer as might be used for detection of gravitation waves. This interferometer has two bounces at each end mirror, this is parametrised in $b = 2$. The two arms (1,2) have optical path length z_1 and z_2 with an optical path length difference $z = z_1 - z_2$.

100], and state teleportation [101]. SMSS, or quadrature squeezed states, squeezed on a single spatial mode, can be used to increase the information capacity in communication schemes [102–104], improve accuracy in measuring absorption, scattering and modulated signals [105–108], and improve interferometric accuracy [33], including in gravitational wave detection [8, 34]. MSM-squeezed states can enhance many imaging systems [62, 65, 66, 69–71, 87]. This can be done in the photon counting regime or in bright field quantum imaging.

The results of this thesis are of particular interest in the fields of interferometric measurements and bright field quantum imaging. In the next sections, I will expand further on the quantum noise limit (QNL) of these systems, and how squeezed light can improve the limit. I will highlight some interesting requirements on the squeezed light, in order for the optimum improvement of these measurements to be achieved.

2.7.1 Interferometry

Interferometry is used in many different fields from the detection of gravitational waves [109] to precision metrology measurements [110]. In each case the interferometer measures an optical path length difference between the two arms, $z = z_1 - z_2$ (figure 2.10). This can arise either out of a physical difference in the length of the arms, or some phase retarding medium placed in one of the arms. As with all systems an interferometry detection scheme has some minimum quantum noise. This standard quantum limit (SQL)

results in an error on z of

$$(\Delta z)_{SQL} = \sqrt{\frac{2\hbar\tau}{m}}, \tag{2.81}$$

where m is the mass of each end mirror, and τ is the duration of the measurement [33].

The overall noise has two major contributions; photon counting noise $(\Delta z)_{pc}$ and radiation pressure noise $(\Delta z)_{rp}$. The photon counting noise arises from the fluctuating number of photons. The radiation noise arises from the fluctuating radiation pressure of the photons pushing on the end mirrors. Caves derived the noise contributions from these two sources in the case of a coherent state input on port 1 of amplitude β, and a squeezed light input on port 2 of squeezing parameter s [36]. These contributions take the form

$$(\Delta z)_{pc} = \frac{c}{2b\omega\,|\beta|} e^{-s} \tag{2.82}$$

$$(\Delta z)_{rp} = \frac{b\hbar\omega\tau\,|\beta|}{mc} e^{s}, \tag{2.83}$$

where ω is the frequency of the light, b is the number of reflections on each end mirror, τ is the measurement time, m is the mass of each of the end mirrors, and c is the speed of light. In these equations the sign of s describes which quadrature is squeezed. When no squeezing is present the squeezing parameter becomes zero, $s = 0$. The total noise on the output signal is given by a sum of these two contributions as

$$\Delta z = \left((\Delta z)_{pc}^2 + (\Delta z)_{rp}^2 \right). \tag{2.84}$$

It is important to note that these noise contributions have very different dependencies on frequency. $(\Delta z)_{pc}$ decreases with increased signal frequency, whilst $(\Delta z)_{rp}$ noise increases with increased signal frequency. The minimum noise of $(\Delta z)_{SQL}$ is given when these two contributions are balanced. The noise at a frequency just below this point is dominated by $(\Delta z)_{pc}$, and can be reduced with amplitude squeezing ($s < 0$). The noise at a frequency just above this point is dominated by $(\Delta z)_{rp}$, and can be reduced with phase squeezing ($s > 0$). This means that, for squeezed light to introduce the best improvement in the interferometric noise over a wide frequency range, the vacuum's squeezed quadrature, or NEP, must rotate by 90 degrees around 50 Hz [111].

It is this effect that Unruh noticed in 1983 when he proposed that the quantum noise in an interferometer could be reduced on many frequencies if a source of squeezed light could be found that produces amplitude squeezed light at low frequencies and phase at high frequencies [9, 112].

Since then there have been proposals made by various groups based around the use of pre-filtering cavities

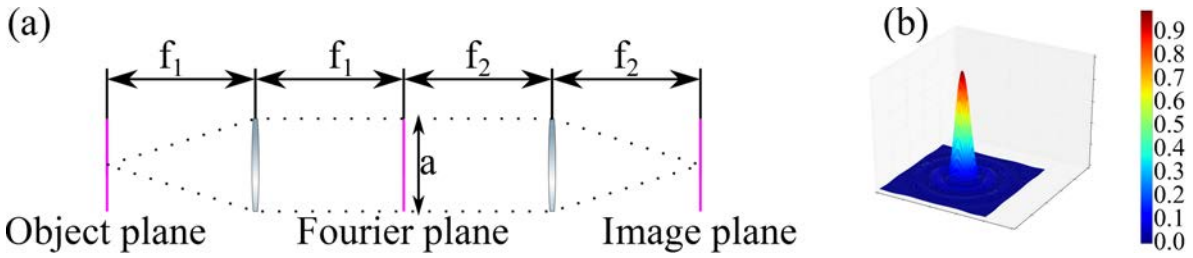

Figure 2.11: (a) a 4f imaging system, with magnification f_2/f_1. (b) The intensity profile of the image of a point source given the finite size of the lenses.

as first proposed by Kimble [39–42]. In 2013 Horrom demonstrated an example of frequency dependent phase rotation using EIT [43]. In 2013 Corzo et al. directly investigated a 4WM system, inferred the noise ellipse phase (NEP) of the squeezed light generated [44], and showed a frequency dependent rotation of the NEP. Such a squeezed state of light should allow an interferometer to make measurements below the SQL for a wide range of frequencies.

In the experimental section (section 4.4) of this thesis, I produce a quadrature squeezed state and directly measure the phase rotation of the frequency components caused by the gain medium. In this way, I evidence the ability to concurrently measure QNR on the phase quadrature at one frequency, whilst measuring QNR on the amplitude quadrature at a different frequency.

2.7.2 Imaging and super-resolution

There are many types of optical imaging systems from microscopes, for looking at very small objects up close, to telescopes, used for looking at very large objects far away. Fundamentally all imaging systems are very similar, comprising of a series of lenses of a given transverse size and focal length. If all lenses are considered to be perfect thin lenses, with no aberrations, then the resolution of any system will be limited by the finite size of the apertures that the light travels through. This is called the diffraction limit.

Consider a two lens imaging system, where the lenses are separated by the sum of their focal lengths, $f_1 + f_2$. The source of light is placed one focal length, f_1, before the first lens and the image forms one focal length, f_2, after the second lens. Any amplification is given by the ratio between the focal lengths of the lenses $M = f_2/f_1$. Such an imaging system is shown for a point source in figure 2.11(a). A finite size lens can be treated as an infinite lens with a slit placed behind it. As such the effect of the lens' finite size acts in a similar way to a single slit often described in the literature [113]. The result of the diffraction is that the spot size of the image is broadened, as shown in figure 2.11(b). For a point source, the intensity profile

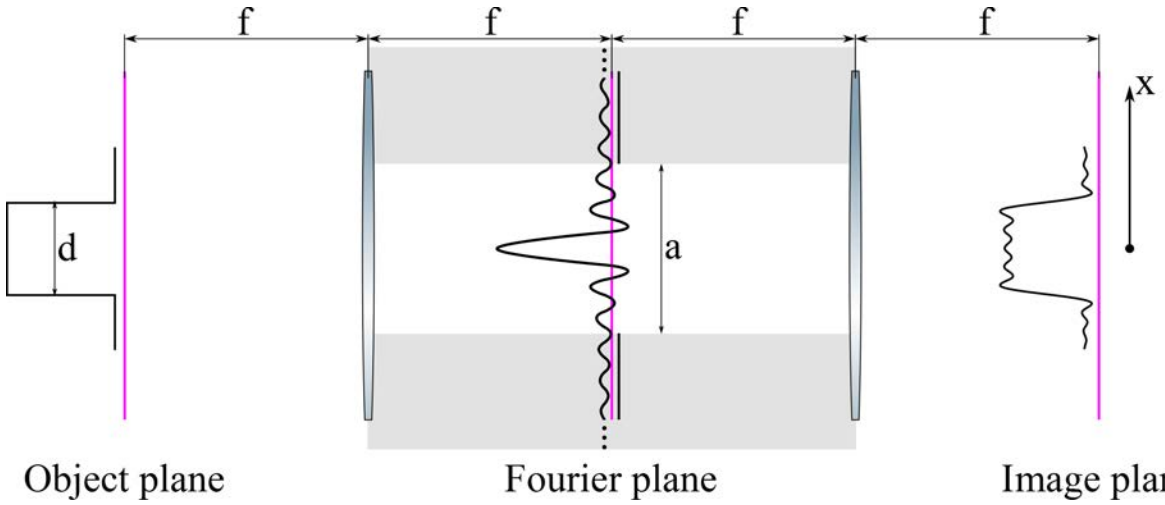

Figure 2.12: A simple 4f imaging system, with object, Fourier, and image planes. There is a central aperture that restricts the transmitted spatial frequencies, leading to a distorted image. Super-resolution analytically extends the Fourier spectrum of the image with the aim of improving the representation of the object. Here the lenses are treated as infinite, with their size restrictions being replaced with an aperture in the centre. The grey regions are the regions discarded by this aperture.

in the image plane is described by

$$I(x) = I_0 \left(\frac{\sin \beta}{\beta} \right)^2, \tag{2.85}$$

where $\beta = kax/f_2$, $k = \frac{2\pi}{\lambda}$ is the wavevector of the light, a is the smallest transverse diameter in the system, and x is the transverse co-ordinate in the image plane. I_0 is the fraction of light that makes passes through the imaging system, defined by the solid angle subtended by the slit at the point source.

The diffraction broadening of the point source object leads to a minimum separation where two point objects would be resolvable. There are a number of different exact definitions of when two objects are resolvable. Perhaps the most famous is the Rayleigh criterion [114], which takes two objects to be just resolvable where one image peak lies exactly at the first minimum of the next, and, for a circular aperture, is given by

$$R = 1.22 \frac{f\lambda}{a}, \tag{2.86}$$

where R is the minimum resolvable separation, f is the focal length of the lens, λ is the wavelength of the light, and a is the smallest transverse diameter in the optical system. This can be provided by either the size of a finite lens or an aperture. Under this criterion the exact location of a point source is only known to this accuracy.

The finite size of these lenses can be thought of as an aperture in the Fourier plane in the middle of the

imaging system, which removes the high-order spatial modes of the system. This is easily demonstrated by considering a single sharp sided object, of diameter d, imaged through the system (figure 2.12). Restricting the discussion to only 1 dimension such a slit can be described by

$$A(x) = \begin{cases} 1 & \text{where } -\frac{d}{2} < x < \frac{d}{2} \\ 0 & \text{otherwise} \end{cases} . \tag{2.87}$$

In this case the full Fourier spectrum is given by $A(q) = \mathcal{F}(A(x)) = A_0\left(\frac{\sin kdq}{kdq}\right)$, where A_0 is the peak amplitude. This is restricted, in the far field, by the aperture, representing the size of the lens, and so the function becomes

$$A(q) = \begin{cases} A_0\left(\frac{\sin kdq}{kdq}\right) & \text{where } -\frac{a}{2} < x < \frac{a}{2} \\ 0 & \text{otherwise} \end{cases} , \tag{2.88}$$

where a is the size of the aperture. The final image is then given by the Fourier transform of this function $A'(x) = \mathcal{F}^{-1}(A(q))$. In this example the loss of high order spatial frequencies can be seen in the image plane as the sharp edges to the slit are poorly represented (figure 2.12).

The resolution of such optical system can be improved by some post-processing techniques. Images are said to be super-resolved if features smaller than the resolution limit can be measured. A simplified post-processing super-resolution technique is to extend the Fourier spectrum of an image to recreate the missing high order components. In practice this means that the Fourier transform of the final image is taken, giving the information in equation (2.88). The finite transverse size of the imaging system means that information outside of $-\frac{a}{2} < x < \frac{a}{2}$ is lost. The Fourier transform can then be extrapolated to recover this lost information. In theory this allows the high order information to be retrieved and allows the sharp edges of the slit to be regained in the post-processed image.

In practice, since the extrapolation is an ill-posed problem [115, 116], the analytical reconstruction is very sensitive to noise. As such even a small amount of noise will place a limit on the achievable level of super-resolution. As we have seen, light always has a certain level of quantum noise. This leads to a standard quantum limit (SQL) for the achievable level of super-resolution. In the case of a slit as described above, the image can be deconstructed on a set of prolate spheroidal functions as the eigenvectors [117, 118]. From this deconstruction the eigenvalue corresponding to the smallest spatial feature can be derived by setting the signal-to-noise ratio to be unity [73]. This eigenvalue is given by

$$\lambda_Q \approx \frac{e^{-2s}}{4\langle n \rangle}, \tag{2.89}$$

where $\langle n \rangle$ is the total number of photons in the field illuminating the object, and s is the squeezing parameter. If the light used is a coherent laser field then $s = 0$, if the light is amplitude squeezed then $s > 0$. Either by numerical calculation, or by using tables of eigenvalues [118], the index Q of the eigenvalue λ_Q can be found. Using this, it is possible to estimate the resolution length as [73]

$$D = \frac{\lambda f}{a}\left(\frac{\langle n \rangle}{Q+1}\right). \tag{2.90}$$

Thus to improve the achievable resolution either $\langle n \rangle$ must be increased, or s must be increased, which results in a decrease in Q. In the case of classical light $s = 0$, and so to increase resolution only $\langle n \rangle$ can be increased, achieved by increasing the light power. However, particularly in biological imaging, some objects are sensitive to light, and may be destroyed if exposed to very intense light power, placing an upper limit to the number of incident photons $\langle n \rangle$.

Alternatively a squeezed light source can be used, giving $s > 0$. If this light source was a SSM squeezed state, then only a single spatial frequency would have a reduced noise, and as such the Fourier reconstruction would still be significantly hindered by the quantum noise in other spatial modes that are not squeezed. Instead MSM squeezed light must be utilised [115].

Currently MSM squeezed light sources are in their infancy, with some MSM sources being investigated. However in all cases there have been significant limitations on these states. Many PDC systems have been used in pulsed regime [55, 62, 119]. In the area of bright field quadrature squeezing PDC has been used to produce few-spatial-mode squeezed states with the use of confocal cavities. However, this method is experimentally challenging, and produces only low levels of squeezing [75–79]. 4WM has previous been used to produce a larger 12 spatial-mode squeezed state [84], where, in this case all the modes were symmetric.

It is in the area of generating such MSM squeezed light that this thesis is focused. In the experimental section (section 4.5) of this thesis, I present the production and characterisation of a 75 spatial-mode quadrature squeezed state. In this experiment, the only restriction placed on the squeezed modes is that they are larger than the coherence area. In chapter 5, I discuss the initial work towards imaging such MSM squeezed light, and measuring reduced quantum fluctuations between images.

CHAPTER 3

GENERATION OF SQUEEZED LIGHT WITH NONLINEAR OPTICS AND ITS MEASUREMENT

3.1 Introduction

Amplifiers such as those described in section 2.4 can be created using nonlinear media, such as parametric down conversion (PDC) in crystals and four wave mixing (4WM) in hot atomic vapours. In this chapter, I will introduce the concept of nonlinear optics, and discuss how it can be used to generate entangled and squeezed fields. I will discuss PDC, and why it is challenging to use PDC for the generation of MSM squeezed fields. I will move on to discuss 4WM and how this is more readily suited to the generation of MSM squeezed fields. I will also discuss the many complications arising from the use of 4WM in hot rubidium vapours, and how these challenges can be overcome.

3.2 Nonlinear optics

In this section I discuss the interactions between light and dielectric media. I begin with discussing the case of linear media, and move on to discussing nonlinear optics. Here I include a brief description of the relevant linear and nonlinear optics, more detailed treatments can be found in the literature [95, 120, 121].

A light field incident on a dielectric medium induces a dipole moment in the media, which acts as an additional light source. In general the dipole moment per unit volume, or polarization, $\wp$, of a system can be written as

$$\wp = \epsilon_0 \chi E, \tag{3.1}$$

where ϵ_0 is the permittivity of free space, and E is the electric field. χ is a property of the dielectric medium called the susceptibility. The dipole moment causes a change to the electric field in the media according to

$$\frac{dE}{dt} = \frac{ik}{2\epsilon_0}\wp, \tag{3.2}$$

where k is the wave vector of the light.

In linear optics the first order susceptibility is used, $\chi = \chi^{(1)}$, and the polarization becomes

$$\wp_L = \epsilon_0 \chi^{(1)} E. \tag{3.3}$$

The first order susceptibility is responsible for the index of refraction, n, of a medium and its optical absorption, α. This are described by the real and imaginary parts of the susceptibility respectively,

$$n = \mathbf{Re}\left(\chi^{(1)}\right), \tag{3.4}$$

$$\alpha = \mathbf{Im}\left(\chi^{(1)}\right). \tag{3.5}$$

In nonlinear media there is an additional nonlinear component to the polarisation $\wp_{NL}$, making the total polarisation $\wp = \wp_L + \wp_{NL}$, where

$$\wp_{NL} = \epsilon_0 \left(\chi^{(2)} E^2 + \chi^{(3)} E^3 + ...\right) \tag{3.6}$$

In the majority of media, the susceptibilities become increasingly small with increasing order, due to the increased numbers of photons involved in each interaction. In most media these susceptibilities are negligible, these are the linear media. However, in some media, these coefficients can be larger than normal, causing the nonlinear polarisation to be of a comparable magnitude to the linear polarisation. In some crystals the $\chi^{(2)}$ coefficient becomes large. These media can then support PDC. In hot atomic vapours, due to their centro-symmetry, the even order susceptibilities become zero. Thus, since $\chi^{(2)} = 0$, the $\chi^{(3)}$ coefficients are the leading order nonlinearity, creating 4WM interactions.

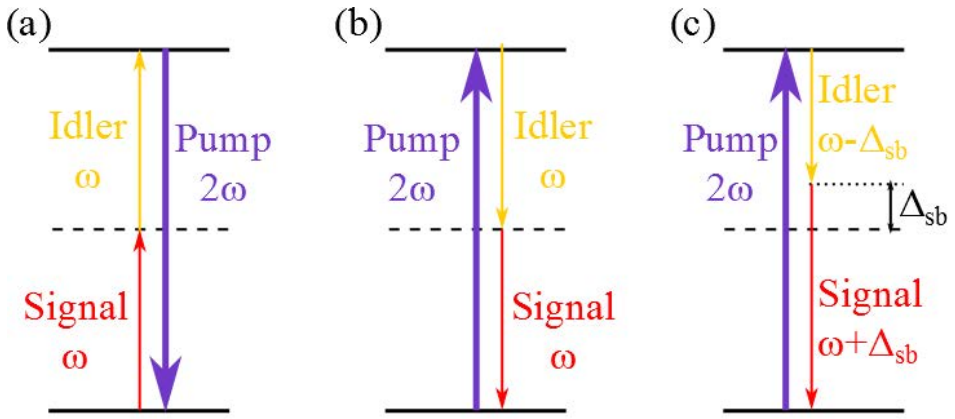

Figure 3.1: The energy level systems for a $\chi^{(2)}$ medium. (a) when two photons at frequency ω are frequency doubled to a single photon at frequency 2ω. (b) the reverse process where PDC is used to convert a single pump photon at frequency 2ω to a pair of signal and idler photons at frequency ω. (c) the case of non-degenerate PDC, with a frequency splitting of $2\Delta_{sb}$ between the signal and idler photons.

3.3 Parametric down conversion

Consider two electric fields, oscillating on the same frequency, $E = 2E_0 (\cos \omega t)$, that are propagating in a $\chi^{(2)}$ medium. The polarisation of the system is

$$\wp_{NL} = \epsilon_0 \left(\chi^{(1)} 2E_0 (\cos \omega t) + \chi^{(2)} 4E_0^2 \cos^2 \omega t \right) \tag{3.7}$$

$$= \epsilon_0 \chi^{(1)} 2E_0 \cos \omega t + \epsilon_0 \chi^{(2)} 2E_0^2 (\cos 2\omega t + 1) \tag{3.8}$$

The polarisation now contains the additional frequencies of 2ω and a DC field, as well as the original frequency ω. If the $\chi^{(2)}$ coefficient is non-zero, then the medium converts some of the incident light from frequency ω to 2ω. In this way, nonlinear processes in optics can be used to double the frequency of a field. Similar $\chi^{(2)}$ processes can be used for PDC, and sum and difference frequency generation [122]. The atomic energy scheme as used for converting pairs of photons at ω into single photons at 2ω, and the reverse process, of PDC, are shown in figure 3.1.

The process of PDC, whereby one pump photon is taken and split into a signal and an idler photon, can be thought of as a photon pair generator. As such, the process inherently produces photon pairs. The photons will have correlated momenta and frequency, due to conservation of momentum and energy. In this form, PDC in a $\chi^{(2)}$ medium creates a two mode amplifier, which can be used to generate squeezing as explained in section 2.4. The intrinsic gain of the PDC process is very low, due to the process involving only a virtual intermediate state, far detuned from any atomic resonance.

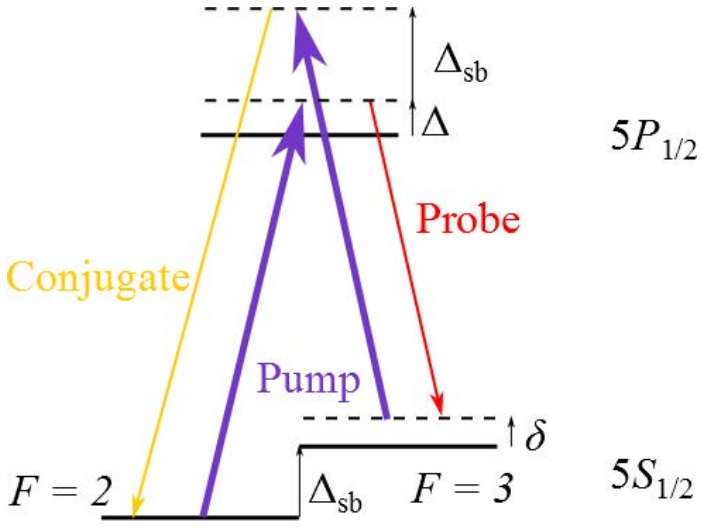

Figure 3.2: The ^{85}Rb D1 level diagram, as used for 4WM. Exact transition frequencies can be found in [123].

3.4 Four-wave mixing

The 4WM process is a nonlinear process using the $\chi^{(3)}$ nonlinearity. This susceptibility couples four separate fields, instead of the three fields used in PDC. In our case the additional field is a second pump field. In practice the two pump photons can be taken from a single pump laser field. Conservation of energy requires that the total energy of the absorbed pump photons must equal the total energy of the emitted probe and conjugate photons. The 4WM process is, like PDC, a parametric process, which means that after the 4WM cycle the atom returns to the very same state that it was in before the 4WM cycle. The double lambda level structure of our medium, rubidium 85, which is shown in figure 3.2, leads to a strong $\chi^{(3)}$ coefficient. This is explored further in our paper [124], where the gain of the 4WM process is mapped, as a function of angle and two-photon detuning.

The presence of the strong pump fields initially prepares the atomic vapour in the upper ground state, due to the larger detuning of pump transition from this state to the excited state, compared to that of the lower ground state. This is the start point of the 4WM cycle. It starts with a two photon transition into the lower ground state, where one pump photon is absorbed, and one conjugate photon is emitted. When in the lower ground state, the atom is immediately pumped back into the upper ground state through a two photon transition, absorbing a pump photon, and emitting a probe photon. This process can be thought of as near instantaneous, due to the ratio between the detunings of the intermediary excited states.

A full mathematical treatment of the 4WM system in a double lambda system has been published by Lukin [125]. He calculates susceptibilities by considering the density matrix equations of the double lambda

level structure. These susceptibilities are then used with Maxwell's equations, as defined in equation (3.2), to give propagation equations, for the probe and conjugate fields, in the medium. A brief outline of the pertinent points of this description follows.

Mathematically the 4WM gain process is described by the system of equations

$$\frac{\partial}{\partial z}\mathcal{E}_p = \frac{ik_p}{2\varepsilon_0}\wp_p(\omega_p) \tag{3.9}$$

$$\frac{\partial}{\partial z}\mathcal{E}_c = \frac{ik_c}{2\varepsilon_0}\wp_c(\omega_c), \tag{3.10}$$

where

$$\wp_p(\omega_p) = \varepsilon_0\chi_{pp}(\omega_p)\mathcal{E}_p + \varepsilon_0\chi_{pc}(\omega_p)\mathcal{E}_c^{\dagger}e^{i\Delta\mathbf{k}\cdot\mathbf{r}} \tag{3.11}$$

$$\wp_c(\omega_c) = \varepsilon_0\chi_{cc}(\omega_c)\mathcal{E}_c + \varepsilon_0\chi_{cp}(\omega_c)\mathcal{E}_p^{\dagger}e^{i\Delta\mathbf{k}\cdot\mathbf{r}}. \tag{3.12}$$

$\mathcal{E}_p$ and $\mathcal{E}_c$ are the fields of the probe and conjugate respectively. The term $\Delta\mathbf{k}\cdot\mathbf{r}$ is the geometric phase term. The terms $\chi_{pp}(\omega_p)$ and $\chi_{cc}(\omega_c)$ are referred to as direct terms. These are the linear susceptibilities of the atomic medium to the probe and conjugate fields respectively. Here they are responsible for absorption (the real part) and for dephasing (imaginary parts), with the probe term being much stronger than the conjugate $\chi_{pp}(\omega_p) \gg \chi_{cc}(\omega_c)$. The $\chi_{pc}(\omega_p)$ and $\chi_{cp}(\omega_c)$ are referred to as cross terms, and arise from the full 4WM process whereby a pair of two photon transitions happen simultaneously, and two pump photons are converted into a pair of twin probe and conjugate photons. These describe the response of the χ^3 susceptibilities in the dressed 4WM system [125]. We have published an extensive study on the meanings of the different susceptibilities [124]. Combining these expressions gives

$$\frac{\partial}{\partial z}\mathcal{E}_p = \frac{ik_p}{2}\chi_{pp}(\omega_p)\mathcal{E}_p + \frac{ik_p}{2}\chi_{pc}(\omega_p)e^{i\Delta\mathbf{k}\cdot\mathbf{r}}\mathcal{E}_c^* \tag{3.13}$$

$$\frac{\partial}{\partial z}\mathcal{E}_c = \frac{ik_c}{2}\chi_{cc}(\omega_c)\mathcal{E}_c + \frac{ik_c}{2}\chi_{cp}(\omega_c)e^{i\Delta\mathbf{k}\cdot\mathbf{r}}\mathcal{E}_p^*. \tag{3.14}$$

These equations can be simplified by considering just the full 4WM process, and thus taking the direct terms (χ_{pp} and χ_{cc}) to zero, and using $\chi_{cp}(\omega_c) = \chi_{pc}^{\dagger}(\omega_p)$. The term $\Delta\mathbf{k}\cdot\mathbf{r}$ is the geometric phase term, containing only the vacuum wave vectors, and can be absorbed as $\mathcal{E}'_{p,c} = \mathcal{E}_{p,c}e^{-i\Delta\mathbf{k}\cdot\mathbf{r}/2}$. The probe and conjugate can be assumed to have similar wave vectors $\frac{k_c}{k_p} \approx 1$. Finally, with the substitution $\frac{s}{L} = \frac{ik_p}{2}\chi_{pc}(\omega_p)$, these equations

simplify as

$$\frac{\partial}{\partial z}\mathcal{E}_p = \frac{s}{L}\mathcal{E}_c^* \tag{3.15}$$

$$\frac{\partial}{\partial z}\mathcal{E}_c = \frac{s}{L}\mathcal{E}_p^*. \tag{3.16}$$

Solving these equations with input states $\mathcal{E}_c(0)$, and $\mathcal{E}_p(0)$, a solution for the output states, after a length L, becomes

$$\mathcal{E}_p(L) = \mathcal{E}_p(0)\cosh s + \mathcal{E}_c^*(0)\sinh s \tag{3.17}$$

$$\mathcal{E}_c(L) = \mathcal{E}_p^*(0)\sinh s + \mathcal{E}_c(0)\cosh s. \tag{3.18}$$

These equations are exactly those of the phase-insensitive TMSS amplifier, of length L, described in equations (2.18) and (2.19). Thus the 4WM can be used to produce exactly the two-mode squeezed state that we saw in section 2.4. This 4WM process has a high intrinsic gain, due to it operating near atomic resonance.

3.5 Four-wave mixing vs parametric down conversion for quantum optics

PDC currently holds the record for the largest QNR in a quadrature squeezed state at -12dB [31, 32]. However, in order to achieve this level of QNR, the process requires a large intensity gain, of the order of 5. To achieve this, the low intrinsic single pass gain of PDC is increased by the use of a cavity. However, a cavity restricts the spatial modes on which the process can operate. Normally a cavity will only support a single transverse spatial mode at a given frequency. Thus any squeezed light produced with this method can only be squeezed on a single transverse spatial mode. It has been possible to use spatially degenerate cavities, such as confocal, or self-imaging cavities, to extend the useful number of spatial modes up to 3, but only with a relatively weak level of squeezing [79, 126].

By contrast, 4WM is intrinsically a high gain process for which a hot atomic medium is often used. The high single pass gain of the 4WM process means that no cavities are needed to generate strong squeezing. This allows the process to generate localised squeezing on multiple independent transverse spatial modes. However, the 4WM process to date has only produced -4 dB [44] of squeezing and it can also introduce further complications.

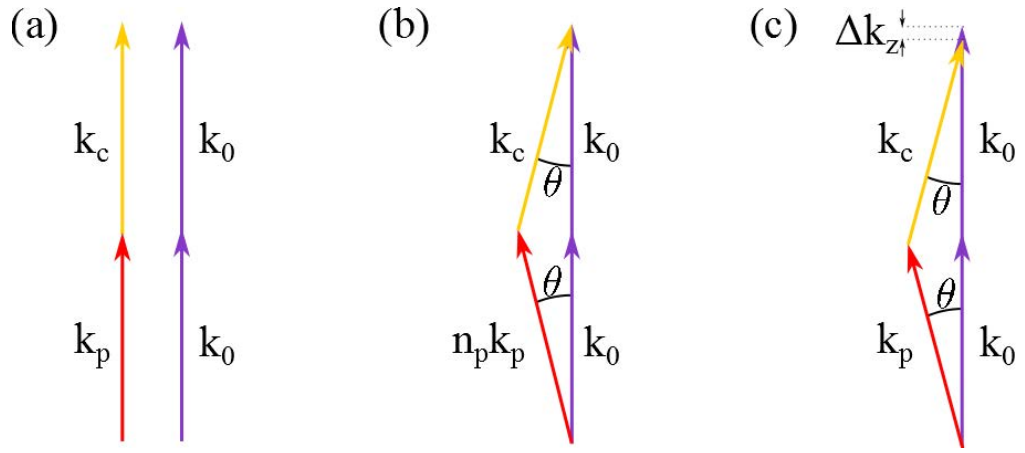

Figure 3.3: The phase matching condition in free space and in the atomic medium. (a) The fulfilment of the geometric phase-matching condition ($\Delta k_z = 0$), where the process happens in free space. (b) The phase-matching condition in the 4WM medium, where the index of refraction of the probe is increased by the medium. (c) The geometric phase mismatch $\Delta k_z > 0$, in the case of a small angle between fields.

Where PDC can be tuned to produce two entangled fields with very similar frequencies, the 4WM process, that we use, entangles two frequencies that are separated by 6 GHz. Thus, when these fields are used to generate quadrature squeezing in a single mode, it is also across distant sidebands. In the coming sections, I will discuss the implications that this has on the detection of the squeezed state.

Due to conservation of momentum, the 4WM system also has a phase matching condition (figure 3.3), which, in the case of a strong pump field, causes a gap in the far field gain spectrum (as seen below). Thus, the twin entangled fields, of the TMSS, propagate in slightly different directions. In the next section, I will discuss this phase matching condition further.

Overall, 4WM in hot atomic vapours presents a promising medium for the generation of continuous variable MSM quadrature squeezed light. This is despite PDC currently achieving significantly stronger squeezing than 4WM on a single spatial mode and the additional complications of 4WM. The suitability of 4WM for MSM squeezed light generation is due to the 4WM process not requiring the use of a cavity to produce strong quadrature squeezing.

3.6 Four-wave mixing phase matching condition

Due to the fundamental requirements of energy and momentum conservation, there is a phase matching condition associated with the 4WM process. The total momentum of the two pump photons must be matched by that of the probe and conjugate photons. In free space, the phase matching condition simply requires that

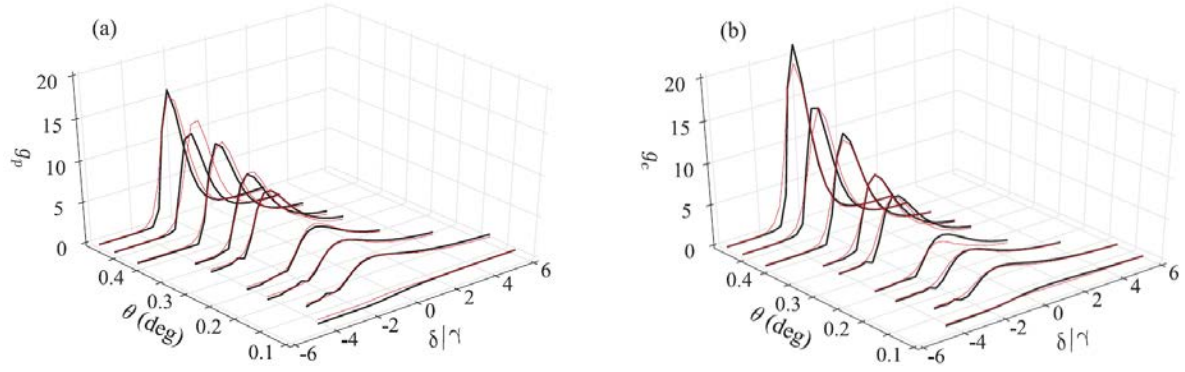

Figure 3.4: Figure from our phase matching paper [124], showing the experimental and theoretical results. The data is fitted for small angles both for the probe gain g_p (a) and the conjugate gain g_c (b). The thick black lines show the theoretical model; the thin red lines show the data. The fit is of good quality except for the smallest angle, where the probe and conjugate power measurements are polluted by pump leakage through the output polariser. For $\theta > 0.5°$, the model predicts gains much larger than those measured.

the fields are all rigorously co-propagating (figure 3.3(a)). However, because most of the atoms are in the upper ground state, the probe field is close to the atomic resonance in the gain medium, which increases the refractive index. This modifies the effective phase matching condition, as shown in figure 3.3(b). This can be thought of as the equivalent of requiring a small geometric phase mismatch Δk_z in free space (figure 3.3(c)). Meeting the modified phase matching condition requires a small angle θ to be introduced between the probe and pump, and correspondingly between the conjugate and pump. Previously this feature has been studied, initially by Boyer et al. working within NIST [127], and later more thoroughly in our own group [124]. In this paper the 4WM gain feature, as described by equations (3.13) and (3.14), was explored both theoretically and experimentally. The susceptibilities, and their variation with one-photon detuning Δ, were also studied in this paper. The gain was mapped, with changing two-photon detunings, δ, and angles between the probe and pump fields, θ. The results are plotted both experimentally and theoretically in figure 3.4.

The modified phase matching condition results in reduction in the far field gain near to the pump field (figure 3.5). Additionally, there is a technical limitation due to the inability to fully filter out the pump light, resulting in some pump light leakage leaving a region around the central pump axis where squeezing cannot be observed. This creates effective restricted gain regions (RGRs) for the probe and conjugate fields that travel along different propagation axes. This means that the 4WM system produces the far field entanglement shown in figure 2.8(b) not figure 2.8(a). Thus, the complications arising in generating the squeezed field are those explained in section 2.6.4. In order to ensure that the two entangled fields, of the TMSS, propagate along a new shared axis they are brought on top of each other with a set of mirrors, and combined on a beam splitter, completing the action shown in figure 2.9(b).

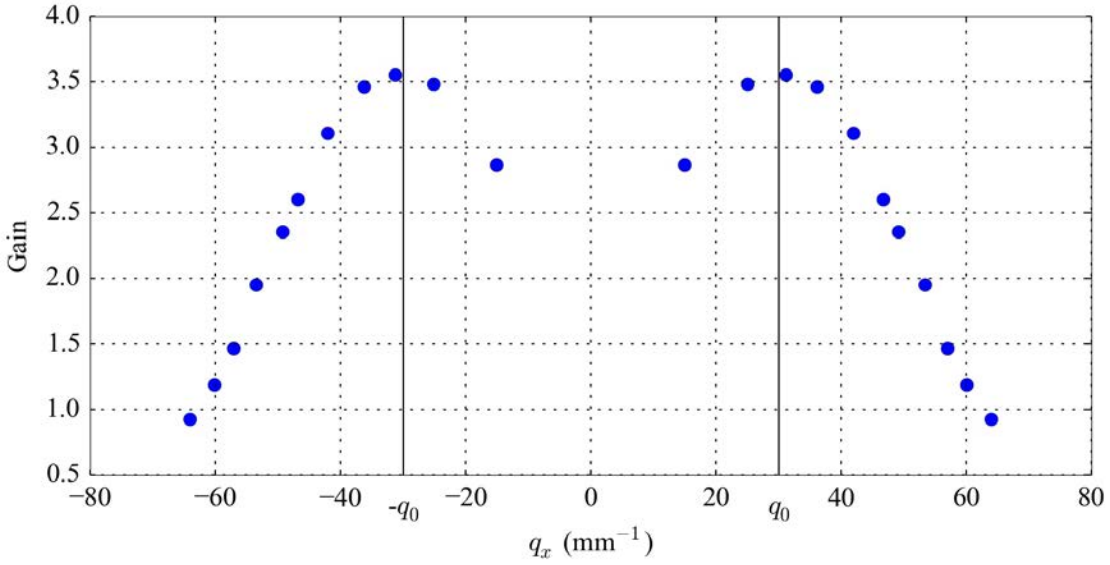

Figure 3.5: The near-field gain spectrum from the 4WM process, as measured as a function of angle, θ, in the far field. The angle is converted into a transverse wavevector, taken perpendicular to the pump.

3.7 Detection of squeezed states

The intensity of the light field can be described by the operator $\hat{I} \propto \hat{E}^{(-)}\hat{E}^{(+)}$ [128], where $E^{(+)} \propto \hat{a}$, and $E^{(-)} \propto \hat{a}^\dagger$ [129]. Neglecting the constants of proportionality the mean value of the intensity can be found as the expectation value

$$I = \left\langle \hat{a}^\dagger \hat{a} \right\rangle . \tag{3.19}$$

The fluctuations in the intensity of the light field are given by

$$\Delta\hat{I} = \sqrt{\left\langle \hat{I}^2 \right\rangle - \left\langle \hat{I} \right\rangle^2} \tag{3.20}$$

$$= \sqrt{\langle \hat{a}^\dagger \hat{a} \hat{a}^\dagger \hat{a} \rangle - \langle \hat{a}^\dagger \hat{a} \rangle^2}. \tag{3.21}$$

A perfect photodetector converts the intensity $\hat{I}$ from the light field into a photocurrent $\hat{i}_p$ as $\hat{i}_p = \hat{I} = \hat{a}^\dagger \hat{a}$, again neglecting the constants of proportionality. In reality all photodetectors have some finite quantum efficiency $\eta < 1$. This quantum efficiency can be treated as a beam splitter placed before a perfect detector, as shown in figure 3.6 An imperfect photodetector can be described by the operator $\hat{i} = \hat{a}_\eta^\dagger \hat{a}_\eta$, where

$$\hat{a}_\eta = \sqrt{\eta}\hat{a} + \sqrt{1-\eta}\hat{v}, \tag{3.22}$$

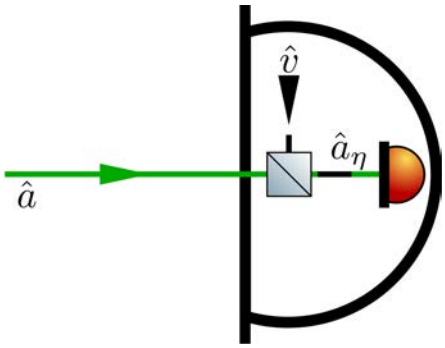

Figure 3.6: An imperfect photodetector (white detector) as modelled as a perfect photodetector (orange detector) with an additional beam splitter used to model the losses.

and $\hat{v}$ is the creation operator on the side of the beam splitter where a vacuum state will be applied. The mean value, and fluctuations of the imperfect photodetector are

$$\langle i \rangle = \eta \left\langle \hat{a}^\dagger \hat{a} \right\rangle \tag{3.23}$$

$$\left\langle \Delta \hat{i}^2 \right\rangle = \eta^2 \left\langle \Delta \hat{i}_p^2 \right\rangle + \eta \left(1 - \eta\right) \left\langle \hat{i}_p \right\rangle, \tag{3.24}$$

where the term $\eta^2 \left\langle \Delta \hat{i}_p^2 \right\rangle$ is the contribution from the field fluctuations, and $\eta \left(1 - \eta\right) \left\langle \hat{i}_p \right\rangle$ is an extra term due to the imperfect quantum efficiency [130]. In practice η can rise up to near unity, in the case of our detector this is 0.95. To simplify the theoretical derivations, throughout this chapter, this term will be assumed to be unity.

Losses on a signal field, for example from imperfect reflectivity on mirror surfaces, can be modelled in a similar fashion, with the inclusion of a beam splitter in the optical path. In such a model, the input operator $\hat{a}$ is modified by the loss to $\hat{a}_\eta$ according to equation (3.22), and the noise modified according to equation (3.24).

In this section, I shall discuss in more detail the detection of squeezed light. I shall begin by discussing the direct detection of squeezed light, using a photodiode, and the limitations of this method, and then move on to discuss the different configurations of homodyne detection, and their limitations.

3.7.1 Direct detection and unbalanced homodyne detection

Consider the measurement of a light field, this field usually has an amplitude and a phase which fluctuate with time. This noise will be made up of two components, the classical noise, arising from factors such as fluctuating laser power, and the quantum noise, which, ultimately, is due to the light being made up of

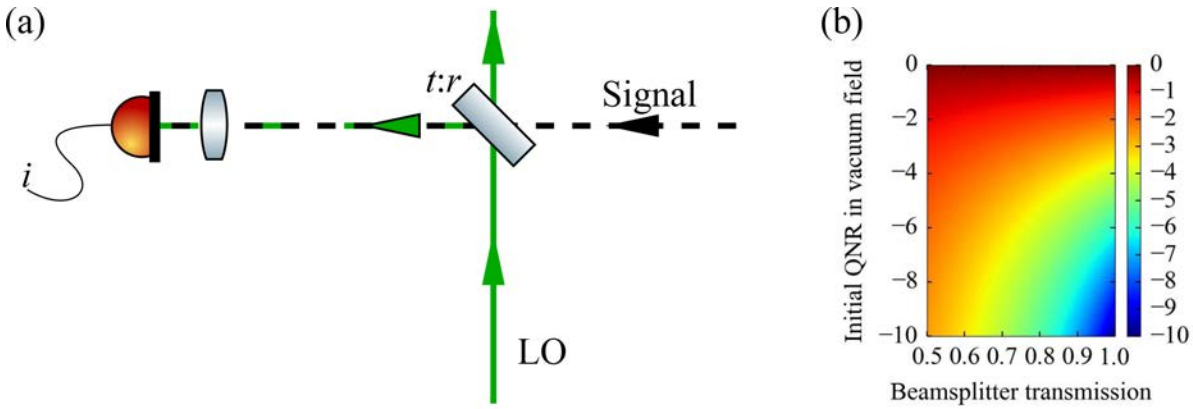

Figure 3.7: (a) An unbalanced homodyne detection system, where a signal is transmitted through a beam splitter with transmission t, and LO is reflected with reflectivity r. (b) The resultant QNR measured as a function of the beam splitter transmission and the initial QNR in the signal.

photons. In classical physics, the light can be split into smaller and smaller parts. As this happens the classical noise is split in the same proportion as the intensity of the light field. Whilst the classical noise is proportional to the intensity of a field, the quantum noise is proportional to the amplitude of the field. As such, when a light field is attenuated, the quantum noise will be reduced proportionally to the amplitude of the field. Consequently, when a field is attenuated the classical noise is reduced more than the quantum noise, and so the field is brought closer to the QNL. In general, the classical noise on a light field will be larger than the quantum noise.

A quadrature squeezed vacuum signal has too little power to be detected directly with a photodiode. Instead, one can first amplify the quadrature squeezed signal with a local oscillator (LO). To achieve this, the fields are overlapped on a beam splitter (figure 3.7(a)), which has a high transmission of the signal field $t = \sqrt{1-\epsilon}$, and a low reflection of the LO, $\sqrt{\epsilon}$. The second output from the beam splitter is ignored. Assuming that the quadrature squeezed field, called the signal field, is generated as discussed in section 2.3, it can be described by the operator

$$\hat{a}_s = \hat{a}\cosh s + \hat{a}^\dagger \sinh s. \tag{3.25}$$

The LO field can be described by the operator b, where $\langle b \rangle = |\beta|\, e^{i\phi_{LO}}$. $|\beta|$ is the amplitude of the LO field and ϕ_{LO} is the phase of the field.

With these LO and signal inputs, the field at the output of the beam splitter is given by

$$\begin{aligned}\hat{a}_{out} &= \sqrt{1-\epsilon}\hat{a}_s + \sqrt{\epsilon}\hat{b} \\ &= \sqrt{1-\epsilon}\left(\hat{a}\cosh s + \hat{a}^\dagger \sinh s\right) + \sqrt{\epsilon}\hat{b}. \end{aligned} \tag{3.26}$$

The combined field, after the beam splitter, will be a bright quadrature squeezed field. The quantum noise reduction (QNR) of the resultant field will depend on the initial level of squeezing in the signal field and the splitting ratio of the beam splitter. The fluctuations on the resulting photocurrent can be found, using equation (3.21), to be

$$\left\langle \Delta\hat{I}^2_{out} \right\rangle = (1-\epsilon)^2 \left\langle \Delta\hat{I}^2_s \right\rangle + \epsilon^4 \left\langle \Delta\hat{I}^2_{LO} \right\rangle + \beta^2\epsilon\,(1-\epsilon)\left(e^{2s}\cos^2\phi_{LO} + e^{-2s}\sin^2\phi_{LO}\right), \tag{3.27}$$

where, $\left\langle \Delta\hat{I}^2_s \right\rangle$ and $\left\langle \Delta\hat{I}^2_{LO} \right\rangle$ are respectively the signal and LO intensity fluctuations. In the limit of a strong LO, the signal fluctuations,$\left\langle \Delta\hat{I}^2_s \right\rangle$, are small compared to the other terms. In the ideal case, the LO fluctuations, $\left\langle \Delta\hat{I}^2_{LO} \right\rangle$, would be at the SN level $\mathcal{N}_{SN}$, but are likely to be limited by some classical noise. The QNR of this field, assuming that the LO is at the QNL, is shown in figure 3.7(b), and is similar to the effect of losses on the squeezed field.

The combined bright quadrature squeezed field can then be detected, using a photodetector. This detection method, involving mixing a signal field with a bright LO on an unbalanced beam splitter, is called unbalanced homodyne detection. To maximise the measured squeezing, the beam splitter should be chosen to transmit the vast majority of the squeezed light, and a minimal amount of the LO. However, the beam splitter should also be chosen such that the mean intensity of the output is still dominated by the LO intensity. This method of unbalanced homodyne detection is very effective in the case of a LO field that is at the QNL. However, in practice, any bright laser field is liable to contain a relatively large level of classical noise. In this case, the classical noise will dominate over the quantum noise in the detection, which makes measuring the quantum noise very difficult through this detection method.

3.7.2 Balanced detection, shotnoise and entanglement

Any classical noise on a field can be removed from detection by splitting a field equally on a 50:50 beam splitter, and aligning each output path to be incident on two detectors. The photocurrents from these detectors can be subtracted $i_- = i_1 - i_2$. This is called a differential detector and is shown in figure 3.8(a). Consider this detection scheme with only a bright field. Classically, half the light is incident on each side of

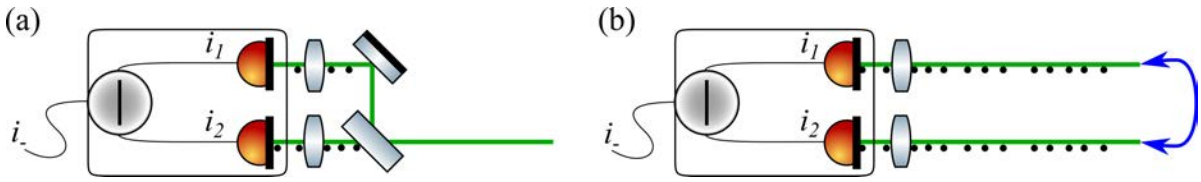

Figure 3.8: (a) A laser split into half at a beam splitter, with each half incident on one side of a differential detector. Each photon (depicted as black dots) can only be detected on one side of the differential detector, resulting in the shot noise. Any classical noise on the LO will be split equally at the beam splitter, and thus will be cancelled out on detection. (b) Two entangled fields, each incident on one side of the differential detector. The photons arrive at the detector in pairs, so that there is no noise measured on the subtracted photocurrent i_-.

the differential detector, and thus the measured photocurrent will be zero. This 50:50 splitting also extends to any classical noise on the coherent field. As such this detection scheme has perfect common mode rejection of the classical noise.

Quantum mechanically, each photon that reaches the beam splitter can only be measured at one of the two detectors. Consequently, quantum noise will still be present on the subtracted photocurrent (figure 3.8(a)). This noise will be the SN of the bright field.

Now consider a pair of perfectly entangled fields. The number of photons at any point in one field will be the same as the number present in the other field at the correlated position. If the correlated fields are aligned to be incident on opposite sides of the differential detector (figure 3.8(b)), then each detector will necessarily see the same number of photons at any given moment in time. Hence, in the case of perfect entanglement, the subtracted photo current will have no noise. In this configuration the noise on the detector, compared to that of a coherent field with the same total intensity, will show the intensity difference squeezing between the entangled fields. The same detection scheme extends to the measurement of continuous variable entanglement, such as that produced by a 4WM system. In practice, in order to generate bright entangled fields, the 4WM process needs to be seeded, on either the probe or conjugate frequencies. As such there will be a power imbalance, resulting in imperfect intensity difference squeezing. The level of intensity difference squeezing in the seeded case is given in equation 2.24.

3.7.3 Homodyne detection

Consider the case where a bright field is split on a 50:50 beam splitter with each output incident on a differential detector as in figure 3.8(a). Following the principles of section 3.7.1 and figure 3.7(a), a squeezed vacuum field can be introduced on the open port of the beam splitter, as shown in figure 3.9. Here the bright coherent field, called the LO, amplifies the vacuum fluctuations, called the signal, (either squeezed or

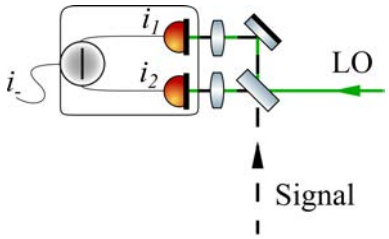

Figure 3.9: A typical homodyne detection setup. A LO is mixed with a signal field on a 50:50 beam splitter. The LO amplifies the noise of the signal field, whilst any classical noise on the LO is removed by the balanced detection.

otherwise) by beating against the vacuum field. The noise of the signal field is thus measured in the detection scheme. This detection method is balanced homodyne detection, and is often referred to as just homodyne detection.

It can be shown that balanced homodyne detection removes any noise contributions from the LO, whether they are classical or quantum [131]. Again, the LO field $\hat{E}_{LO}$ can be described by the operator $\hat{b}$, where $\langle b \rangle = |\beta| e^{i\phi_{LO}}$, and $|\beta|$ is the amplitude of the LO field and ϕ_{LO} is the phase of the field. Let's assume, once more, that the signal field is the output field from the squeezed light source discussed in section 2.3, and defined in equation (2.7). This field is referred to as the signal field and is described by

$$\hat{a}_s = \hat{a} \cosh s + \hat{a}^\dagger \sinh s, \tag{3.28}$$

fed by a vacuum state. This field is a vacuum field if $s = 0$, and is a squeezed vacuum field otherwise. When these fields are combined on a beam splitter, and set incident on a pair of detectors as shown in figure 3.9 the resultant field at each detector is

$$\hat{a}_{d1} = \frac{\hat{b} + \hat{a} \cosh s + \hat{a}^\dagger \sinh s}{\sqrt{2}} \tag{3.29}$$

$$\hat{a}_{d2} = \frac{\hat{b} - \hat{a} \cosh s - \hat{a}^\dagger \sinh s}{\sqrt{2}} \tag{3.30}$$

The subtracted photocurrent is given by

$$\hat{i}_- = \hat{a}^\dagger_{d1} \hat{a}_{d1} - \hat{a}^\dagger_{d2} \hat{a}_{d2} \tag{3.31}$$

$$= \left(\hat{a}^\dagger \hat{b} + \hat{b}^\dagger \hat{a} \right) \cosh s + \left(\hat{a} \hat{b} + \hat{b}^\dagger \hat{a}^\dagger \right) \sinh s. \tag{3.32}$$

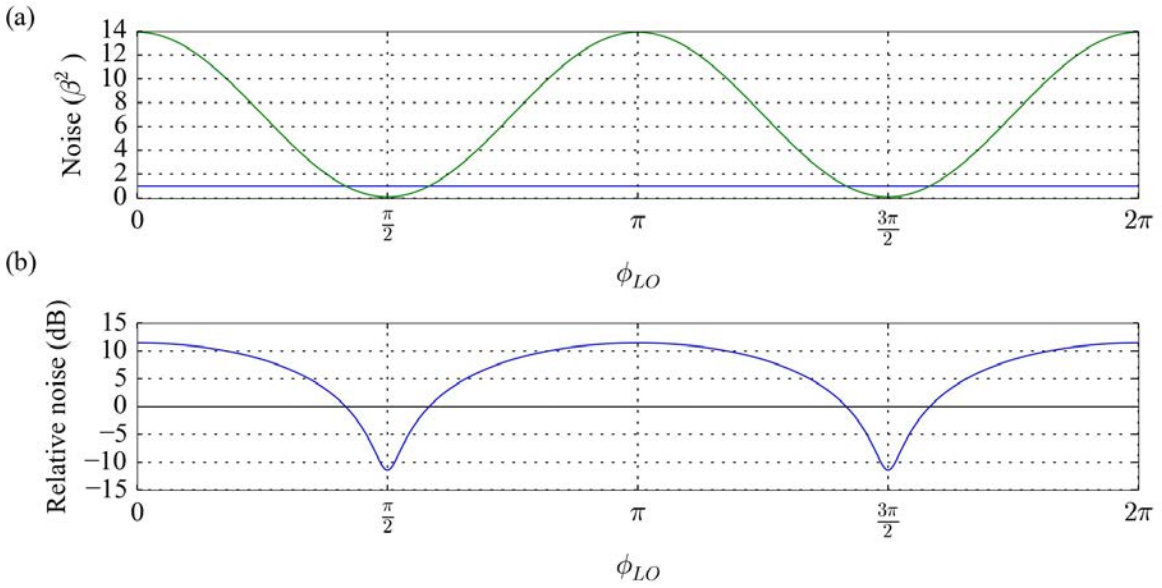

Figure 3.10: The noise of a squeezed state, as measured by a local oscillator of amplitude β, as the relative phase between the LO and signal field is scanned. (a) shows the noise power in units of β^2 for the SN in blue, and the squeezed state in green. (b) shows the squeezing QNR_{dB}, as defined in equation (2.6).

The noise on this photocurrent is thus

$$\left\langle \left(\Delta\hat{i}_-\right)^2 \right\rangle = \langle i_-^2 \rangle - \langle i_- \rangle^2 \tag{3.33}$$

$$\left\langle \left(\Delta\hat{i}_-\right)^2 \right\rangle = \beta^2 \left(e^{2s}\cos^2\phi_{LO} + e^{-2s}\sin^2\phi_{LO}\right) \tag{3.34}$$

$$= 4\beta^2 \left(\left\langle \Delta\hat{X}_s^2 \right\rangle \cos^2\phi_{LO} + \left\langle \Delta\hat{Y}_s^2 \right\rangle \sin^2\phi_{LO}\right). \tag{3.35}$$

The homodyne detection method amplifies the signal field, by a factor $4\left|\beta\right|^2$, ie. the intensity of the LO. The homodyne detector can be set to measure either the $\hat{X}$ or $\hat{Y}$ quadratures of the signal field, or indeed any quadrature in between, by setting the phase of the LO, ϕ_{LO}, with respect to the signal field. The homodyne detection method forms the main analytical technique used in this thesis, and is used to characterise the squeezed states that are generated experimentally in this thesis.

Consider the case of a theoretical quadrature squeezed light generator, such as that described in section 2.3, with a gain of 4. The full noise ellipse of the squeezed vacuum state can be mapped by rotating the LO phase ϕ_{LO}. When ϕ_{LO} is an integer multiple of π $(n\pi)$ $\left\langle \Delta\hat{X}_s^2 \right\rangle$ is measured, and when ϕ_{LO} is a half-integer multiple of π $((n+1/2)\pi)$ $\left\langle \Delta\hat{Y}_s^2 \right\rangle$ is measured. In this case, assuming $s > 0$, the noise measurement of the squeezed state, found using a homodyne detector would produce results as shown in figure 3.10. The top

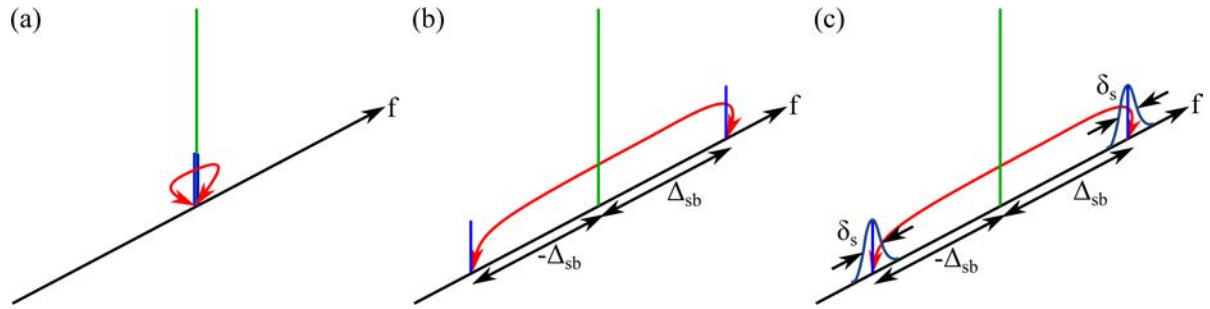

Figure 3.11: The sideband picture. The central frequency is marked in green, and would be the frequency of the LO necessary to measure the correlations. (a) Shows the situation where the sidebands are completely degenerate. QNR can be measured at an analysing frequency $\Delta_a = 0$ (b) Shows the correlated sidebands with a frequency separation $2\Delta_{sb}$ with each still assumed to be a single frequency. QNR can be measured at an analysing frequency $\Delta_a = \Delta_{sb}$ (c) Shows the sidebands over a correlated spectrum of frequencies. QNR can be measured at an analysing frequency in the range $\Delta_{sb} - \delta_s < \Delta_a < \Delta_{sb} + \delta_s$. The red arrows represent the correlations.

graph shows the absolute noise values in units of $|\beta|^2$, and the bottom graph shows relative noise between the squeezed state and the shot noise in dB, corresponding to the QNR according to equation 2.6. It is this QNR that will be investigated throughout this thesis.

3.7.4 Sideband picture

All squeezing can be seen as the correlations of fluctuations on a pair of sidebands. In a homodyne detection process, the total measured fluctuation, from the mean value, is the vector sum of the fluctuations on sidebands offset by the chosen analysing frequency, Δ_a, from the central frequency, ω_0, given by the LO. In order to complete a homodyne detection measurement the LO must be placed at the average frequency of these sidebands. In this thesis, the separation between sidebands generated in a gain process, such as 4WM, is given by $2\Delta_{sb}$, with each sideband located at $\omega_0 \pm \Delta_{sb}$. In a coherent state, the fluctuations on opposite sidebands are independent. However, in a squeezed state, the fluctuations on symmetric sidebands are correlated. The noise is increased on a quadrature if the fluctuations are in phase on this quadrature, or correlated. If fluctuations are out of phase on a quadrature, or anti-correlated, then reduced noise will be measured. In this way, the sideband picture can be used to describe the origins of squeezing.

The correlated sidebands can be localised to the same position, forming a SMSS, as in the near field in figure 2.8. Equally the sidebands could be in separate positions, as in a TMSS, the far field in figure 2.8(b). In either case the LO used to measure the squeezing must have an appropriate mode structure, matched to the mode structure of the squeezed state.

Up to this point the derivations in this thesis have excluded any reference to the frequency of the light. As

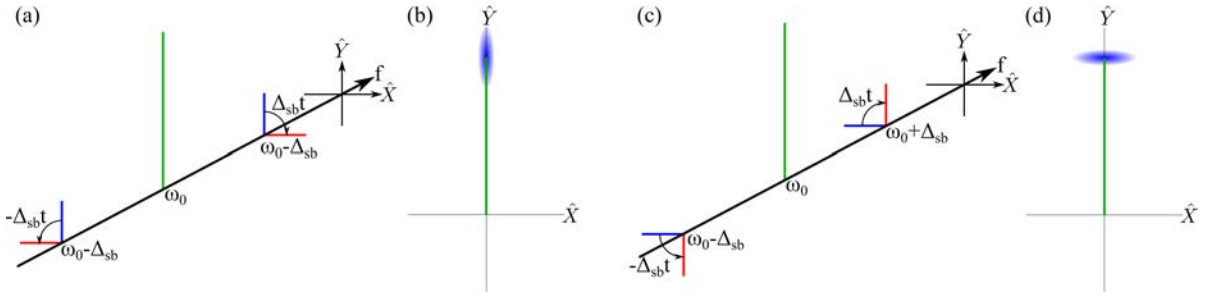

Figure 3.12: The sideband explanation of squeezing. Each sideband fluctuates around a mean value, zero in the case of vacuum fields. In (a) and (c) two fluctuations are shown, being a measure of the field quadratures at a given moment in time. The blue fluctuations are taken along the correlated quadrature, giving increased noise, whilst the red fluctuations are along the anti-correlated quadrature, giving QNR. (a) shows the fluctuations on the sidebands, being correlated in amplitude, and hence adding. The fluctuations are thus anti-correlated in phase, and subtract, giving phase squeezing, corresponding to $\phi_{LO} = 0$, π and 2π in figure 3.10. (b) shows the corresponding quadrature picture. (c) shows the fluctuations on the sidebands being correlated in phase, and anti-correlated in amplitude, giving amplitude squeezing, corresponding to $\phi_{LO} = \frac{\pi}{2}$ and $\frac{3\pi}{2}$ in figure 3.10. (d) shows the corresponding quadrature picture. The difference between (a) and (c) is a rotation of the LO by $\pi/2$.

such, they have implicitly assumed that all fields have the same frequency. This corresponds to a completely degenerate amplifier, ie. where the frequency detuning between the correlated modes is zero, $2\Delta_{sb} = 0$. Thus, in this case, both sidebands have the same frequency, which is also the frequency of the LO, ω_0. The derivations have also implicitly assumed that the gain process has an infinitely small bandwidth of the process. In this case, the squeezed region becomes a delta function (figure 3.11(a)). In such a situation, the analysing frequency must be set to zero, $\Delta_a = 0$, to measure any QNR. When departing from this theoretical system it is instructive to consider the sideband picture.

In a realistic system, technical noise means that the noise cannot be analysed at DC ie. $\Delta_a \neq 0$. In general the sidebands are non-degenerate fields, with some small separation, $2\Delta_{sb}$ (figure 3.11(b)). Additionally the squeezed region usually has some finite frequency bandwidth, δ_s, as represented in figure 3.11(c).

Consider measuring the noise of such systems, with distant sidebands, through homodyne detection with a single frequency LO. In this case the LO frequency must be set to the average of the two sideband frequencies and the noise analysed at $\Delta_a \approx \Delta_{sb}$. This places a requirement on the detector's electronic bandwidth, δ_d, that $\delta_d > \Delta_{sb}$.

When the frequency requirements are met, squeezing can be measured using homodyne detection, with a monochromatic local oscillator (MLO), centred at a frequency halfway between the correlated sidebands, at frequency ω_0. A spectrum analyser can be used to investigate the fluctuations in the frequency range $\Delta_{sb} - \delta_s < \Delta_a < \Delta_{sb} + \delta_s$. The two sidebands at a given analysing frequency, Δ_a, will rotate at frequency

$\omega_0 \pm \Delta_a$. Taking the central LO frequency as a reference, and working in the rotating frame, at this frequency (ω_0), the two sidebands can be seen to rotate in opposite directions at $\pm\Delta_a$.

Consider the case where the global phase is set such that the LO phase remains constant, $\phi_{LO} = \pi/2$. If the fluctuations on the sidebands are initially correlated in the $\hat{Y}$ quadrature, then an excess noise will be measurable on the amplitude quadrature, as measured by a photodetector. Correspondingly, the fluctuations will be anti-correlated on the $\hat{X}$ quadrature, allowing squeezing to be measured on the phase quadrature. The measured states are shown in (figure 3.12(a) and (b)). The excess noise can be brought onto the phase quadrature, and correspondingly the squeezing can be translated onto the amplitude quadrature by rotating the LO phase, and hence the global phase, through $\pi/2$ with respect to the signal fields, as shown in figure 3.12(c) and (d).

In systems such as those generated by PDC these requirement can be easily met, and there have been many experiments measuring squeezing in such systems [30–32, 63, 64, 69]. Squeezing across nearly degenerate sidebands can also be created in 4WM, and squeezing has been measured in such a system by Corzo et al. [84].

3.8 Bichromatic squeezing and detection

In principle MLOs, as described above, will always work. However, if Δ_{sb} is large, then the required detector bandwidth, δ_d, can be difficult to achieve, whilst retaining the necessary low technical noise and high gain of the detector. In the case of the 4WM system operated using ^{85}Rb, as is under investigation in this thesis (figure 3.2), the correlated sidebands, labelled probe and conjugate, are separated by 6 GHz. Thus, measurement with a single frequency LO would require a very fast photodetector $\delta_d > 3$GHz, with low noise, and a spectrum analyser able to analyse at $\Delta_a \approx 3$ GHz.

In order to reduce these technical requirements, a bichromatic local oscillator (BLO) can be employed, as has previously been proposed by Marino et al. [132]. This technique trades a single frequency LO at ω_0, with noise analysis at $\Delta_a = \Delta_{sb}$ (figure 3.13(a)), for a LO made up of two frequency components, one to beat with each frequency sideband (figure 3.13(b)). Initially let us retain the assumption that the system has no technical noise, and thus measurements at a DC analysing frequency are possible ($\Delta_a = 0$).

Following a similar derivation to Marino et al. [132], this method of using the BLO can be shown to be exactly equivalent to that of the single frequency LO (equation (3.34)), with some additional numerical factor. In order to complete this derivation, we must return to the description of the light field produced by the TMSS amplifier, described by equations (2.18) and 2.19. In the present case, with two colours, we must take care to keep track of the frequencies of the sidebands. When the entangled twin fields, of the TMSS,

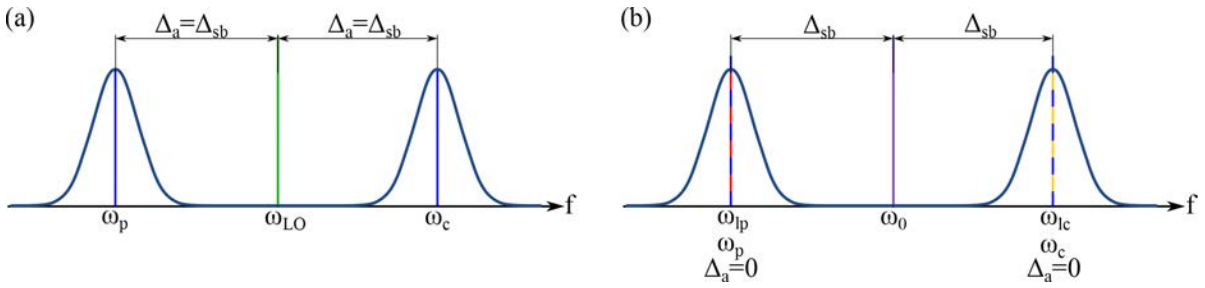

Figure 3.13: The sideband picture for (a) a single frequency LO with $\Delta_a = \Delta sb$, and (b) a bichromatic LO with $\Delta_a = 0$. In the two cases the measured squeezing is identical.

are mixed on a beam splitter the squeezed signal fields at the output are described by

$$\hat{a}_{s1} = \frac{1}{\sqrt{2}}\left(U\left(\hat{a}_1 e^{-i\omega_1 t} + \hat{a}_2 e^{-i\omega_2 t}\right) + V\left(\hat{a}_2^\dagger e^{i\omega_2 t} + \hat{a}_1^\dagger e^{i\omega_1 t}\right)\right) \tag{3.36}$$

$$\hat{a}_{s2} = \frac{1}{\sqrt{2}}\left(U\left(\hat{a}_1 e^{-i\omega_1 t} - \hat{a}_2 e^{-i\omega_2 t}\right) + V\left(\hat{a}_2^\dagger e^{i\omega_2 t} - \hat{a}_1^\dagger e^{i\omega_1 t}\right)\right), \tag{3.37}$$

where the labels ω_1 and ω_2 are taken with respect to the central frequency ω_0, such that $\omega_1 = -\omega_2 = \Delta_{sb}$, leading to $\omega_{c,p} = \omega_0 + \omega_{1,2}$, and $U = \cosh s$, $V = \sinh s$ as before. The BLO field is similarly described by

$$\hat{b}_{BLO} = \frac{1}{\sqrt{2}}\left(\hat{b}_1 e^{-i\omega_1 t} + \hat{b}_2 e^{-i\omega_2 t}\right), \tag{3.38}$$

where $\langle b_j \rangle = |\beta_j| e^{i\phi_j}$, with $j \in \{1, 2\}$. ϕ_j are the phases of the two LO frequency components, and $|\beta_j|$ are their amplitudes. Taking only one squeezed signal field, from one output port, $\hat{a}_{s1}$, as is done experimentally, the combined fields at each side of the differential detector, in a homodyne detection scheme, are given by

$$\hat{a}_{d1} = \frac{\hat{b}_{BLO} + \hat{a}_{s1}}{\sqrt{2}} \tag{3.39}$$

$$= \frac{1}{2}\left[\hat{b}_1 e^{-i\omega_1 t} + \hat{b}_2 e^{-i\omega_2 t} + U\left(\hat{a}_1 e^{-i\omega_1 t} + \hat{a}_2 e^{-i\omega_2 t}\right) + V\left(\hat{a}_2^\dagger e^{i\omega_2 t} + \hat{a}_1^\dagger e^{i\omega_1 t}\right)\right] \tag{3.40}$$

$$\hat{a}_{d2} = \frac{\hat{b}_{BLO} - \hat{a}_{s1}}{\sqrt{2}} \tag{3.41}$$

$$= \frac{1}{2}\left[\hat{b}_1 e^{-i\omega_1 t} + \hat{b}_2 e^{-i\omega_2 t} - U\left(\hat{a}_1 e^{-i\omega_1 t} + \hat{a}_2 e^{-i\omega_2 t}\right) - V\left(\hat{a}_2^\dagger e^{i\omega_2 t} + \hat{a}_1^\dagger e^{i\omega_1 t}\right)\right] \tag{3.42}$$

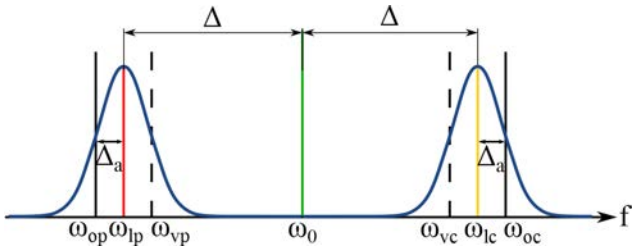

Figure 3.14: The frequency components of the squeezed field in blue, and BLO components $\omega_{lp,lc}$, with the probe frequency in red and conjugate frequency in yellow. The squeezing spectrum is analysed in object bands, $\omega_{op,oc}$, marked with the solid black lines and the image bands, $\omega_{vp,vc}$, marked with the black dashed lines. In the text the form of the detected noise is derived for $\Delta_a = 0$, and later quoted for $\Delta_a \neq 0$.

As before, the subtracted photocurrent can be calculated as

$$\hat{i}_- = \hat{a}_{d1}^\dagger \hat{a}_{d1} - \hat{a}_{d2}^\dagger \hat{a}_{d2} \tag{3.43}$$

$$= \frac{1}{4}\left[\hat{b}_1^\dagger e^{i\omega_1 t} + \hat{b}_2^\dagger e^{i\omega_2 t}\right]\left[U\left(\hat{a}_1 e^{-i\omega_1 t} + \hat{a}_2 e^{-i\omega_2 t}\right) + V\left(\hat{a}_2^\dagger e^{i\omega_2 t} + \hat{a}_1^\dagger e^{i\omega_1 t}\right)\right] \tag{3.44}$$

$$+ \frac{1}{4}\left[U\left(\hat{a}_1^\dagger e^{i\omega_1 t} + \hat{a}_2^\dagger e^{i\omega_2 t}\right) + V\left(\hat{a}_2 e^{-i\omega_2 t} + \hat{a}_1 e^{-i\omega_1 t}\right)\right]\left[\hat{b}_1 e^{-i\omega_1 t} + \hat{b}_2 e^{-i\omega_2 t}\right]. \tag{3.45}$$

Terms of the form $e^{\pm 2i\omega_1 t}$, $e^{\pm 2i\omega_2 t}$ and $e^{i(\omega_1 t - \omega_2 t)}$ oscillate quickly, and as such average out to zero. Thus the noise on the photocurrent can be calculated as

$$\left\langle \left(\Delta\hat{i}_-\right)^2 \right\rangle = \langle i_-^2 \rangle - \langle i_- \rangle^2 \tag{3.46}$$

$$= |\beta|^2 \left(e^{2s}\cos^2\left(\frac{\phi_1+\phi_2}{2}\right) + e^{-2s}\sin^2\left(\frac{\phi_1+\phi_2}{2}\right)\right), \tag{3.47}$$

where I have assumed that the power of the two frequency components of the LO field are identical, $|\beta_1| = |\beta_2| = \left|\frac{\beta}{\sqrt{2}}\right|$. This result can be directly compared with that in equation (3.34), and can be seen to be equivalent with the transformation $\phi_{LO} \to \frac{\phi_1+\phi_2}{2}$.

The equivalence between bichromatic homodyne detection and monochromatic homodyne detection is critical for the experiment, since it allows for the measurement of squeezing, where the correlated sidebands are separated by large frequency gaps.

In reality there are some additional complications. Firstly technical noise limits the detection, meaning that no noise measurement can be made at a DC value, ie. there is a requirement for $\Delta_a > 0$. It is important to remember that the field fluctuation at a given frequency, is given by the vector sum of the field fluctuations of the symmetric sidebands, $\omega_{lp} \pm \Delta a, \omega_{lc} \mp \Delta a$. As such, the fluctuations of two bands get measured at each of the probe and conjugate frequencies. These bands are the object band (at frequencies $\omega_{op} = \omega_{lp} - \Delta_a$ and

$\omega_{oc} = \omega_{lc} + \Delta_a$ with squeezing parameter s_o) and an additional image band (at frequencies $\omega_{vp} = \omega_{lp} + \Delta_a$ and $\omega_{vc} = \omega_{lc} - \Delta_a$ with squeezing parameter s_v), as shown in figure 3.14. If the probe and conjugate LO components are placed symmetrically about the pump frequency, at the centre of the squeezing spectrum, and if the analysing frequency is less than the squeezing bandwidth $\Delta_a < \delta_s$, then squeezing will be present in both the object and image bands. Such conditions can easily be met if the BLO components are generated through the use of a 4WM amplifier.

A second imperfection arises from the method of generation of the BLO field. By using the 4WM process, and seeding at only the probe frequency, the probe component of the BLO necessarily has a greater intensity than the conjugate component $\beta_2 > \beta_1$.

The derivation with these assumptions lifted is more complicated and has previously been published by Marino et al. [132], where they derive the fluctuations on the photocurrent to be

$$\begin{aligned}\left\langle (\Delta i_-)^2 \right\rangle =& 4\left|\beta_1\right|^2 \left\{ \left(1 + \frac{\delta\beta}{|\beta_1|}\right) \left[\left(e^{2s_o} + e^{2s_v}\right) \cos^2\left(\frac{\chi_p + \chi_c - \theta_s}{2}\right) \right.\right. \\ & \left. + \left(e^{-2s_o} + e^{-2s_v}\right) \sin^2\left(\frac{\chi_p + \chi_c - \theta_s}{2}\right) \right] \\ & \left. + \frac{1}{2}\left(\frac{\delta\beta}{|\beta_1|}\right)^2 \left(\cosh 2s_o + \cosh 2s_v\right) \right\}, \end{aligned} \tag{3.48}$$

where χ_p and χ_c are the relative phase difference between each LO component and its corresponding signal component, and $\delta\beta = \beta_2 - \beta_1$. There is a factor of 4 difference in normalisation due to the input states considered. This result shows that if only the first order of $\delta\beta/\left|\beta_1\right|$ is taken squeezing can still be measured with a BLO, in exactly the same way as a single frequency LO.

The use of this measurement makes the assumption that $\delta\beta/\left|\beta_1\right| << 1$. However, in the experiment, the BLO is formed through a seeded 4WM process. This means that $\beta_1 = \sqrt{(G-1)}\alpha_s$ and $\beta_2 = \sqrt{G}\alpha_s$, where α_s is the seed amplitude, and G is the 4WM intensity gain. Let us assume that $G = 4$, a realistic estimate of the gain given the experimental 4WM parameters, and for simplicity that $s_o = s_v = \cosh^{-1}\sqrt{G} \approx 1.3$. With these assumptions

$$\left(\frac{\delta\beta}{|\beta_1|}\right) = \frac{\sqrt{G} - \sqrt{G-1}}{\sqrt{G-1}} \tag{3.49}$$

$$= 0.15, \tag{3.50}$$

and the QNR on the photocurrent can be calculated, using equation (3.48), as

$$QNR_{dB} = \begin{cases} -8.45 \text{ dB} & \text{where } \chi_p + \chi_c = \theta_s \\ 11.42 \text{ dB} & \text{where } \chi_p + \chi_c = \theta_s + \pi. \end{cases} \tag{3.51}$$

The level of QNR can be compared to that if the two components had exactly the same power, ie. $\delta\beta = 0$, when

$$QNR_{dB} = \begin{cases} -11.44 \text{ dB} & \text{where } \chi_p + \chi_c = \theta_s \\ 11.44 \text{ dB} & \text{where } \chi_p + \chi_c = \theta_s + \pi. \end{cases} \tag{3.52}$$

As such it can be seen that, at a 4WM gain of 4, the method of using a BLO generated through a second 4WM process reduces the measurable QNR by roughly 3 dB.

This level of squeezing can be compared to the intensity difference squeezing produced, as given by equation (2.24). When the gain is 4, and both the object and image bands are considered, the intensity difference squeezing is -11.46dB. Thus, it can be seen that, the intensity difference squeezing and amplitude quadrature squeezing are comparable. It should be noted that when using a bichromatic homodyne detector, and a BLO formed through a separate 4WM process, there is some significant reduction in the measurable level of squeezing, associated with the power imbalance in the BLO frequency components. This reduction is dependent on both the BLO power imbalance and the initial level of squeezing. The effect of this loss on the experiment presented in this thesis, is discussed later in section 4.3.6.

3.9 Summary of experimental requirements

In this chapter, I have introduced nonlinear optics and discussed the 4WM process used to generate entangled fields. I have then outlined the complications arising from the use of non-degenerate 4WM, and the implications that it has for generating squeezing. Together all of these considerations generate a set of experimental requirements.

In order to create a pair of entangled fields, there must be a pump field of sufficient power tuned to a resonant frequency in a nonlinear medium. It must be possible to extract the remains of the pump light before performing any measurement on the twin fields, either by spatial separation, or polarisation, or a combination of the two. To generate squeezing the twin entangled fields must be well overlapped on a beam splitter. The resultant squeezed field can then be detected using a LO in a homodyne detection system. In the case of degenerate 4WM, if the squeezing is SSM, then the LO must be mode matched with that squeezed

mode. If the signal field is a MSM squeezed field, then this condition is relaxed. In the case of nondegenerate 4WM, with distant sidebands, the LO should be bichromatic, and each frequency component must match the mode shape and frequency of the corresponding component in the squeezed signal field. If the signal field is SSM, then both frequency components of the LO and signal field must be rigorously overlapped. If the signal field is a MSM squeezed field, then the two frequency components of the LO field must be overlapped in exactly the same way as the two frequency components of the signal field. That is to say they have to abide by the phase conjugation condition. In the case of all fields having flat wavefronts, as assumed by Lugiato and Grangier [133], this corresponds to a geometrical alignment between the frequency components. When flat wavefronts cannot be assumed, the phase conjugation condition is more complicated, and separately applies to all locations within the transverse spatial profile of the fields.

CHAPTER 4

OPTIMISATION AND CHARACTERISATION OF SQUEEZED LIGHT

4.1 Introduction

The main aim of the experiment is to generate and characterise a MSM squeezed state, suitable for quantum imaging with direct illumination. For a MSM squeezed state to be suitable for quantum imaging with direct illumination, the squeezed state must contain many localised regions that are independently squeezed, each of a size much smaller than the size of the whole of the squeezed state. With the 4WM gain medium under investigation in this thesis, this requires that the spatial separated modes of the far field TMSS must first be overlapped, using a beam splitter, to generate a squeezed state propagating along a single direction. The many components of the experiment are laid out as a block diagram in figure 4.1. They consist of a gain medium, acting as a near-field MSM SMSS source, propagation of this squeezed light to entangled fields, or TMSS, in the far field. Combining the entangled fields on a beam splitter, to recover a MSM SMSS. The generation of a BLO, imaging of the mode shape, and finally a homodyne detection stage to measure the squeezed field. Each of the blocks in the experiment contains a number of difficulties that the experimental design has to overcome. In this chapter, I describe the design of the experiment to meet these requirements, which were laid out in the previous chapter, and summarised in section 3.9. I will end the chapter by discussing the experiments completed to measure the phase rotation of the squeezed vacuum state, also referred to as the rotation of the noise ellipse phase (NEP), and the MSM nature of the generated squeezed field.

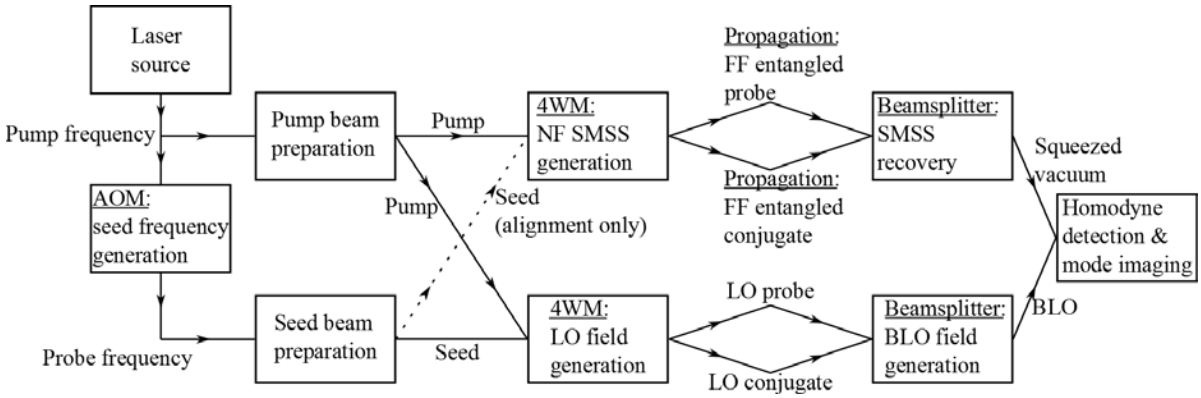

Figure 4.1: The block diagram of the experimental system used to generate and measure squeezing. In this diagram, NF references the near field, and FF references the far field. A single laser source is used, operating at the pump frequency. The majority of the field is used to generate two pump fields operating two separate 4WM gain processes, one to generate a squeezed vacuum field, and one to generate the BLO field. The remaining small portion of the main source field is separated off for the seed fields, and is frequency shifted using an AOM. This is re-sized and aligned into the 4WM medium used to generate the BLO. A portion of this field can also be directed into the 4WM medium used for squeezed state generation for alignment purposes. After the 4WM gain processes, the squeezed vacuum probe and conjugate field are overlapped, and separately the BLO components are overlapped. This process generates a squeezed state propagating in a single direction, and a suitable BLO to measure it, thus making the squeezed field suitable for using in direct illumination quantum imaging. The SMSS field is then measured in a homodyne detector using a BLO, and the investigated mode imaged.

4.2 Experimental setup, and techniques

The system was initially designed by Mat Turnbull, the previous PhD student on the experiment. Details of the original design, alignment procedure and initial experiments can be found in his thesis [98]. Since he has completed his studies, I have continued to work using the same base setup. I have made some improvements to the setup, and streamlined the alignment procedure, detailed in section 4.2.6, which has allowed me to progress the experimental work, and measure new results.

The full experimental setup is shown in figure 4.2, and fundamentally consists of the same parts as the block diagram in figure 4.1. It is designed to allow the full control necessary to generate and characterise a MSM squeezed field using a BLO. In the remainder of this section I shall proceed to describe the important aspects of the setup, and the alignment procedure.

All fields within the experimental setup are derived from a single continuous wave Titanium:Sapphire laser (M Squared SolsTis), which is pumped with a green pump laser (Coherent Verdi). The Ti:Sapph laser is tunable across a wide frequency range. The software provides two separate locks to keep the laser stable and at the desired frequency. The laser control is shown in figure 4.3. An etalon in the laser cavity can be tuned and then locked to provide coarse wavelength adjustment. This is used to tune the laser to the correct

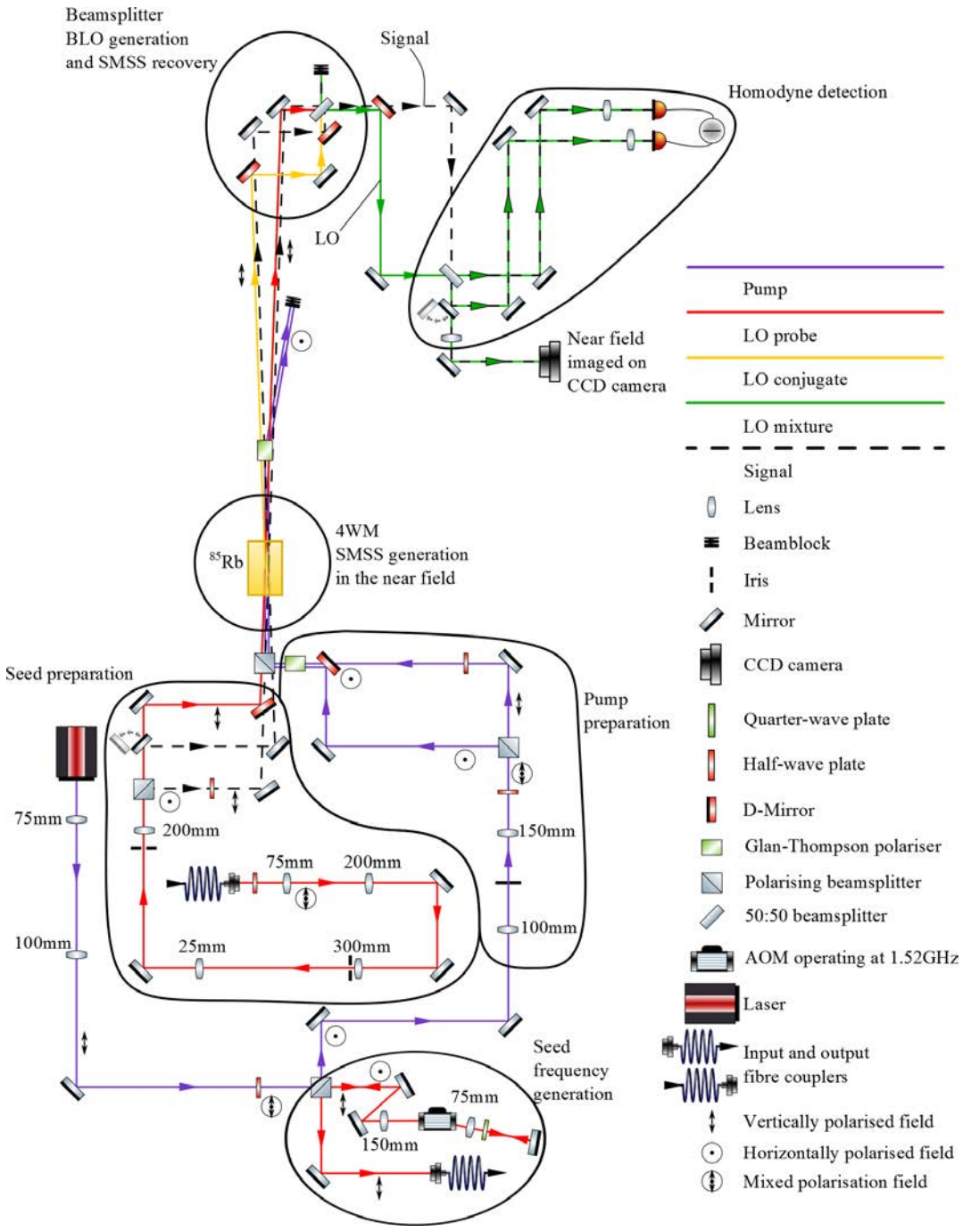

Figure 4.2: A full experimental diagram of the setup. The black dashed lines depict the vacuum fields, which at all points contain both the probe and conjugate frequencies. The solid lines depict bright fields. The red and yellow represent probe and conjugate LO frequencies respectively. The green represents the BLO, and the purple the pump field. The magenta lines show the mask object and images positions. Where the vacuum and LO fields are slightly offset in the diagram they are actually separated vertically in the experiment. Nonetheless we use a single beam splitter for both of them in the overlapping stage.

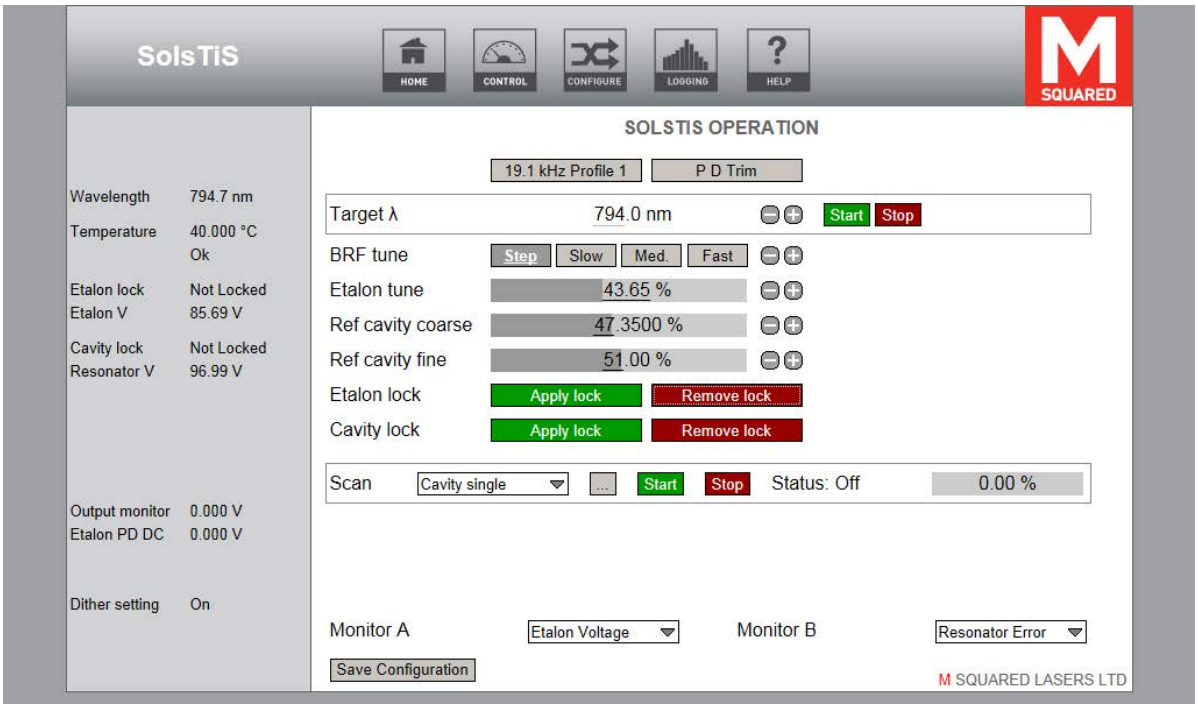

Figure 4.3: The computer software user interface used to control the laser frequency and locking. Note that the wavelength readout has a significant offset compared to that read with a separate wavelength meter.

frequency as read on a separate wavelength meter (Advantest TQ8325). The laser frequency can be locked to a reference cavity, and the cavity length tuned to provide further fine adjustment of the laser frequency. This control is used to scan through the 4WM gain feature and is left locked close to the frequency that provides the highest 4WM gain.

4.2.1 Gain medium

The gain medium used to generate the localised squeezing, in the near field, is a hot rubidium 85 vapour. The rubidium is contained within a vapour cell (Triad Technology, purity >98%), which is heated to approximately 110°C to achieve the correct vapour pressure, and hence good 4WM gain. The 4WM gain is very sensitive to atomic density fluctuations. The temperature of the vapour cell is kept constant using a peltier controlled by a temperature controller system (Thorlabs, TED200C) as a feedback loop from a thermistor. Full details can be found in Mat's thesis [98]. The thermistor can be read to find an approximate vapour temperature.

In general temperature gradients in air give rise to convection currents. Such air currents can cause phase fluctuations, and beam deflections, within the squeezed field, and as such reduce any squeezing. In order to remove these air currents the vapour cell and heating system are contained within a vacuum chamber. The

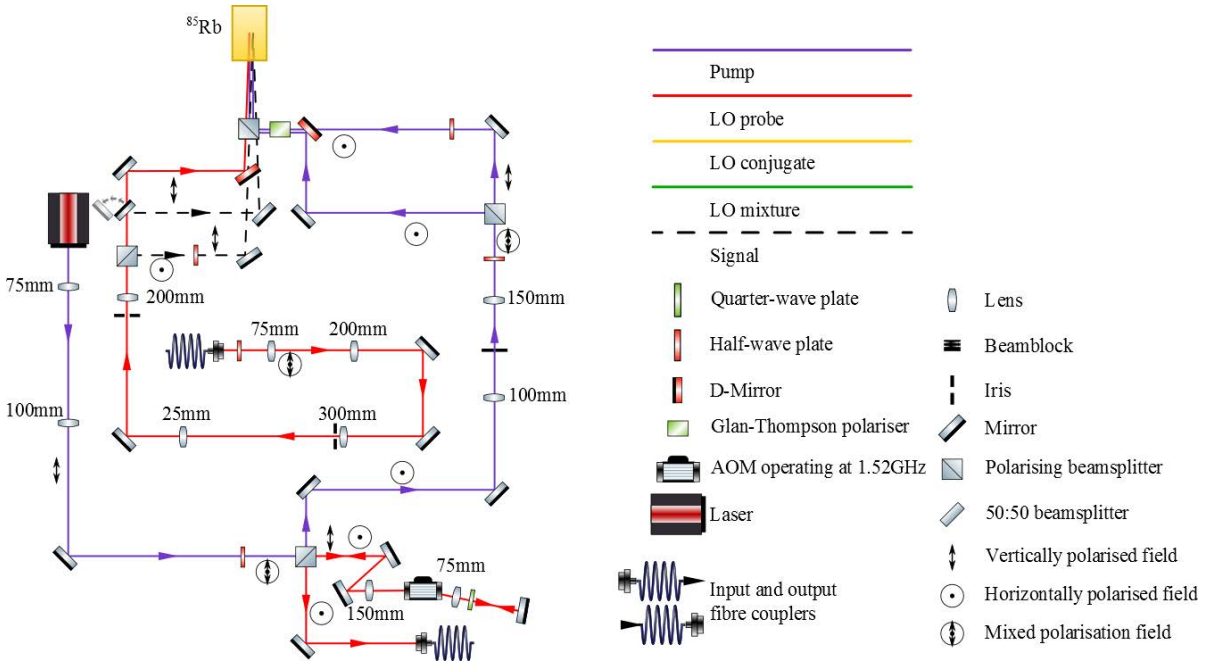

Figure 4.4: The preparation of all the pump and seed fields, at the probe frequency, before the 4WM cell. Where, on the diagram, the signal and LO fields are slightly separated, they are split vertically in the experiment.

vacuum chamber does not need to be under high vacuum, as such the chamber is not constantly pumped whilst in use. Instead the chamber is evacuated once every few months and then sealed with a valve.

4.2.2 Initial beam preparation

All fields are derived from the same source laser, operating at 794.975 nm, which ensures relative phase stability between the different fields. The preparation of all of the necessary fields is shown in figure 4.4. The main laser field is re-sized and collimated, with the majority of the laser power being used to generate the 4WM pump beams. At this stage a small portion is taken to be used to generate the seed field at the probe frequency. The seed is generated using an acousto-optic modulator (AOM) operated in a double-pass arrangement.

The majority of the laser field, after a small portion has been extracted for the seed field, is passed through a second telescope ($f_1 = 100$ mm, $f_2 = 150$ nm), passing through a pin hole (150 μm), at the focus, to clean the mode shape. This field is then split in half to generate the two pump fields, one used for the generation of the signal, and the other for the generation of the BLO. Both pumps have a waist size ($1/e^2$ radius) of approximately 1 mm in the centre of the 4WM cell. This waist size, along with the length of the rubidium

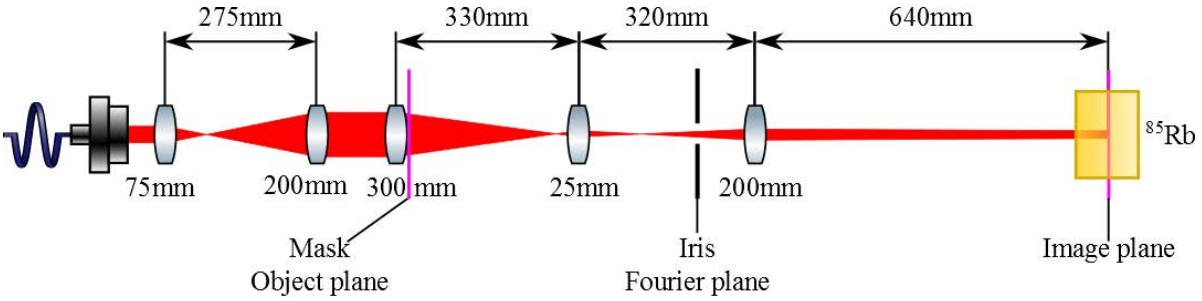

Figure 4.5: The lens system re-sizing the seed field between the fibre and 4WM cell. The field is first expanded to allow for easy use of a detailed mask. The mask is subsequently imaged in the centre of the 4WM cell at a smaller size.

vapour cell (12.5 mm) provide the dimensions for the 4WM gain region in the experiment.

The pump and probe fields have a large frequency separation of approximately 3 GHz. This leads to a required AOM frequency of approximately 1.5 GHz in a double pass arrangement to shift the field to the probe frequency. The AOM (Brimrose TEF-1520-100-795) is driven with a radio frequency (RF) taken from signal generator (HP 8642M) and amplified up to 1 W (see Mat's thesis [98] for details). The RF generator is used to set the two-photon detuning, and is normally set to a frequency of 1.52 GHz, corresponding to a two-photon detuning of $\delta = 4$ MHz. The two-photon detuning is calculated by comparing the frequency detuning between the pump and seed field to that between the two ground levels of the double lambda system.

The high operational frequency of the AOM leads to both a large asymmetry in the shape of the shifted field, and a low conversion efficiency. Additionally the AOM setup is very sensitive to alignment and is relatively unstable. To remove the asymmetry in the field, and to decouple the 4WM alignment from the AOM alignment, the shifted probe field is passed through a single-mode fibre (Thorlabs, polarisation maintaining single mode, P3-780PM-FC-2). There is a limit to the power that the AOM can support of $\leq$ 40 mW, which coupled with a single pass AOM efficiency of approximately 10% and a fibre coupling efficiency of approximately 40%, leads to a maximum seed power of approximately 150 μW. The fibre defines the seed mode into the 4WM process, both propagation direction, by alignment, and size by the slection of fibre coupler (Thorlabs, 75 mm waist, F240FC-780). This means that different frequencies can be coupled into the fibre and the same seed alignment retained.

After the fibre, the seed field is overlapped with the pump field in the 4WM cell. In order to accurately control the mode shape of a bright field after the 4WM process, the mode shape of the seed must be controlled. This is achieved with a mask placed in the input beam and imaged into the cell. In order to control the sharpness of this image, high spatial frequencies can be removed in the Fourier plane with an iris. To make

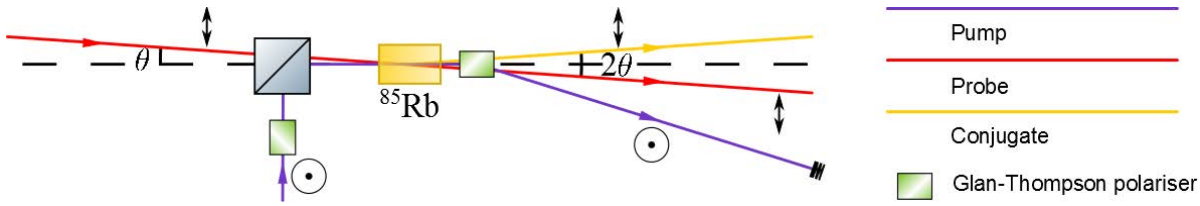

Figure 4.6: The seeding process. The seed field is mixed with the pump field on a large polarising beam splitter, at a small angle θ. The pump field is deflected and removed after the 4WM process by polarisation filtering using a Glan-Thompson polariser.

the application of a mask easier, the seed field is first expanded to a diameter of 5 mm.

In order for the seed field to be uniformly amplified by the 4WM system, it is important that the size of the seed field in the cell is small compared to the pump size. This is due to the Gaussian beam profile of the pump. Thus, after the masking point, the seed field is shrunk and imaged in the centre of the 4WM cell at a waist size ($1/e^2$ radius) of 0.4 mm. The unfolded imaging system is shown in figure 4.5. The field is split after the last lens in the imaging system. All optical path lengths to the rubidium cell are kept equal, to ensure that the object plane is imaged into the cell for all paths. One seed field remains permanently aligned as the seed signal (this field is blocked for squeezed vacuum generation) The second field can be directed either into the signal 4WM process, to aid with alignment, or to be the seed for the BLO generation.

4.2.3 Two mode squeezed state generation and local oscillator generation

The 4WM process requires that the pump and the twin beams are all linearly polarised, with the twin beams perpendicularly polarised to the pump beam. In our case the pump is vertically polarised and the twin beams are horizontally polarised. The pump and seed fields are combined using a beam splitter before the 4WM cell. The seed fields are used to produce bright twin beams, a BLO, or to introduce seed fields for alignment purposes.

The pump power (approximately 1 W) is much larger than the BLO seed (limited to approximately 150 μW), thus the pump field, and any scattered light from the field, need to be diverted before any measurements of the squeezed field can be made. This is achieved using a Glan-Thompson polariser (extinction ratio 10^{-5}) after the 4WM process which deflects the pump beam, allowing it to be easily dumped into a beam block (figure 4.6). The pump fields are also passed through a Glan-Thompson polariser before combing them with the seed fields, to maximise the pump polarisation purity. This is important to ensure the efficient extraction of the pump after the cell. In the rest of the thesis the Glan-Thompson polarisers will be represented as beam splitters to aid with clarity.

The 4WM phase matching condition (as discussed in section 3.6) means that the probe and conjugate fields propagate at a small angle $\theta \approx 5$ mrad to the pump field. This angle allows any remaining light, which is not diverted by the polariser, to be physically blocked.

When the 4WM process is seeded, a pair of bright twin entangled fields are generated. These fields show intensity correlations; that is the noise on the difference in their intensities is lower than the SN of a coherent field of their combined intensity. In our experiment measurements of up to -6 dB of intensity difference squeezing have previously been measured [98]. In a similar experiment intensity difference squeezing has been measured at up to -9.2 dB [83]. The seeded gain process can alternatively be used to generate the two frequency components necessary to form the BLO.

4.2.4 Overlapping of the restricted gain regions

In section 2.6.3 I discussed how a gain process can produce a SMSS in the near field, and how on propagation that SMSS can transform into a TMSS in the far field. I also discussed how the two modes of the TMSS do not have to propagate along the same direction, but instead can propagate separated by a small angle, as in the case in the 4WM process investigated in this thesis. In section 2.6.4 I discussed how a SMSS can be recovered from this TMSS in the far field, with the process shown in figure 2.9(b). In this section, I will discuss some of the alignment requirements for recovering the SMSS, through the process in figure 2.9(b). Here I explain the requirements by taking the view that the 4WM is an entanglement source, producing a TMSS in the far field, and that the recombination of this TMSS on a beam splitter gives a SMSS. In order to simplify the discussion, I will consider only 2 pairs of twin modes.

The main requirements in this section all arise from the symmetry of the 4WM process. The theoretical description of the TMSS amplifier in section 2.4 defines the two modes of the TMSS associated with $\hat{b}_1$ and $\hat{b}_2$. In this section the operators are re-labelled as $\hat{b}_1 \rightarrow \hat{b}_p$ and $\hat{b}_2 \rightarrow \hat{b}_c$ for the probe and conjugate frequencies of the 4WM system. In the theoretical picture, one pair of correlated modes is considered. In this description the mode associated with $\hat{b}_1$ (or $\hat{b}_p$) is defined to travel along the upper path, and that associated with $\hat{b}_2$ (or $\hat{b}_c$) to travel along the lower path. In this section these paths are denoted "Left" and "Right", and the operators written $\hat{b}_{pL}$ and $\hat{b}_{cR}$, to include the path information (figure 4.7). The description in the theoretical sections (section 2.4 and section 2.6.3) corresponds to a breaking of symmetry, since each of the frequency modes, associated with $\hat{b}_{p,c}$, is only considered to be produced in one direction. In the real system there is no break in the symmetry of the 4WM process.

Experimentally a TMSS amplifier such as that in section 2.4 generates two pairs of correlated modes, a

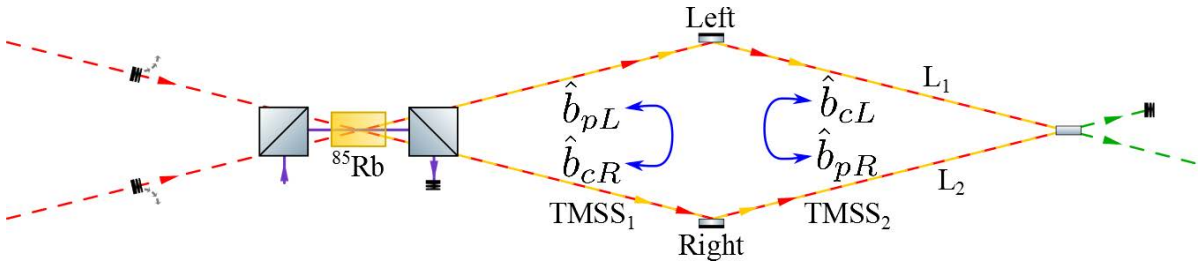

Figure 4.7: The interferometer used to overlap the signal fields. Seed beams are used for alignment of the squeezed vacuum as shown. Once the system is aligned, the seed fields are blocked to obtain the squeezed vacuum. The vacuum fields will form two separate TMSSs, one with probe in the left arm, of length L_1, and conjugate in the right, of length L_2, and a second with probe in the right arm and conjugate in the left.

total of four modes, with associated operators $\hat{b}_{pL}$, $\hat{b}_{cR}$, $\hat{b}_{pR}$ and $\hat{b}_{cL}$. These four modes can be considered as two pairs of correlated modes, with each pair forming an independent TMSS. The first TMSS, TMSS$_1$, has the probe sideband propagating in the "left" path, with associated operator $\hat{b}_{pL}$, and the conjugate sideband propagating in the "right" path, with associated operator $\hat{b}_{cR}$. The second TMSS, TMSS$_2$, has the conjugate sideband propagating in the "left" path, with associated operator $\hat{b}_{cL}$, and the probe sideband propagating in the "right" path, with associated operator $\hat{b}_{pR}$. Thus, the probe propagates in both the left and right restricted gain regions (RGRs) ($\hat{b}_{pL,R}$) and the conjugate propagates in both right and left RGRs ($\hat{b}_{cR,L}$) (figure 4.7). The output of the 4WM system is also a TMSS, TMSS$_{4\mathrm{WM}}$, which is a superposition of the two independent squeezed states, TMSS$_1$ and TMSS$_2$.

These two independent TMSSs can be interfered on a beam splitter and converted into two independent SMSSs, SMSS$_1$ and SMSS$_2$, following the same conversion as described in section 2.6.2. Thus the SMSS produced by the 4WM and recovered by interfering the "left" and "right" paths on a beamsplitter, SMSS$_{4\mathrm{WM}}$, can then be written as a superposition of these two independent squeezed states, SMSS$_1$ and SMSS$_2$. Each of the states SMSS$_1$ and SMSS$_2$ will, in general, have a different phase. Since the states are overlapped fully, and have the same polarisation and frequency components, they cannot be separated experimentally.

Consider a noise measurement preformed on the SMSSs, using homodyne detection and a MLO. If each SMSS were to be measured independently, the noise measured would be described by equation (3.34). However, since the states cannot be separated, the noise measured must be considered for the superimposed state, $\left\langle (\Delta \mathrm{SMSS}_{4WM})^2 \right\rangle$. The fluctuations corresponding to the superimposed state, $\left\langle (\Delta \mathrm{SMSS}_{4WM})^2 \right\rangle$, as

measured with a MLO, can be written as,

$$\begin{aligned}\left\langle \left(\Delta \mathrm{SMSS}_{4WM}\right)^2 \right\rangle &= 4\beta^2 \left(e^{2s}\cos^2\phi_1 + e^{-2s}\sin^2\phi_1\right) + 4\beta^2 \left(e^{2s}\cos^2\phi_2 + e^{-2s}\sin^2\phi_2\right) \\ &= 4\beta^2 \left[e^{2s}\left(\cos^2\phi_1 + \cos^2\phi_2\right) + e^{-2s}\left(\sin^2\phi_1 + \sin^2\phi_2\right)\right], \end{aligned} \tag{4.1}$$

where s is the squeezing parameter for each SMSS, $|\beta|$ is the amplitude of the MLO used to measure the SMSS fields, and $\phi_{1,2}$ are the relative phases of the squeezing ellipse for the two SMSSs, with respect to the LO phase. They replace ϕ_{LO} in equation (3.34).

The phases are made up of two contributions, $\phi = \phi_{4WM} + \phi_{\Delta L}$. The first, ϕ_{4WM}, is the phase arising from the 4WM amplification process, and solely depends on the pump and the chosen two-photon detuning. Thus ϕ_{4WM} is the same for TMSS_1 and TMSS_2. The second, $\phi_{\Delta L}$, arises from the path length difference $\Delta L = L_1 - L_2$ between the paths that the two modes of the TMSS travel before the beam splitter. As such the phases for the two SMSSs are

$$\phi_{\Delta L1} = \frac{2\pi}{c}\left(\omega_p L_1 - \omega_c L_2\right) \tag{4.2}$$

$$\phi_{\Delta L2} = \frac{2\pi}{c}\left(\omega_p L_2 - \omega_c L_1\right), \tag{4.3}$$

where $L_{1,2}$ are the path lengths of the two paths to the beam splitter, and $\omega_{p,c}$ are the frequencies of the probe and conjugate fields.

In order to maximise the measurable squeezing it is required that $\phi_1 = \phi_2$. This can only be achieved if $L_1 = L_2$. As such there is a requirement that there is no path length difference between the two paths to the beam splitter, $\Delta L = 0$. This process can be seen as rotating the two SMSS noise ellipses such that they are aligned, as shown in figure 4.8(b). Experimentally, this can be achieved using a bichromatic Mach Zehnder interferometer, where the 4WM process is treated as the first beam splitter. In this process the two symmetric RGRs are simultaneously stimulated each with a seed field at the probe frequency. This forms one interferometer at the probe frequency, and a second at the conjugate frequency. The visibility at the output of the bichromatic interferometer is maximised, which can only be achieved when the fringes of the probe and conjugate interferometers coincide. When this is achieved the interferometer is said to be a "white light" interferometer, and the fringes formed with light at any frequency will coincide. Typically a bichromatic fringe visibility of 99% can be achieved. This process minimises the path length difference between the two arms of the interferometer. Additionally optimum visibility is only achieved when the fields in the two arms

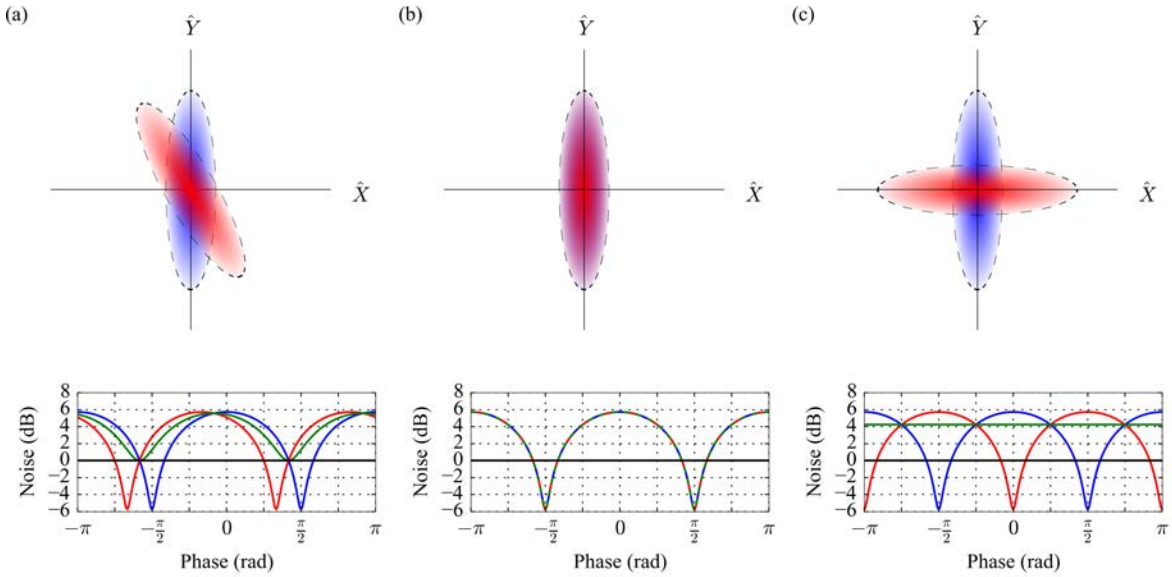

Figure 4.8: The effect of phase difference between the two SMSSs. The top row shows the orientation of the noise ellipses for each SMSS. The bottom row shows the noise of the two ellipses, in red and blue, along with the noise of the combined state in green, all plotted relative to the shotnoise of the LO used for homodyne detection. The graphs are the theoretical noise of a system with a 4WM gain of 4. (a) The phase delay is $\pi/6$, where the minimum noise of the combined state is at the QNL. (b) There is no phase difference between the two squeezed states. (c) The phase delay is $\pi/2$ and the combined state only shows noise significantly above the SN.

are optimally overlapped on the beam splitter. Thus this also serves as a method to ensure that the modes of the TMSSs are well overlapped on the beam splitter.

After the interferometer is aligned, the seed fields are blocked, such that each of the output ports of this beam splitter will be a squeezed vacuum state. The squeezed state from only one of the output ports of the beam splitter is investigated experimentally. This stage of the alignment proves to be the most critical for the generation and characterisation of a strong quadrature squeezed state.

4.2.5 Homodyne detection

The homodyne detection stage presents a further alignment challenge. In order to measure a good level of squeezing the probe and conjugate LO fields must be overlapped in exactly the same way as the signal RGRs. This forms the correct BLO to analyse the squeezed vacuum field that has been generated. When the squeezing is SSM, the BLO RGR must be geometrically overlapped with the signal RGR. When the squeezing is MSM, the BLO can be varied and moved across the signal RGR (see section 4.5). This can be achieved by using two separate interferometers. Firstly, one to overlap the probe LO on top of the probe in

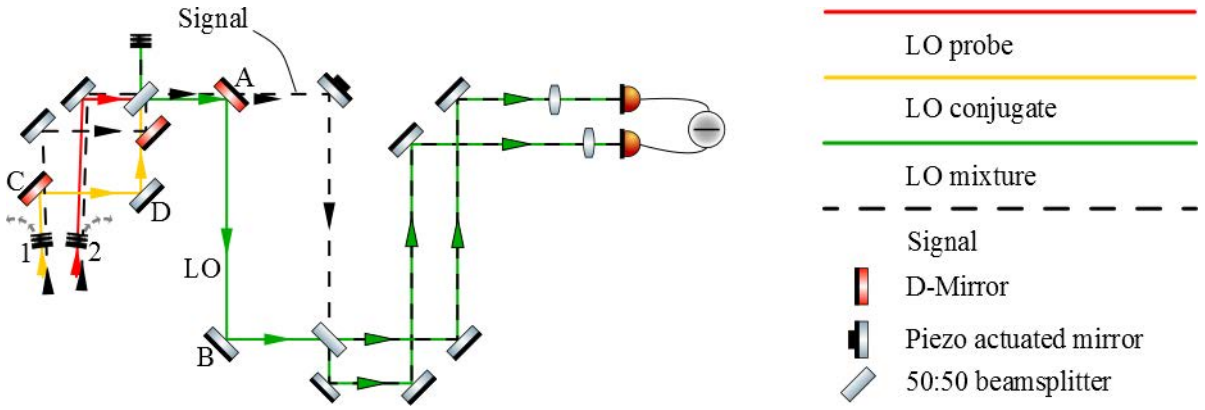

Figure 4.9: The homodyne detection stage. The LO is aligned to the signal field using visibility of interferometers independently for the probe (using mirrors A and B, and a beam block at position 1) and conjugate frequencies (using mirrors C and D, and a beam block at position 2). Where, on the diagram, the signal and LO fields are slightly separated, they are split vertically in the experiment.

the signal field, achieved using mirrors A and B, and the beam block in position 1 in the figure 4.9. Secondly, an interferometer to overlap the conjugate LO on top of the conjugate in the signal field, achieved using mirrors C and D, and the beam block in position 2 in the figure 4.9.

A spectrum analyser (HP 8560E) is used to measure the noise on the subtracted photocurrent from the homodyne detector. In section 2.2, I discussed the need to scan the relative phase between the LO and the signal field to achieve a complete measurement of the noise ellipse of the squeezed field. In practice this is achieved using a piezo-actuated mirror, driven by two stacked peizos. The piezos are driven with a triangular ramp with a period of 700 ms. More details on the setup of this can be found in Mat's thesis [98]. The spectrum analyser is set to a zero frequency span at 1 MHz, and a sweep rate of 0.9 s. The resolution bandwidth of the spectrum analyser is set to 100 kHz and the video bandwidth is 30 Hz. The spectrum analyser is set to trigger each scan from the waveform generator, such that the squeezing scan always appears at the same point on the screen.

The process of evaluating the SMSS starts with measuring the shot noise. This can be found by blocking the squeezed vacuum field input to the homodyne detector stage, at the point labelled "signal" in figure 4.9. Next the noise of the squeezed vacuum field should be measured, whilst the phase difference between the signal and LO is scanned. This ensures that the full squeezing ellipse is measured. The scanning can be achieved by changing the optical path length difference between the LO and signal field using a piezo actuated mirror, shown in figure 4.9. A typical experimental squeezing scan is shown in figure 4.10. This graph is a direct comparison to figure 3.10, where the same result is plotted theoretically.

The theoretical graph is plotted with the same 4WM gain, 4, as is measured in the experiment. However

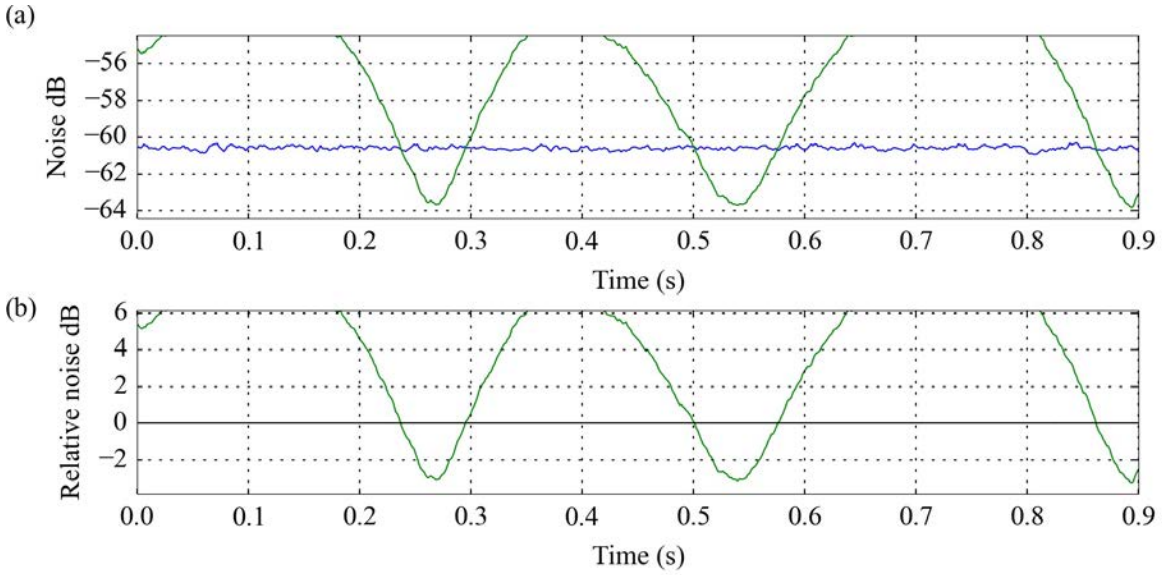

Figure 4.10: A typical squeezing scan. The phase of the signal is scanned, such that the noise of the different quadratures is measured. (a) shows the raw data, with the SN in blue, and the signal in green. (b) shows the relative noise between the squeezed field and a vacuum field.

in the experimental graph there are some factors, including imperfect alignment, that limit the minimum noise that can be measured. The skew in the shape of the experimental graph is partially due to the slight phase instability of the experiment, caused by vibrations on the table and air currents, and partially due to the nonlinear nature of the piezo scan. The level of squeezing can be extracted by subtracting the SN from the signal. In this case, it can be seen that squeezing of -3 dB has been achieved, corresponding to a noise reduction of a factor 2. This is the measure of QNR, as such this is the value extracted and plotted in all optimisations and squeezing experiments reported in this thesis.

This noise also incorporates all the technical and electronic noise from the detector and spectrum analyser. As such, the choice of detector is very important for measuring the best levels of squeezing. If the SN of the LO is equal to the electronic noise floor in the detection system then the minimum measurable noise is 3 dB below SN. As such, a direct measurement of a noiseless state would show only -3 dB of squeezing. Any measurement of a more realistic squeezed state will similarly show weaker squeezing than is present in the field. For example, if the 4WM process reduces the quantum noise of the field by 50%, or -3 dB, then the noise of this field will be half the level of the electronic noise floor. As such, the results, as displayed on the spectrum analyser, will show a total noise 1.8 dB above the noise floor. In other words, a real QNR of -3 dB will be reduced down to a measured -1.2 dB.

In order to arrive at an accurate measurement for the QNR, the noise of the squeezed field should remain

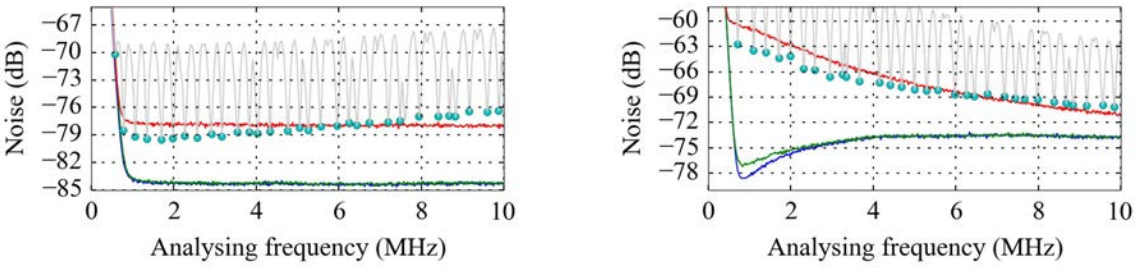

(a) Detector B.

(b) Detector C.

Figure 4.11: The background noise levels of the two detectors used in the experiment. Each detector is a detector with low electronic noise. a) Shows the data for detector B, which has lower gain, but a larger bandwidth. b) shows the data for detector C, which has higher gain, but a lower bandwidth. In each case the blue line is the noise floor, of the detector and spectrum analyser system, measured by blocking all light incident on the detector. The green line is the noise of the residual pump light that reaches the detector, measured by blocking the seed field. The red line is the SN, measured by blocking the squeezed signal field, and the grey line is the signal noise, measured as its phase is scanned. Its minima are plotted with blue circles. The noise peak close to DC is the technical noise.

at least an order of magnitude larger than the electronic noise floor, corresponding to 10 dB. Since intensity difference squeezing of up to 6 dB has been measured in this system, it is reasonable to require that the SN of the LO should be at least 16 dB above the technical noise floor. This requirement is best met by the use of a detector with both a high gain and a low technical and electronic noise.

The effect of a high noise floor can be seen in figure 4.11, where one detector, labelled B (figure 4.11(a)), measures less squeezing than a second detector, labelled C, with a higher gain (figure 4.11(b)). As can be seen from the graphs, changing from B to C sees the difference between SN and the noise floor rise from around 10 dB to around 17 dB, at 1 MHz. Thus, at this level of gain, subtracting the electronic noise floor should make only a minimal correction to the raw measured QNR. In view of this, detector C is used in the experiments with higher amplification at low intensities. The trade-off is that detector C has a smaller bandwidth. Additionally detector C also has a lower saturation intensity.

4.2.6 Experimental procedure improvements

The original alignment process involved starting each day with optimising the angle between the probe and pump (θ), for the optimum production of intensity difference squeezing. In order to move on to the next step, the system was required to produce at least -5 dB of intensity difference squeezing. This was originally achieved using removable magnetic mirror mounts, which have poor stability when taken in and out of the system.

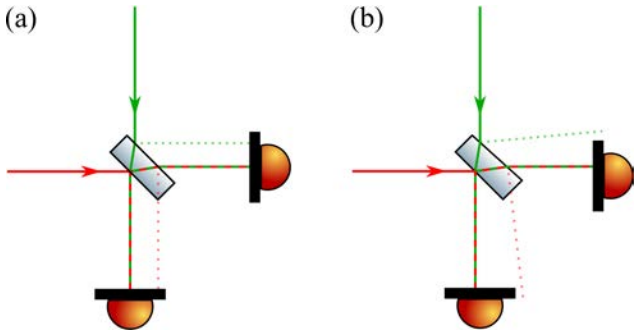

Figure 4.12: The creation of ghosting. For each input (red and green) a ghost is created (the light dashed lines) at the non-reflective side of the beam splitter. (a) shows an ordinary beam splitter, where the ghost image can reach the detectors. (b) shows where a wedged beam splitter is used, and the ghost propagates away from the main light field, and as such does not reach the detectors.

After taking over the setup from the previous PhD student, I made some small changes, exchanging some mirror mounts to improve the control over some beams, and the day to day experimental stability. I updated the system, such that the key mirrors defining the initial alignment were all static rather than removable. Whilst making these changes, I gained an improved understanding of the experimental system, and which stages of the alignment are critical to achieve strong squeezing.

From experimental observations, it transpired that the production of strong quadrature squeezing does not depend as strongly on the angle θ as intensity difference squeezing does. Thus optimising θ for maximum intensity difference squeezing, measured on the entangled fields, is not critical for achieving strong quadrature squeezing. The exact cause of this remains uncertain, however its observation led to the removal of this first tricky alignment stage. Instead the critical stage in the alignment comes primarily from the optimisation of the bichromatic interferometer. The critical first step to this alignment is that the seed fields in each RGR are propagating along coupled directions, ie. each probe is rigorously co-propagating with the other's conjugate. Additionally, it is critical that the two probe and conjugate fields are overlapped with each other and the centre of the pump field, in the centre of the vapour cell, the near field. This ensures that the probe and conjugate field have the maximal geometric overlap with each other and the pump field throughout the gain medium.

A further problem that needed resolving was the impact of the thickness of beam splitters. The beam splitters necessarily have two surfaces, one being the partially reflective surface, and the other nominally transmissive. In reality the transmissive surface produces a low power reflection, called ghosting (figure 4.12(a)). If this ghost is coupled into the detector, then its presence will reduce the measurable level of squeezing. Consequently removing such ghosting ensures better measurements. In order to achieve this, I have introduced

wedged beam splitters to ensure that any ghosting propagates away from the main beam path (figure 4.12(b)). This ensures that the ghost image does not reach the detectors, and hence improves results.

With these improvements, I have been able to progress the experiment from the state of measuring usable squeezing on an occasional basis to measuring a reasonable level of squeezing on a daily basis, at approximately -3 dB. This progression has allowed me to develop experiments to measure the effects of the NEP rotation using the BLO, and to directly measure the MSM nature of the squeezed light generated in the experiment. A discussion of these experiments and the results obtained will follow in sections 4.4 and 4.5.

4.3 Optimisation and calibration

There are a number of factors, beyond the alignment, that will affect the 4WM gain, and hence the level of squeezing it can generate. These include the frequency of the main pump beam, called one-photon detuning, Δ, the detuning between the pump and the probe frequency, called two-photon detuning, δ, and the rubidium temperature. Although previous work has been done investigating these parameters for optimum 4WM gain [124], and for optimum amplitude correlation measurements [98], it is still important to perform some measurements to ensure that the optimum parameters for SMSS squeezing remain the same as those for gain and TMSS generation. To achieve this optimisation, as each parameter is scanned, a graph such as that shown in figure 4.10 is taken for each value of the parameter, and the squeezing is extracted as the lowest relative noise level. This corresponds to the normalised size of the minor axis of the squeezing ellipse. The value of the parameter can then be chosen to be that which generates the optimum squeezing.

4.3.1 One-photon detuning

The one-photon detuning, Δ, is a measure of the main laser frequency, as a detuning from the rubidium 85 D1 line $5S_{1/2}, F = 2 \rightarrow 5P_{1/2}$ transition (figure 3.2). The laser frequency is scanned using the computer control of the Ti:Sapph laser. The peak gain occurs at a detuning of approximately 800 MHz from the rubidium-85 D1 line $5^2S_{1/2}\,(F = 2) \rightarrow 5^2P_{1/2}$ transition. Previous calibrations both with the use of a saturation spectroscopy setup, and the use of a wavelength meter, have shown that a change in tuning of 1% of the full cavity tuning range corresponds to a change in frequency of 1.5 ± 0.3 GHz. There is no absolute calibration for the laser frequency presently available. This is because each time the laser is locked the system locks to the nearest cavity peak, irrespective of the previous lock point.

As the laser frequency is scanned through the 4WM gain region, the gain, and hence the squeezing,

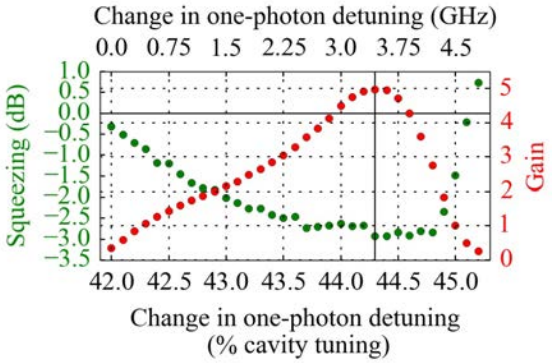

(a) One-photon detuning. The rubidium vapour cell temperature is held at 112°C, and the two-photon detuning is set as $\delta = 4$ MHz. The peak gain and squeezing correspond to a detuning of approximately 800 MHz from the rubidium-85 D1 line $5^2S_{1/2}\,(F = 2) \rightarrow 5^2P_{1/2}$ transition.

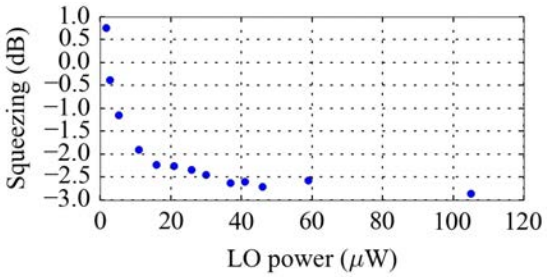

(b) LO power. The rubidium vapour cell temperature is held at 112°C, and the two-photon detuning is set as $\delta = 4$ MHz.

Figure 4.13: The change of squeezing with experimental parameters. (a) The 4WM gain, measured as a ratio of output probe intensity to seed intensity (red) and squeezing (green) as a function of laser frequency (or one-photon detuning Δ). The horizontal axis is labelled both as the cavity detuning accessible from the laser control system, and as the change of frequency, inferred through previous calibrations. The vertical line passes through the highest gain and the strongest recorded squeezing. (b) The squeezing is plotted as the LO power is changed. Whilst the LO power does not directly affect the squeezing level, lower LO power means that the results are affected more by the noise floor of the detector.

changes. Initially, as Δ is decreased the gain increases due to approaching the 4WM resonance, and hence more probable 4WM. When Δ is reduced further, such that the probe frequency becomes too close to the atomic resonance, absorption of the probe starts to dominate, which both reduces gain and, to an even greater extent, squeezing. The resultant effect on the 4WM gain, measured by comparing the input and output powers of the probe field, and squeezing levels are displayed in figure 4.13(a). The scale in figure 4.13(a) has an arbitrary offset, due to the lack of absolute calibration.

Since the laser is turned off overnight, the one-photon detuning needs to be reset daily. A wavelength meter is used for coarse adjustment of the laser frequency, until the wavelength is within the 4WM gain region, and the fine tuning is adjusted such that the largest 4WM gain is achieved. Figure 4.13(a) demonstrates that tuning to the largest 4WM gain also tunes to the highest levels of squeezing. Thus tuning for optimum 4MW gain is a viable method to ensure that the laser frequency is at the best position for optimum squeezing.

4.3.2 Local Oscillator power

In theory the level of squeezing measurable should not be affected by the LO power used. However, in practice, as discussed in section 4.2.5, the minimum noise that can be measured is limited by the ratio of

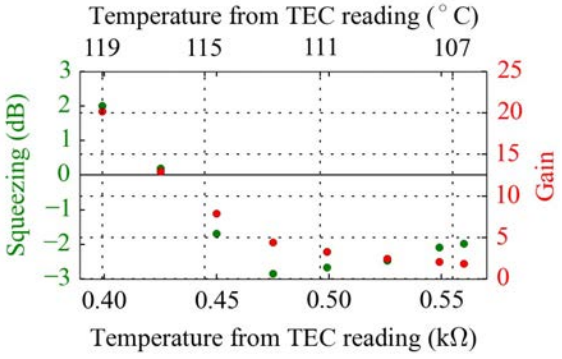

(a) ^{85}Rb vapour temperature. The two-photon detuning is set as $\delta = 4$ MHz.

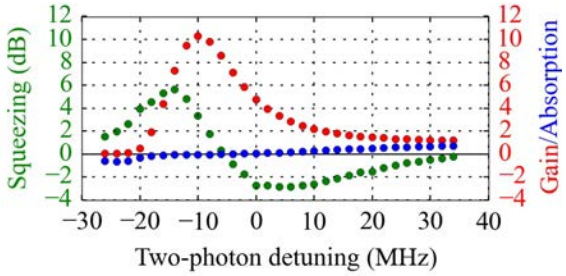

(b) Two-photon detuning. The rubidium vapour cell temperature is held at 112°C.

Figure 4.14: The change of squeezing with experimental parameters. (a) The squeezing level (green) and 4WM gain (red) are plotted as the temperature of the 4WM cell is changed. The temperature is reported both as the TEC readout, and the corresponding temperature from the thermistor data sheet. (b) The graph shows how the two-photon detuning affects the measured squeezing. The red data shows the gain, the green data shows the squeezing, and the blue data shows the fractional difference between probe and conjugate powers in the LO.

the SN of the LO to the electronic noise floor. It is important to check that the LO power is high enough such that the electronic noise floor does not limit the measured QNR. In order to check this, the LO power is scanned, by adjusting the seed power using a waveplate and polarising beam splitter. The squeezing level is measured for each power, and plotted in figure 4.13(b). The graph shows the power of the seed at the input to the 4WM cell. With the usual gain of 4 this corresponds to a quarter of the final BLO power. The measurable noise clearly saturates at approximately -3 dB for large LO powers, and remains near this level for LO powers down to a seed power of roughly 50 μW, corresponding to approximately half the maximum seed power. This demonstrates that the squeezing measurements with a strong LO are not limited by the LO power.

4.3.3 Temperature

The effect of changing temperature, and hence rubidium vapour pressure, is shown in figure 4.14(a), where the temperature is measured by the thermistor used for the temperature control loop. This thermistor is placed near what should be the coldest point on the vapour cell, and thus gives an approximate vapour temperature for the rubidium. However, it should be noted that this measure is not accurate due to the inexact location of the thermistor.

As the temperature is increased the vapour pressure of rubidium is increased, which leads to more rubidium atoms being present in the gain region. This leads to a higher gain, and as such one would expect more

squeezing. However, increasing the temperature also increases the number of collisions occurring within the atomic vapour. These collisions are responsible for inducing a decoherence in the atomic medium which makes the absorption increase faster than the gain. This effect is mainly seen on the probe, due to its frequency being much closer to the atomic resonance compared to that of the conjugate. As such, one part of the correlated twin beam side-bands is absorbed, leading to reduced correlations, and eventually to an overall increase in quantum noise, when the absorption is high enough.

4.3.4 Two-photon detuning

The two-photon detuning, δ, set by the frequency of the seed field, demonstrates a similar effect to that of the temperature. The increased gain from being closer to the atomic resonance competes with the associated increased absorption. The effects of changing the two-photon detuning are shown in figure 4.14(b). In the most simplistic view, one would expect a gain profile to be roughly Gaussian, with the gain dropping off to either side of some ideal value, defined by the atomic transition frequency and line-width. In reality, the medium becomes opaque as the two-photon detuning is reduced, as can be seen by the gain reducing to zero (red circles in figure 4.14(b)). However, this thesis is concerned with the level of squeezing that can be measured (green circles in figure 4.14(b)). The level of squeezing is effected by the competition between the processes of gain and loss within the atomic medium. As the two-photon detuning is reduced, the loss increases faster than the gain, reducing the squeezing [124]. Indeed, at small δ, absorption leads to increased noise rather than reduced noise. The blue data in figure 4.14(b) shows the fractional difference between the probe and conjugate powers, within the LO, taken as $(I_p - I_c)/(I_p + I_c)$. When the probe power is equal to the conjugate power, $I_p = I_c$, the 4WM system absorbs as much probe power as is present in the initial seed beam. As such this point represents strong absorption, and results in a loss of squeezing near this point.

4.3.5 Parameter inter-dependence

All of these parameters contribute to the efficiency of the 4WM process, and they all effect the squeezing level that can be measured. These parameters also interact, such that the optimum tuning of one parameter may depend on a second parameter. One such example is the dependence of the squeezing level on the combination of two-photon detuning and the temperature of the rubidium vapour. Figure 4.15 shows how the squeezing changes with two-photon detuning at a variety of rubidium temperatures. Indeed, it can be seen that the optimum two-photon detuning for QNR changes with the temperature. This is because the temperature sets the vapour pressure and hence the 4WM gain, whilst at the same time changing the rate

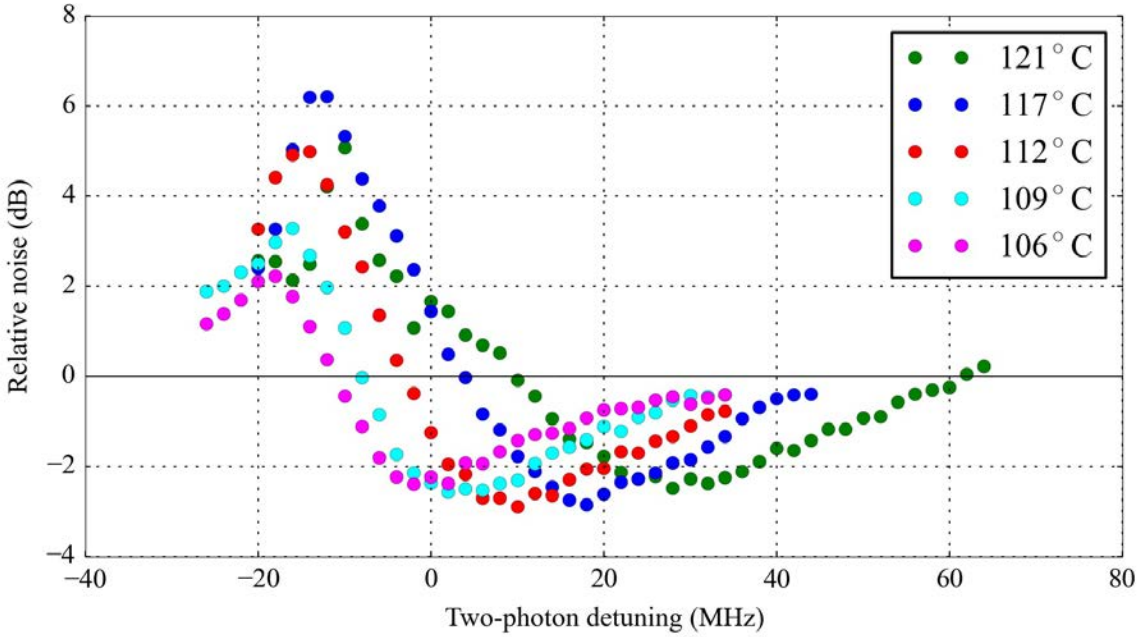

Figure 4.15: The graph shows how the squeezing level changes with two-photon detuning and temperature. Each colour shows the data taken at a different temperature. The temperatures are converted from the resistance read across the thermistor.

at which light is absorbed. The competition between these two factors leads to a change in the optimum two-photon detuning for generating squeezed light as the temperature is changed.

4.3.6 Optimal squeezing and losses

Using the optimum parameters, found through the scans in this section, I have managed to achieve a maximum squeezing level of -3.7 dB, as seen in Figure 4.16. When corrected for the remaining noise floor this reveals an underlying level of squeezing of -3.8 dB. These results are taken with the LO and signal pumps balanced at about 900 mW, the AOM operating at 1.52 GHz, corresponding to a two photon detuning of $\delta = 4$ MHz. The LO seed power is set to greater than 100 μW, after a gain 4 in the 4WM process and splitting this corresponds to 350 μW. The rubidium vapour cell temperature is held at 112°C.

In these results, the excess noise on the anti-squeezed quadrature is close to 10 dB. For a pure Gaussian state, the level of QNR should be at this same level, since such a state is a minimum uncertainty state. However, the losses and imperfections throughout the experiment prevent this from being the case. The combined loss, through imperfect mirrors (13 with a reflection of 99.8 %), beam splitters (2 with an absorption of 0.2 %), vapour and vacuum chamber windows (2 with a transmission of 98 %), and the imperfect photodectors (2 with a quantum efficiency of 95 %) is close to 20 %. The effect of these losses on the measur-

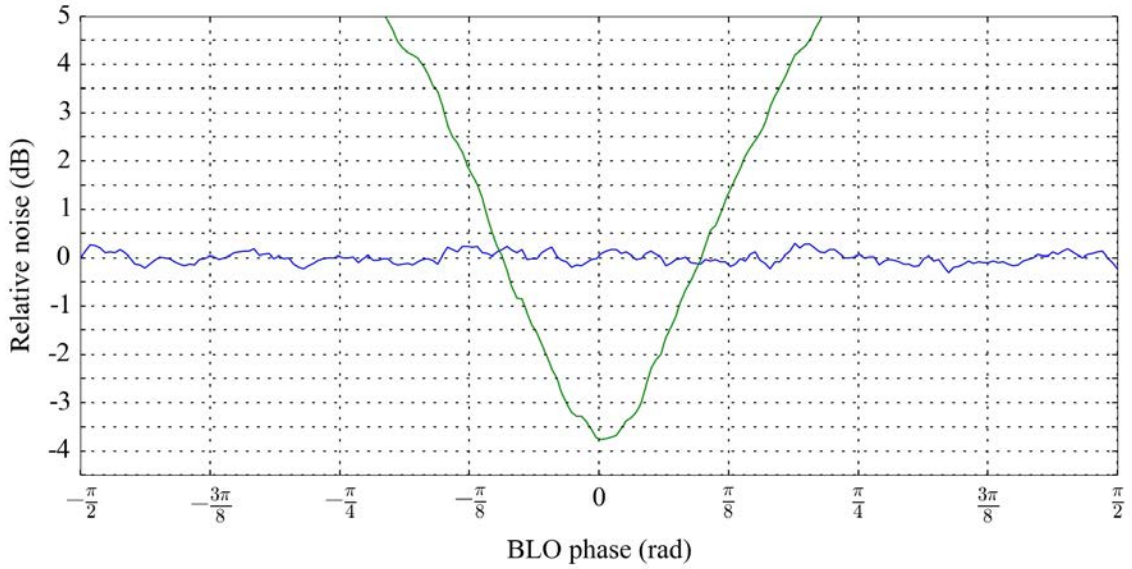

Figure 4.16: A typical squeezing graph, generated by scanning the phase difference between BLO and signal fields. For this data the LO pump power is 900 mW, the signal pump power is 950 mW and the gain is around 4. The electronic noise floor can also be subtracted, revealing a squeezing level of -3.8 dB.

able squeezing level can be modelled using ideal beam splitters (section 3.7). Specifically, equation (3.24) can be used, with $\left\langle \Delta\hat{i}_p^2 \right\rangle$ being the noise of the input state, and $\left\langle \hat{i}_p \right\rangle$ being the extra noise introduced from the background vacuum field. Using this model it can be seen that losses at this level would reduce the squeezing from -10 dB to -6.3 dB.

Imperfect mode matching of entangled modes on the beam splitter is a more tricky issue. Typically a visibility of 99 % can be reached, corresponding to a 1 % mismatch. However, the extra 1 % of light will have excess noise, $\left\langle \hat{i}_p \right\rangle$, at 10 dB above the QNL. Again, using the beam splitter model, this 1 % mismatch can be calculated to correspond to a loss of squeezing from -10 dB to -7 dB.

Finally, there is an error through the overlap of the LO to the squeezed field. Once again this mismatch is close to 1 % and mixes in light with an excess noise 10 dB above SN. Correspondingly, this results in a loss of squeezing from -7 dB to -5.3 dB.

In total, including the losses and imperfect alignments in correct order, these losses add up to a total drop from -10 dB of squeezing at the point of generation to -3.6 dB at the point of measurement. Thus, within the system, the maximum level of squeezing that could be expected with the present parameters would be -3.6 dB. On top of this, there is an additional loss from the imbalance of powers in the LO, as explained at the end of section 3.8. The inclusion of this loss results in a final expected squeezing measurement of -3.5 dB. As such, the level of squeezing measured (figure 4.16) is consistent with the expected best measurement. The

biggest single effect in the reduction of the measurable level of QNR is the slight mismatch of entangled modes. As such, to generate stronger squeezing the mode matching must be improved.

4.4 Rotation of the noise ellipse

4.4.1 Introduction

In section 2.7.1, I discussed the use of squeezed light in an interferometer and the limitations to the accuracy of the interferometer from both phase and amplitude noise. I explained the nature of the squeezed field required to make measurements below the QNL over a large range of frequencies, and how at low frequencies amplitude squeezing is required, whilst at high frequencies phase squeezing is required. In this section, I investigate the properties of the squeezed vacuum field that I have generated using a 4WM process, with a particular view to its use in such an interferometer. This experiment serves as a proof-of-principle of the generation of a squeezed field with similar quadrature properties as those required for improved gravitational waves detection [9].

In this section, I treat the squeezed field as a single spatial mode and investigate how the noise ellipse phase (NEP) rotates as the two-photon detuning is changed. I use the BLO field to investigate this rotation of the NEP. First, I verify that the BLO phase tracks the NEP in the present experiment. Then I investigate the phases of the BLO frequency components as evidence for the NEP. Finally, I discuss the relevance of the results to improving the sensitivity of interferometers.

4.4.2 Invariance of relative phase between local oscillator and squeezed vacuum

The phases of the correlations in the vacuum twin fields, used to generate the squeezed field, are only dependent on the two-photon detuning and the phase of the pump field. When the twin beams are mixed on the beam splitter, to produce a SMSS, and that SMSS is measured using a beam splitter, the result is a noise ellipse, defined by equation (3.47). The NEP, $(\phi_1 + \phi_2)/2$, is the average of the phase of the probe, ϕ_2, and conjugate, ϕ_1. The phase of both components changes as the two-photon detuning is changed. The two-photon detuning, δ, is chosen by the frequency of the LO used in the homodyne detector and the analysing frequency, Δ_a, of the spectrum analyser.

Consider a measurement made with a MLO, formed by an independent laser field, at the central pump frequency. Here, the noise is measured as a sum of the two sidebands separated from the MLO field by the analysing frequency, Δ_a (section 3.7.4). The choice of Δ_a, set on the spectrum analyser, determines the

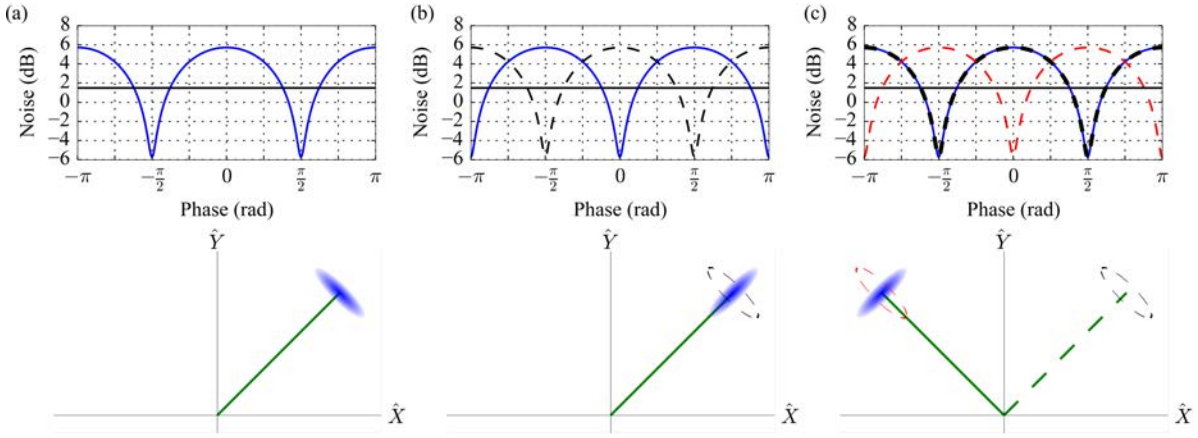

Figure 4.17: The quadrature diagrams where a squeezed state (blue) is mixed with a LO (green). The top panel shows the measured noise of the squeezed state as the phase is changed. as defined by equation (3.47). The bottom panel shows this same noise as represented by an ellipse on a quadrature diagram. (a) shows the measurement made at a two-photon detuning δ_1. (b) and (c) show the case when the two-photon detuning is changed to δ_2. The black line shows the state at δ_1 for comparison. In (b) the LO is derived from an independent laser, so changing δ does not change the LO phase. In (c) the LO is a BLO generated through 4WM such that changing δ changes the BLO phase. In (a) both LO sources produce the same results. In (c) the red dotted line shows the state as it would be measured by a MLO at δ_2, as shown in (b). In each case the ellipse outline colours in the bottom panel relate to the colours in the top panel.

two-photon detuning of the measured bands. Since changing the two-photon detuning changes the NEP, one might expect that such a change would result in a relative phase shift. Indeed, such a relative phase change, between the LO and the squeezed vacuum field, does occur and results in a translation of the squeezing spectrum along the horizontal axis as represented in figure 4.17(b).

However, in the present experiment a BLO is used, which is also generated using 4WM. In this case, two sidebands are measured for each frequency component of the BLO (section 3.8). Here, the analysing frequency, Δ_a, sets the separation of these sidebands from the BLO components. The analysing frequency is chosen to be small, such that the two bands can be treated as both being at the same two-photon detuning. The two-photon detuning is, in turn, determined by the frequencies of the BLO components, defined by the frequency of the seed used to generate the BLO. When the BLO seed frequency is changed, the phase of the BLO will rotate, due to the 4WM process. This will happen at the same rate as the NEP of the squeezed vacuum field rotates. Thus, the relative phase between the BLO and squeezed vacuum will remain constant as the two-photon detuning is changed (figure 4.17(c)). Since it is only the relative phase between the BLO and SMSS components that appear in the homodyne detection signal (equation (3.48)) there should be no translation of the squeezing spectrum as measured with the spectrum analyser.

In order to verify this experimentally, the squeezing needs to be measured at different two-photon detun-

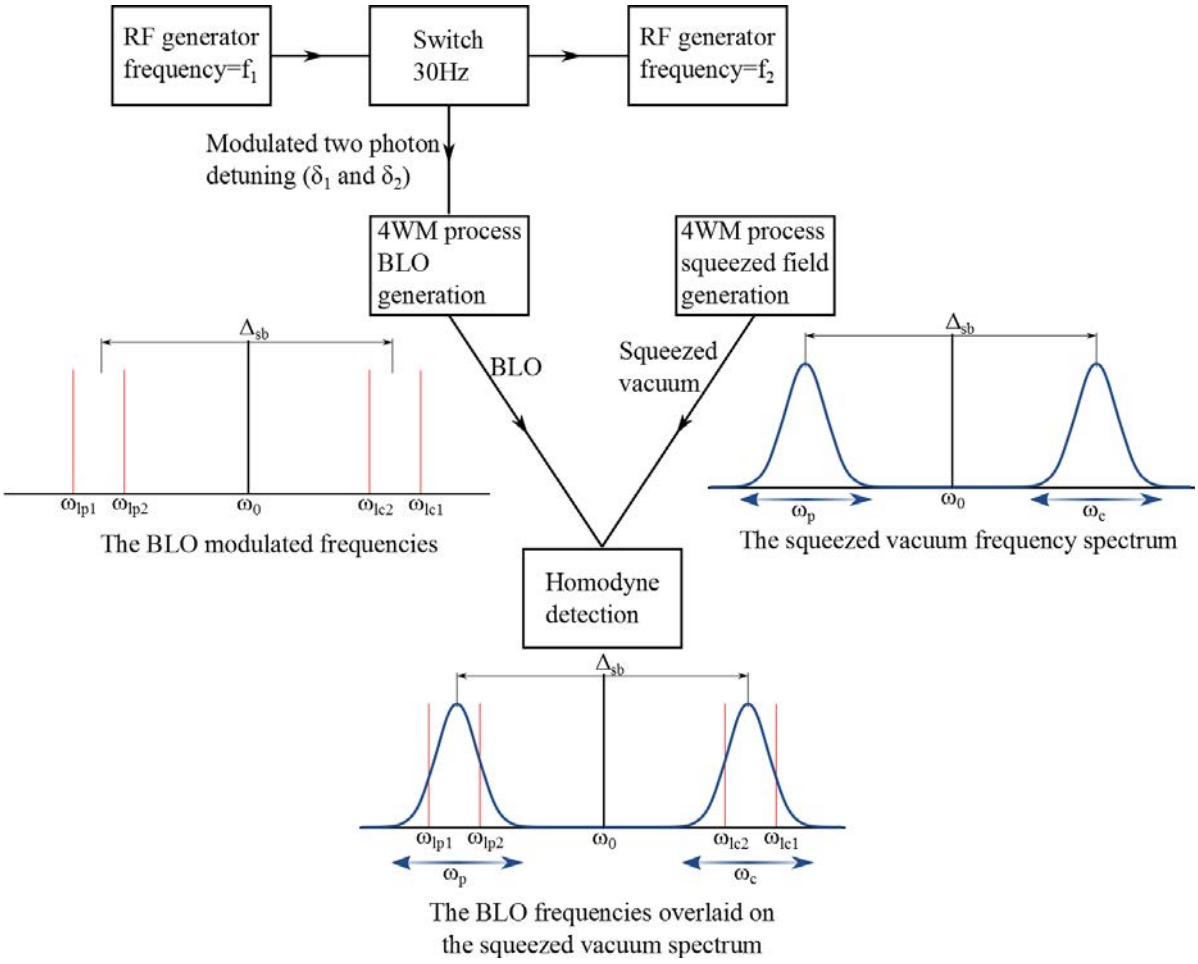

Figure 4.18: The block diagram for an experiment where the two-photon detuning of the BLO is modulated. The BLO two-photon detuning defines which parts of the squeezed vacuum field are measured. Here $\omega_{lp1,lc1}$ are the frequencies of the BLO components at the first two-photon detuning δ_1, and $\omega_{lp2,lc2}$ are the frequencies of the BLO components at the second two-photon detuning δ_2. Here Δ_{sb} is again the detuning between the sidebands, in the case of the 4WM process under investigation this is approximately 3 GHz. Throughout this experiment the analysing frequency, Δ_a, is kept constant at 1 MHz.

ings δ, and the phase compared. The simplest implementation of such an experiment would be to measure squeezing twice in succession, and compare the phases. However, there are phase instabilities in the experiment, in part due to the experiment having a large footprint, and there being many vibrations in the lab, and in part due to the non-uniformity of successive piezo scans. This means that the phase of the squeezing spectrum is not stable. Thus to accurately determine any change in the phase, the squeezing at two different two-photon detunings must be measured quasi-concurrently.

Practically, the concurrent measurement of the squeezing at two different two-photon detunings is achieved by modulating δ much faster than the piezo scans one wavelength of the squeezed vacuum path length. To

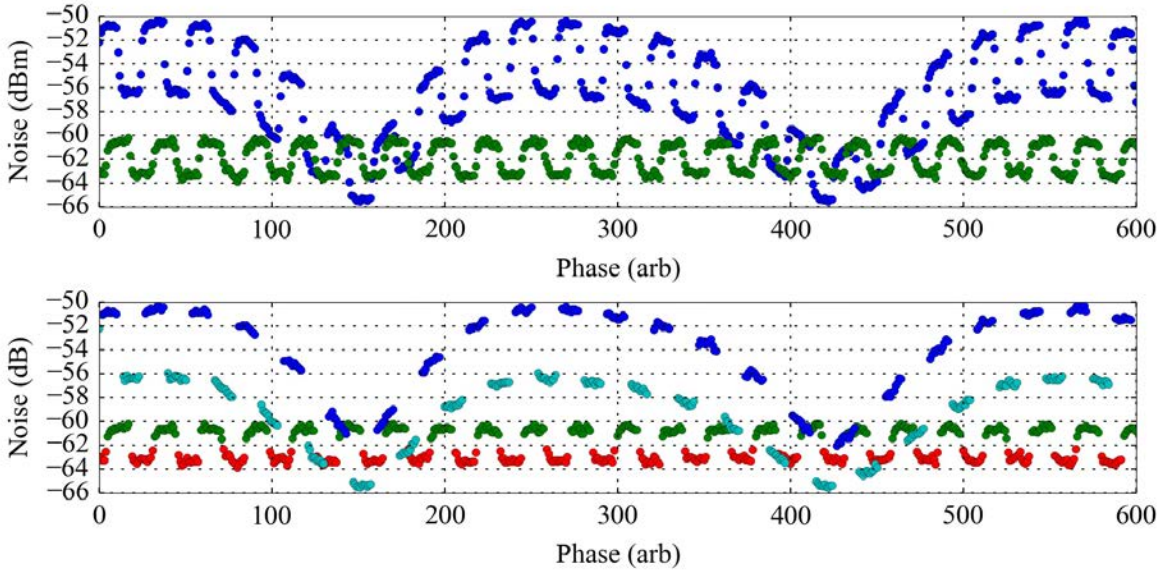

Figure 4.19: The process of extracting the squeezing data for a pair of two-photon detunings. The top panel shows the raw data as δ is modulated, the blue data being the squeezing signal, and the green the SN. There is a phase offset between the signal and local oscillator traces. The bottom panel shows the same data with the squeezing and SN signals split into the separate two-photon detunings. The blue and green data show the squeezing and SN signals for $\delta = -2$ MHz. The cyan and red data show the squeezing and SN signals for $\delta = 4$ MHz.

achieve this, I used two RF generators (HP 8642M and Rohde Schwarz SML02), operating at different frequencies, and an RF switch (Mini-Circuits ZASWA-2-50DR+), controlled with a square pulse generator to switch between the two frequencies. The block diagram of the process is shown in figure 4.18.

The modulation frequency of the two-photon detuning was set to 30 Hz, and thus necessitated the increase of the video bandwidth on the spectrum analyser to 100 Hz. This experimental setup can be used to check the phase delay, in the squeezing spectrum, between any pair of two-photon detunings within the squeezed region, extending over 40 MHz. The raw data clearly shows the effect of switching between the two frequencies on the usual noise scan, seen in the top panel in figure 4.19. As the two-photon detuning is changed, the power of the LO changes as well as the level of squeezing changing. This is evident in the level of the SN which is solely dependent on the LO power. The change occurs both due to the changing efficiency of the AOM as δ is changed, and due to the change in gain with δ seen in (figure 4.14(b)).

Since the spectrum analyser records data points faster than the switching speed of the RF, the raw data includes some points during the shifts, which should be removed. Then, the data can be split into two sets, one for each two-photon detuning. This process is shown in figure 4.19. Once the different frequencies are separated the relevant SN can be subtracted from the signal noise in the usual way to re-produce the usual

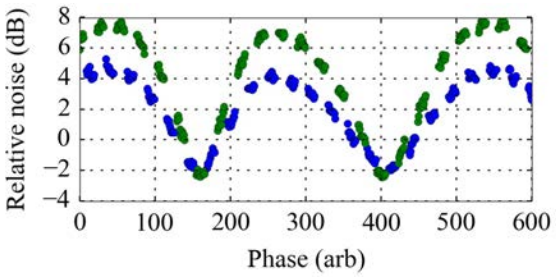

(a) Two-photon detunings of 4 MHz (green) and 10 MHz (blue).

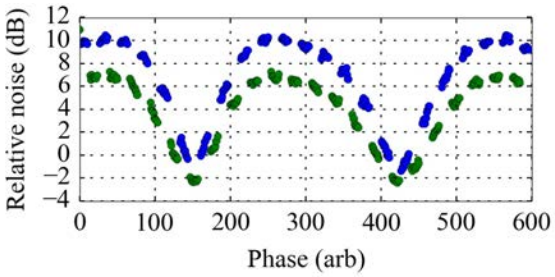

(b) Two-photon detunings of −2 MHz (blue) and 4 MHz (green).

Figure 4.20: The processed data, showing two squeezing signals, as the RF frequency is modulated, here plotted relative to SN. The data shows that the minimum noise occurs at the same phase within the scan at both frequencies.

squeezing graph for each frequency. These results are shown in figure 4.20(a), for the case of two-photon detunings of 10 MHz, in blue, and 4 MHz, in green. By inspection of the graph it is evident that the phase shift between the two measured squeezing spectra is insignificant. This means that, although both the phase of the BLO and the NEP rotate as the two-photon detuning changes, they do so at the same rate. Thus, there is no phase drift between the phase of the BLO and the NEP, and it can be concluded that the phase delay of the BLO is a valid witness to the phase rotation of the noise ellipse.

In order to ensure that the assumption that BLO phase change and NEP rotation occur at the same rate across the whole squeezing bandwidth, I have completed this same measurement with a number of different frequency separations. Across the whole squeezing region of −16 MHz to 24 MHz (figure 4.15) there is no evident change in relative phase between the noise ellipse and BLO phase. Here I only include two pairs of two-photon detunings shown in figure 4.20, comparing results on either side of the central frequency 4 MHz. The first example is for the case of two-photon detunings of 10 MHz and 4 MHz in figure 4.20(a). The second example is for the case of two-photon detunings of −2 MHz, in blue, and 4 MHz, in green in figure 4.20(b). It is worth noting that across the squeezing bandwidth, both the gain and squeezing do change (as previous shown in figure 4.14(b)).

This experiment has confirmed that the phase of the BLO tracks the rotation of the noise ellipse across the whole squeezing bandwidth. This means that the bright field components of the BLO can be used to provide all the information about the phase of the noise ellipse of the squeezed vacuum field. The experiment with bright fields is much simpler than any experiment with the vacuum fields due to the ease of measurement of bright fields. This is due to the clear definition of phase for a bright field.

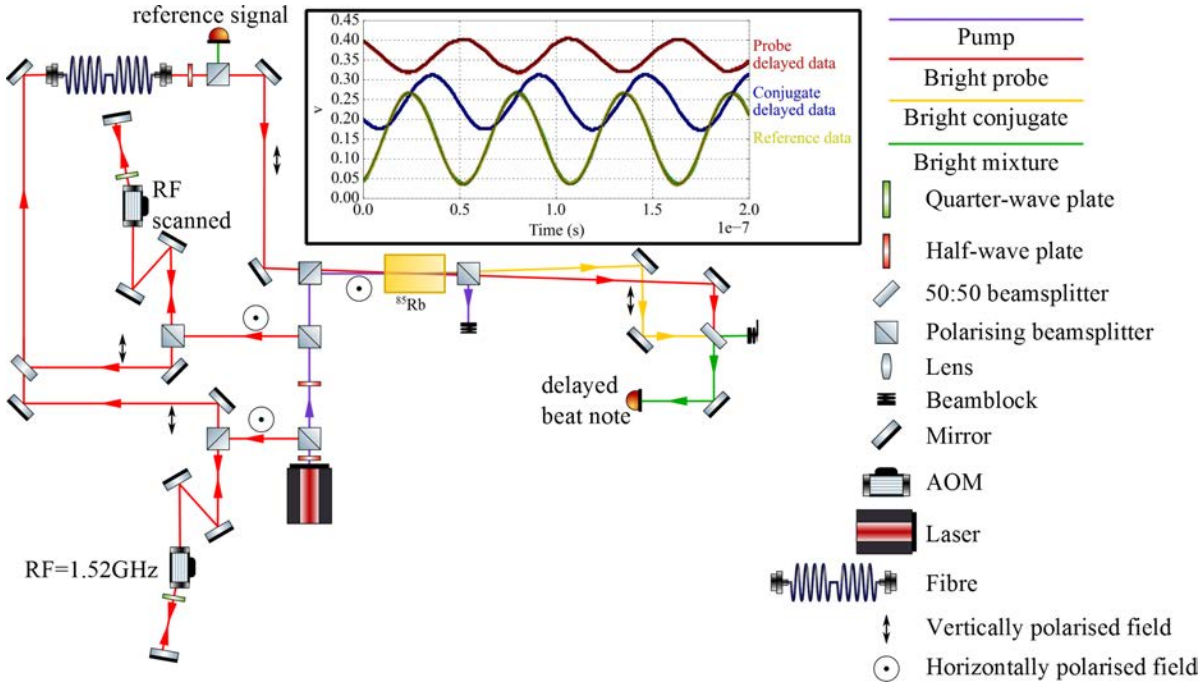

Figure 4.21: The simplified phase delay experimental setup. The change from the standard experimental setup (figure 4.2) occurs before the fibre input, where the seed fields created from two separate AOMs, driven at two different frequencies, are combined on a 50:50 beam splitter. The inset shows the beat notes. The blue shows the conjugate beat note after the cell, the red data shows the probe beat after the cell, and the yellow data shows the calibration beat taken before the cell, with the conjugate run, and the green data behind it shows the calibration for the probe run. The two-photon detuning for this graph is -14 MHz, hence the probe is being absorbed, and thus the amplitude of the conjugate beat note is larger than that of the probe beat note.

4.4.3 Noise ellipse phase rotation measurements

A experiment can now be performed to measure the phase delay due to 4WM using the bright field probe and conjugate components of the BLO. Again, this experiment requires the comparison of simultaneous results for two different two-photon detunings. The experimental setup is shown in figure 4.21. In this setup, two separate double pass AOM systems are used to create two seed fields with different frequencies. The two AOMs are driven by the two different RF generators. One is left at a fixed frequency, whilst the other frequency is changed. The two seed fields are combined on a 50:50 beam splitter before being coupled into the same single mode fibre. The passage through the same seed fibre ensures that the two frequencies propagate in exactly the same mode through the 4WM system. The overlapping of these two frequencies, on a beam splitter, generates a beat note at their frequency difference. If the phase of the field at one frequency is delayed with respect to the phase of other, then the phase of the beat note will be changed.

The interest in the experiment lies in the delay caused by the 4WM process. As such, the beat note is

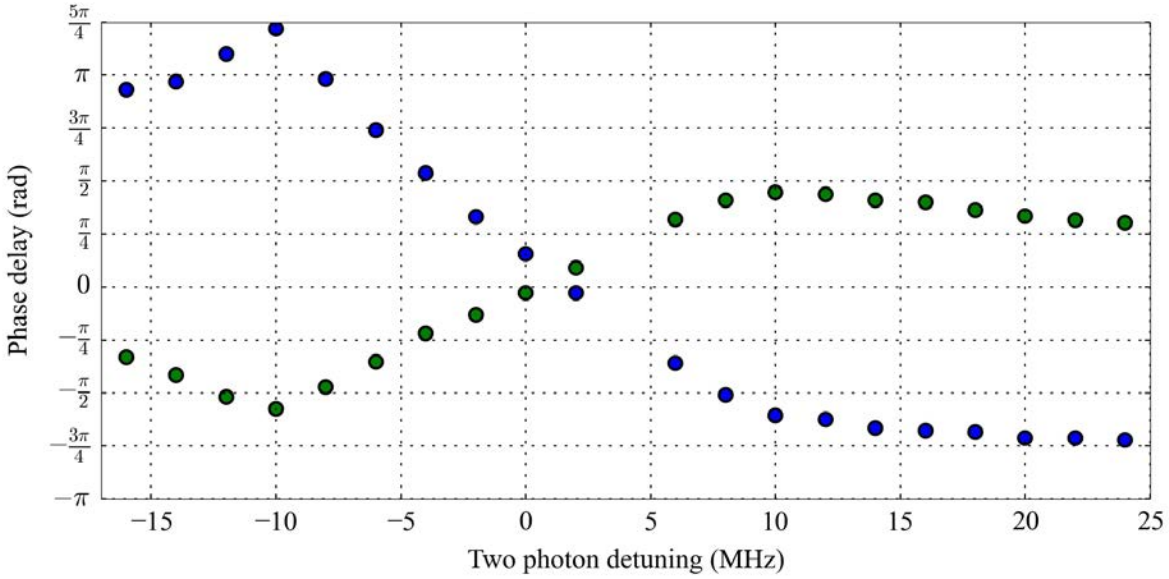

Figure 4.22: The phase of the probe (blue) and conjugate (green) frequency components, as extracted from graphs such as that in the inset in figure 4.21. One RF generator is kept at a constant frequency of 1520 MHz, whilst the other is changed. Here the frequency is represented as the two-photon detuning.

measured concurrently both before and after the 4WM process. The comparison between the reference beat note, taken before the 4WM process, and the beat note measured after the process provides a measure of the phase delay caused by the 4WM process. This experiment can be repeated measuring each of the probe and conjugate beat notes, for each different AOM frequency. In both the probe and conjugate case, the reference phase must come from the seed beat note at the probe frequency. The beat notes are recorded, and fitted with a sinusoid, as shown in the inset in figure 4.21. The phases of the sinusoid fits are extracted both before and after the 4WM. The phase delay due to 4WM is calculated by taking the difference between the phases of the signal before and after the 4WM cell. The data from the inset in figure 4.21 shows the how the individual phases of the probe and conjugate field advance. The phase delays are plotted in figure 4.22.

In the experiment, the probe and conjugate fields travel approximately 1 m between being measured before and after the 4WM cell. As such, due to the change in wavelength as the the two-photon detuning, δ, is changed (figure 3.2), the phase delay will change. In this case, it can be inferred that, for larger δ, the probe phase is advanced, and the conjugate phase must correspondingly be delayed. This phase change, due to the change in wavelength, corresponds to approximately $\pi/8$ rad delay over a frequency change of 40 MHz. However, the change in wavelength is not the sole contributor to the phase delay. Inside the vapour cell there is a slow light effect, which increases this phase delay due to propagation, and further effects from the 4WM process itself.

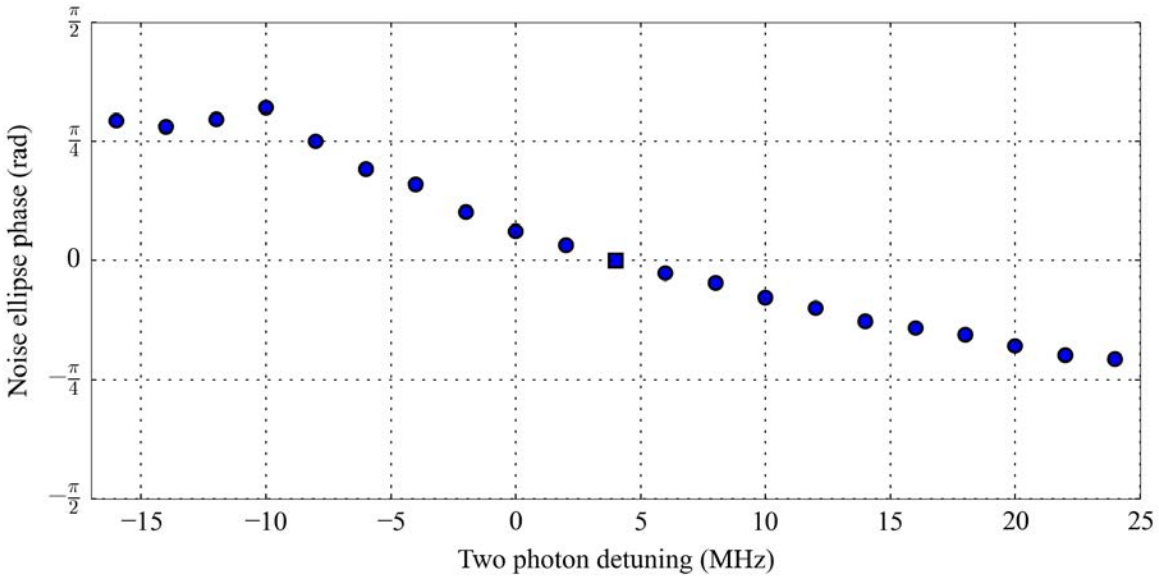

Figure 4.23: The phase rotation of the noise ellipse, as calculated by combining the phase changes of the probe and conjugate frequency components in figure 4.22. The phase rotation is measured relative to $\delta = 4$ MHz, as such this point is taken to have a phase of 0 by definition.

Ultimately, we are interested in how the NEP advances, which arises out of these phase changes. In order to calculate the NEP we must take the average of these phases as derived in appendix A. (Note that the derivation in appendix A is the same as that shown in section 3.8, only with a different reference for the phase.) Thus, any phase delay due to a change in wavelength will exactly cancel out, whether it be in free space propagation or propagation through a slow light medium. However, the phase change from the 4WM process itself will remain, and this will effect a change in NEP. The calculated NEP is shown in figure 4.23, where the phase of the squeezed vacuum noise ellipse can be seen to rotate from $\pi/4$ to $-\pi/4$ as the two-photon detuning is varied.

In both the measurements of the phase delay of the probe and conjugate components, and the NEP rotation, there is an unknown factor caused by the optical path length between the detectors measuring the beat note before and after the 4WM process. This corresponds to a global phase, and is small due to the small path length. From figure 4.22 it can be seen to be approximately $\pi/4$. The exact value of the phase delay is insignificant as any adjustment can be corrected with the correct choice of LO phase.

In an interferometer, the error on the measured phase difference between the two paths depends on light power as well as squeezing parameter. In order to improve the overall SQL, a bright squeezed field can be used (see section 2.7.1). A bright squeezed field can be formed by mixing a coherent LO with a squeezed field. This can be done on the input mirror of the interferometer (see figure 2.10). The squeezed quadrature

of the resultant field within the interferometer is defined by both the NEP in the squeezed signal and the relative phase between the LO and the signal field.

Thus, with the correct choice of LO phase the squeezed field investigated in figure 4.23 could be set to have a minimum amplitude noise at a detuning of $\delta = -16$ MHz. At the same time, due to the rotation of the NEP caused by the 4WM process, the field would have a minimum phase noise at a detuning of $\delta = 24$ MHz. As such, the 4WM process can be used to generate a field that is amplitude squeezed at low analysing frequencies and phase squeezed at high analysing frequencies. However, when a BLO is used, and the components are tuned to the centre of the squeezed region, then at large analysing frequencies one pair of correlated sidebands will show amplitude squeezing, and the other pair will show phase squeezing. As such, if a BLO is used, the mixing of four sidebands effectively removes squeezing (section 3.8). Alternatively, if the BLO is centred outside the squeezed region, then, at best, the homodyne detection process will measure one pair of correlated sidebands, and one pair of uncorrelated sidebands at the QNL. At worst in this case, the homodyne detection process will measure one pair of correlated sidebands, and one pair of uncorrelated sidebands far above the QNL. Again the mixing of the four sidebands at best significantly reduces the measurable level of squeezing. As such, a MLO would be needed to make significant use of the NEP rotation, where squeezing would then occur at an analysing frequency close to 3 GHz.

Despite the complications, covered in this section, I have shown that the BLO can effectively characterise the phase of the correlations across the squeezing spectrum. This phase characterisation is in addition to the characterisation of the squeezing spectrum as a function of frequency, and as such the BLO can be seen to be a complete characterisation tool for the squeezing spectrum, when combined with the spatial characterisation shown in the next chapter.

4.5 Multi-spatial-mode characterisation

4.5.1 Introduction

Fundamentally, a squeezed state is made up of correlations within a certain mode, or set of modes. Homodyne detection can be thought of most simply as a process whereby the LO amplifies the noise on the signal beam (equation (3.34)). In the homodyne detection process, the mode of the LO specifies the mode of the squeezed vacuum field that is measured. In the case of using an LO to measure the noise of a single-spatial-mode quadrature-squeezed state, the measurable level of squeezing is strongly dependent on the overlap between the LO and the signal field.

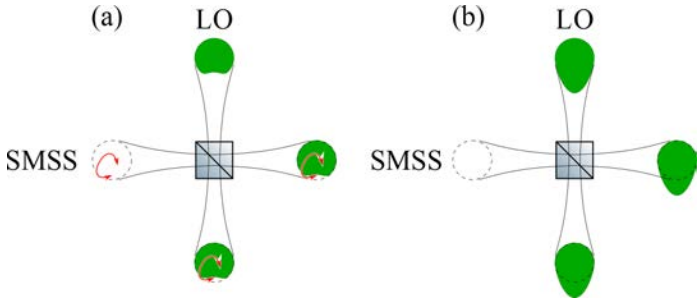

Figure 4.24: The mixing of a bright LO (green) with a squeezed vacuum field (dotted). (a) shows the case where the LO does not fully fill the mode of the squeezed vacuum field. This causes a reduction in the measured squeezing due to only including part of some of the correlations, eg. the point indicated by the red arrow. (b) shows the case where the LO extends beyond the squeezed vacuum mode. This causes a loss of measurable squeezing due to the inclusion of additional vacuum fields, which are at the QNL.

The effect can be explained by considering the noise reductions as correlations between frequency sidebands, within the squeezed mode. These correlations mean that when one part of the squeezed vacuum mode has an positive fluctuation in a particular quadrature, the rest of the field must have a negative fluctuation in the same quadrature. In this picture, if the LO is smaller than the squeezed mode, causing a mode mismatch, then some of these correlations are broken. This means that excess noise will then be mixed in (figure 4.24(a)). Similarly if the LO extends beyond the squeezed state (figure 4.24(b)), then the LO will also amplify some of the vacuum state around the squeezed state. This will lead to an additional contribution at the QNL being measured in the homodyne detector. This additional vacuum noise will reduce the measurable level of squeezing.

In actuality, these two cases of poor mode matching between the LO and squeezed mode are two manifestations of the same effect. Any mode-mismatch can be seen as mixing in additional spatial modes, with vacuum fluctuations at the shot noise level, thus corresponds to a loss of squeezing. Thus, in the single mode case, the LO must match exactly the shape of the squeezed mode if the optimum squeezing is to be measured.

The concept of MSM squeezing, corresponding to perfectly local squeezing was proposed by Kolobov [48]. In the case of perfect MSM squeezing, all correlations are confined to point locations within the transverse spatial profile. Any LO mode that remains within the spatial extent of a MSM squeezed field will measure squeezing at the same level. Figure 4.25(a) shows the alignment where squeezing can be measured in the single mode case. Figure 4.25(b) and (c) respectively show the freedom of choice for positional alignment and mode shape of the LO allowed for measuring a MSM quadrature squeezed state. In practice, with a thick medium, the squeezing cannot be fully local as explained previously in section 2.5. Furthermore, whilst there is a freedom of choice in the position at which to measure the squeezing, the phase of the BLO is still

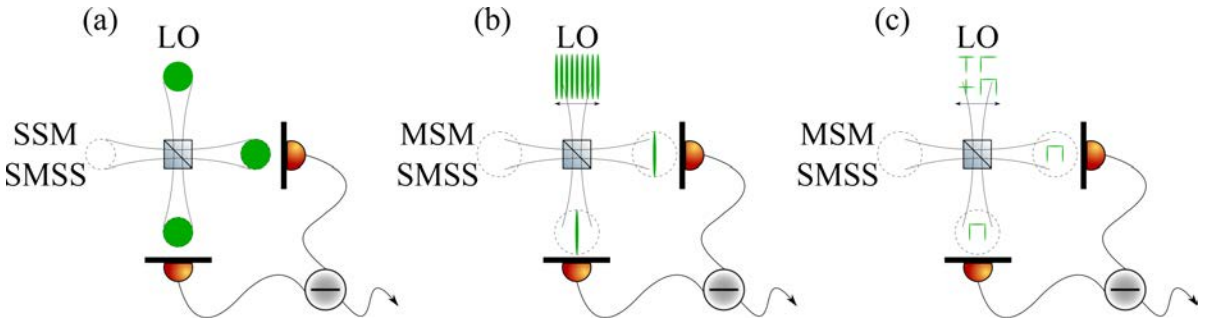

Figure 4.25: The homodyne detector with a variety of inputs. (a) a SSM squeezed state, with the necessary mode matched LO. (b) a MSM squeezed vacuum input and the LO mode input with freedom to select position. (c) a MSM squeezed vacuum input and the LO mode input with freedom to select shape.

restricted. For example, if, at every location within the squeezed field, the same quadrature is squeezed, then the LO must have a flat wavefront. Conversely, if the quadrature that is squeezed rotates across the squeezed region, then so too must the LO phase.

In section 2.7.2, I discussed how MSM squeezed light could be used to improve the resolution of an imaging system. In section 2.5, I discussed how a thin gain medium can generates a MSM squeezed field, and how a realistic thick medium places a limit on the number of modes. In section 3.5, I elaborated on how the cavities required to generate strong quadrature squeezing using PDC remove this MSM nature from the field. Since the gain medium in the present experiment is a resonant 4WM process, with large gain, no cavities are required to obtain strong squeezing. As such, the spatial structure of the squeezed field remains limited only by the thickness of the gain medium. In this section, I present an experimental investigation to characterise the MSM nature of the squeezed field. I will calculate the number of squeezed modes measured and compare it to the theoretical number of squeezed modes present. This experimental result has been published [86].

4.5.2 Experimental techniques

The spatial character of the quadrature squeezed vacuum field can be investigated by probing it on a scale much smaller than its total size. Throughout this thesis I have been working in the near field. As such, it is the near field mode structure that is under investigation. The mode of the squeezed vacuum that is measured depends solely on the mode of the LO used. Thus, to select a mode, the LO field must be appropriately shaped in the near field.

The simplest way to shape a beam is to use a mask which blocks part of the seed field. Necessarily such a mask will have sharp edges, which will introduce high order spatial frequencies. However, the 4WM system has a finite spatial bandwidth, and as such cannot support high order modes. Consequently, any such high

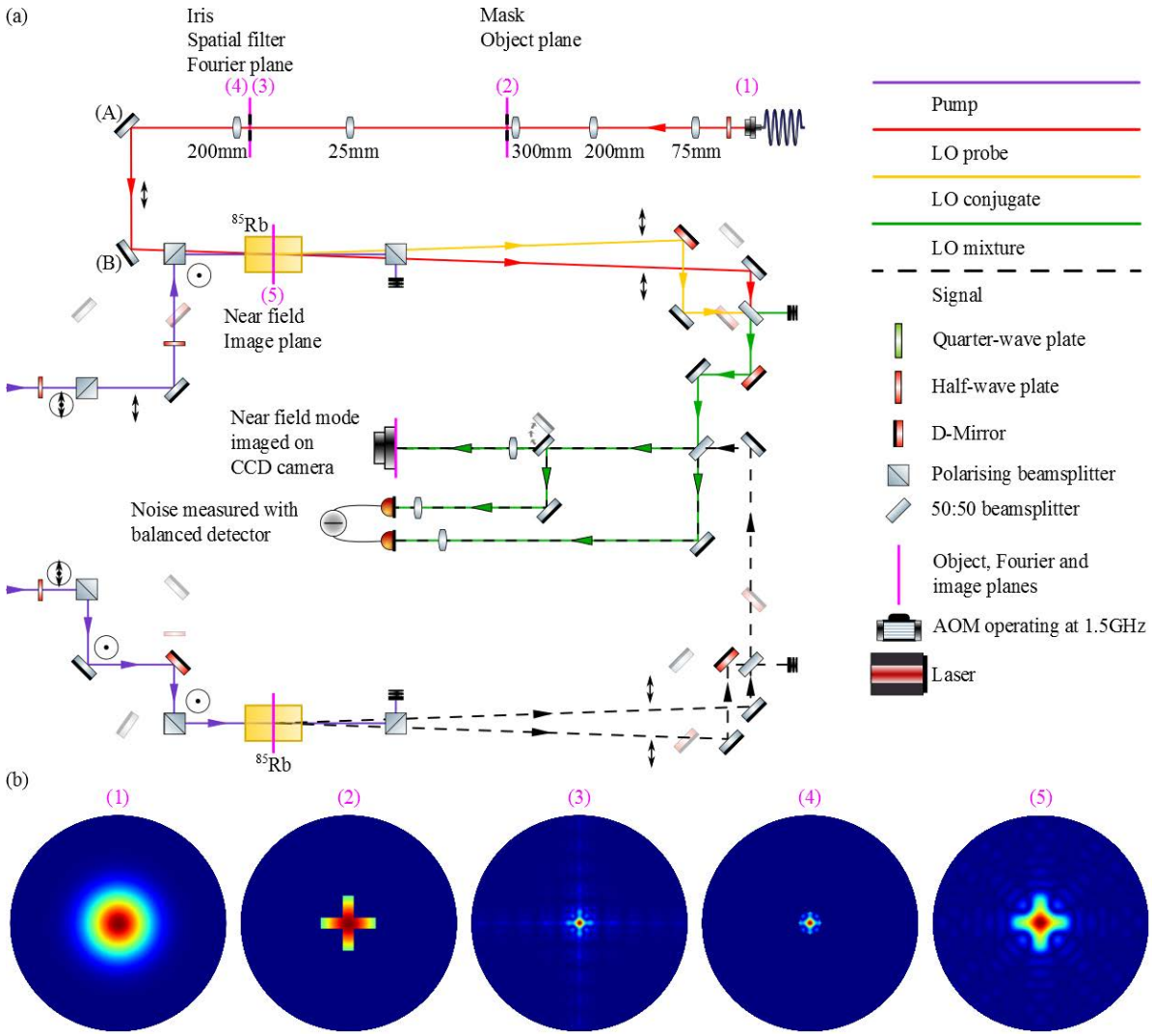

Figure 4.26: The experimental diagram for investigating differing spatial modes. (a) shows the full experimental setup. (b) shows the beam profile for a LO at numbered positions in the beam path. In this diagram a hypothetical "+" shaped mask is used to shape the LO, and some higher order spatial modes are filtered using the iris in the Fourier plane. In the experiment, the LO and signal optical paths and 4WM processes are separated vertically. Here they are shown as mirror images, with the LO path being at the top of the diagram and the signal path at the bottom. The unused mirrors in each case are faded out for clarity.

order modes instead contribute additional noise, at or above the SN, to the final detection. Thus, an iris is placed in the Fourier plane of the mask to remove the high order spatial frequencies.

The use of a mask and imaging system to control of the near-field shape has already been discussed in section 4.2.2. The simplified experimental diagram for this experiment is shown in figure 4.26(a), with the profile of a hypothetical LO as it progresses through the experiment shown in figure 4.26(b). In the seed image (2) the shape of the seed after the mask is shown. Image (3) shows the field after propagation to the Fourier plane, corresponding to the far field. Image (4) shows the field after the spatial filtering iris is applied. The final image, (5), shows the new mode shape with the high order spatial modes removed.

The aim of the experiment is to measure the maximum number of squeezed modes generated by the 4WM system. To do this the same squeezed vacuum field should be probed with a number of independent LO modes, and the number of these that are squeezed should be counted. Mathematically, this is a process known as tiling, where a number of orthogonal modes are fitted into a particular region [134]. In order to achieve the highest number of squeezed modes, one would like to reduce the LO to its smallest possible size in the near field. The simplest mode would be a Gaussian mode. This can be created by using an iris as a mask. However, as the mode size is reduced, by closing the iris, the power in the seed field drops significantly. As the seed power drops, so does the level of squeezing that can be measured, due to the electronic noise (figure 4.13(b)). This results in measurements with mode sizes larger than the coherence area showing no QNR despite the signal field being squeezed.

A slit, rather than an iris, makes a better mask for this experiment. The slit still reduces the LO field in one direction down to a small size, whilst also retaining more of the beam power due to the LO still retaining its full extent in the perpendicular direction. This rectangular LO can then be used to count the number of modes along a certain direction, by translating it in the direction of its narrow dimension. To acquire a full two dimensional mode count this process is undertaken on two perpendicular directions.

The initial concept was to move the mask within the seed field to change the mode selected in the detection. At the mask point the LO has a Gaussian shape. As such, an off-centre mask allows less power transmission than an on-centre mask. When the mask is at the edge of the field, the final LO power is sufficiently low to limit the level of QNR that can be measured. Instead, to ensure the highest possible power LO, the mask was placed in the centre of the seed field. The seed field can then be translated across the near field using a pair of mirrors, labelled A and B in figure 4.26. In this setup it is important that the angle between the seed and pump field is kept constant. This can be achieved by ensuring that the LO does not move in the far field. That is to say that the seed propagation direction of the LO remains constant.

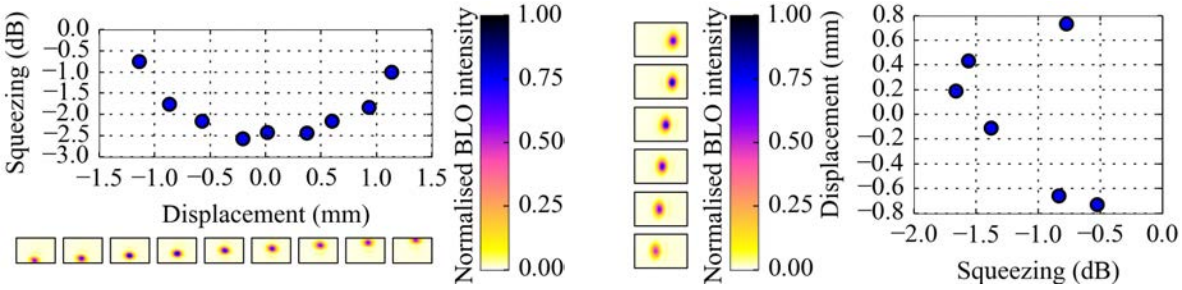

(a) The analysis with a horizontal slit, giving 6 squeezed modes at this mode size.

(b) The analysis with a vertical slit, giving 4 squeezed modes at this mode size.

Figure 4.27: MSM squeezing in a single field analysed in the vertical (a) and horizontal (b) directions. The images show the shape and position of the LO field, corresponding to the mode measured. The graphs show the squeezing level measured at each BLO position.

In order to measure the position of each mode, the near field is imaged on a CCD camera. At each different LO position, and hence probing mode, the QNR is measured, with homodyne detection, and an image of the mode is recorded, with a CCD camera. Throughout the experiment only the alignment of the LO field is changed, with the squeezed field remaining constant, and the imaging system and camera also remaining constant. This ensures that the reported MSM nature is that of a single field, not that of many fields.

4.5.3 Results and discussion

The experiment is completed using a slit as a mask, generating a long and narrow LO field. This field is then translated across the near field in the direction of its small dimension using the alignment mirrors. Initially, the obvious choice for these directions would be to use the horizontal and vertical, and indeed this method does produce a measurement of the MSM nature of the squeezed vacuum field. The initial results using this method are shown in figure 4.27.

These results show a large asymmetry in the number of squeezed modes available in the horizontal and vertical directions. There are two main effects that result in asymmetries of this sort. Firstly, the spatial emission spectrum of the 4WM, and the overlap of the two RGRs causes an asymmetry. When overlapping the RGRs horizontally, there is a larger area of overlap in the vertical direction as compared to the horizontal direction, see figure 2.9. This results in a different number of accepted modes in the horizontal and vertical direction.

Secondly, there are asymmetries due to the space available for each field on the optics. Fourier optics tells us that a small size in the near field corresponds to a large diffracted size in the far field. This effect

presents a practical problem with the edges of the field potentially being clipped by the finite size of the optics used. In our case one inch optics are used. In the horizontal direction the size available for each beam splitter is further reduced by its thickness and the relatively acute angle needed to achieve a 50:50 splitting on the beam splitters. In the vertical direction, which is used to separate the BLO and the signal fields, both the signal and LO fields must pass through the same optics, halving the size available for each field. Where the BLO field is clipped by the optics, so too is the signal field. This clipping corresponds to the difficulty of collecting the full RGR, and as such the number of squeezed modes is reduced.

For greater symmetry in mode number between the two perpendicular directions, I chose to use the diagonal directions for the further development of the experiment and main results. In this case, each beam is masked to reduce the near-field size along one diagonal, leading to far-field expansion along this same diagonal. Each perpendicular diagonal then fits equally well into the RGRs and through the space available in the optics.

Using diagonal slits as masks for the LO, and with the usual parameters, corresponding to a 4WM gain of 4 it is possible to measure squeezing over a wide range of BLO positions, shown in green in figure 4.28(a) and (d). The corresponding BLO mode images are shown in figure 4.28(b) and (e) respectively. In this case the BLO mode waist dimensions are 0.45 mm by 0.61 mm. A better set of parameters can be chosen for the 4WM process, whereby the power of the signal pump is reduced and the two-photon detuning is reduced. The new parameters reduce the gain to 2. With the reduction of gain the maximum level of squeezing is reduced, as can be seen in the blue data in figure 4.28(a) and (d). However, the spatial bandwidth of the squeezing process is increased in this case. Additionally, the BLO mode dimensions can be reduced down to 0.31 mm by 0.58 mm (figure 4.28(c) and (f)). These new parameters allow QNR to be evidenced on a larger number of spatial modes, seen in the blue data in figure 4.28(a) and (d).

The images in figure 4.28 clearly show that the BLO size, given by the slit width, are different in the case of the two data sets, with the smaller mode size corresponding to a lower reduction in the quantum noise. It is important to note that this is indeed a general trend, that the squeezing reduces with the mode size, as explained in section 2.5. This occurs due to the reduction in mode size causing a greater coupling between adjacent modes in the gain medium.

A calculation of the maximum number of squeezed modes requires a knowledge of the size of the coherence area, l_{coh} defined as the mode size where the level of QNR begins to drop significantly. In the context of this particular experiment, the coherence length can be found by measuring the level of squeezing as the slit size is reduced, and hence the mode size within the cell is reduced. In order to accurately measure the size of

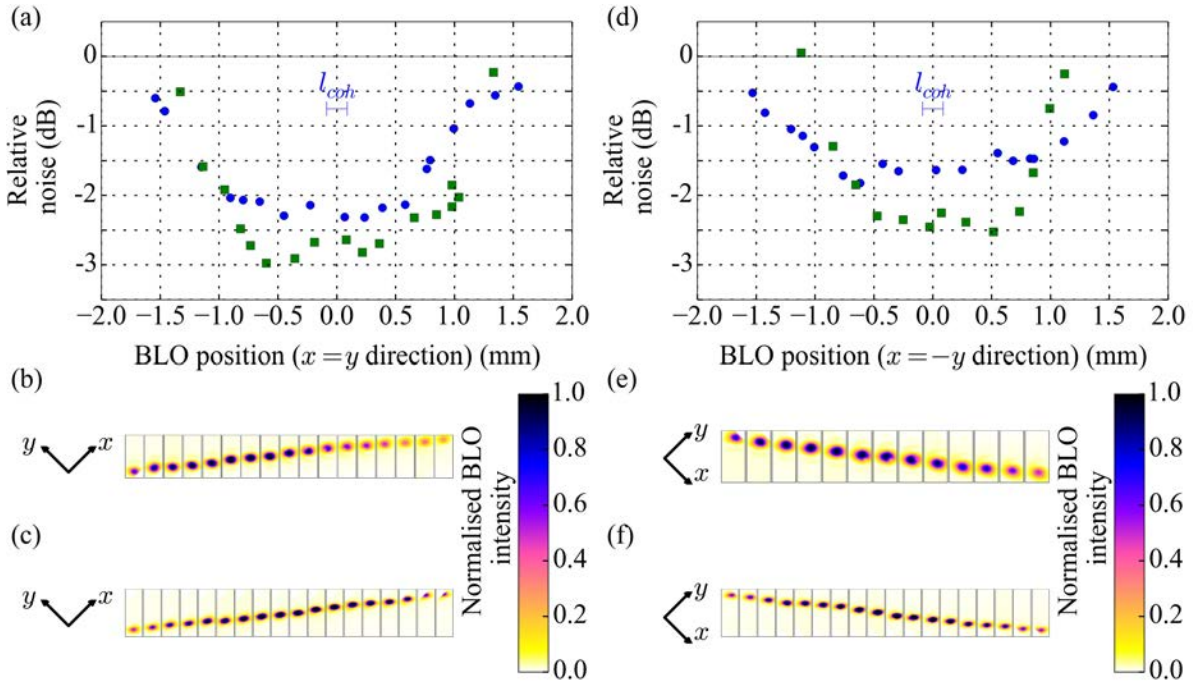

Figure 4.28: MSM squeezing analysed in diagonal directions. (a) shows squeezing as a function of BLO position as it is moved along the $x = y$ direction, (b) and (c) show images of the BLO mode, corresponding to the green and blue data respectively. The images show the mode of the squeezed field that is measured, and the BLO position within the squeezed field is extracted for (a). (d) shows squeezing as a function of BLO position as it is moved along the $x = -y$ direction, again (e) and (f) show the images of the modes measured in the green and blue data respectively. The black lines indicate the QNL, the green squares show the data for parameters resulting in a gain of 4, with BLO mode waist dimensions of 0.45 mm by 0.61 mm, and the blue circles show the data for parameters resulting in a gain of 2, with BLO mode waist dimensions of 0.31 mm by 0.58 mm. All the results are corrected for the electronic noise floor (at -13 dB). The scale bar labelled l_{coh} indicates the size of the coherence area.

the LO in the near-field it is imaged on a camera, and measured using a Gaussian fit. The level of squeezing is plotted as the mode size is reduced in figure 4.29. The graph shows that, with a mode size of 0.18 mm, a small level of QNR can still be measured. This size is taken to be the coherence area, and is indicated as l_{coh} in figure 4.28 for comparison purposes.

A lower bound for the number of squeezed modes in the field can be calculated from the size of the coherence area (extracted from figure 4.29), and the squeezed region (extracted from figure 4.28). The size of the squeezing region can be extracted from figure 4.28 as $l = 3.1$ mm in both the $x = y$ and $x = -y$ directions. Using these values, and the coherence area, the number of squeezed modes can be calculated

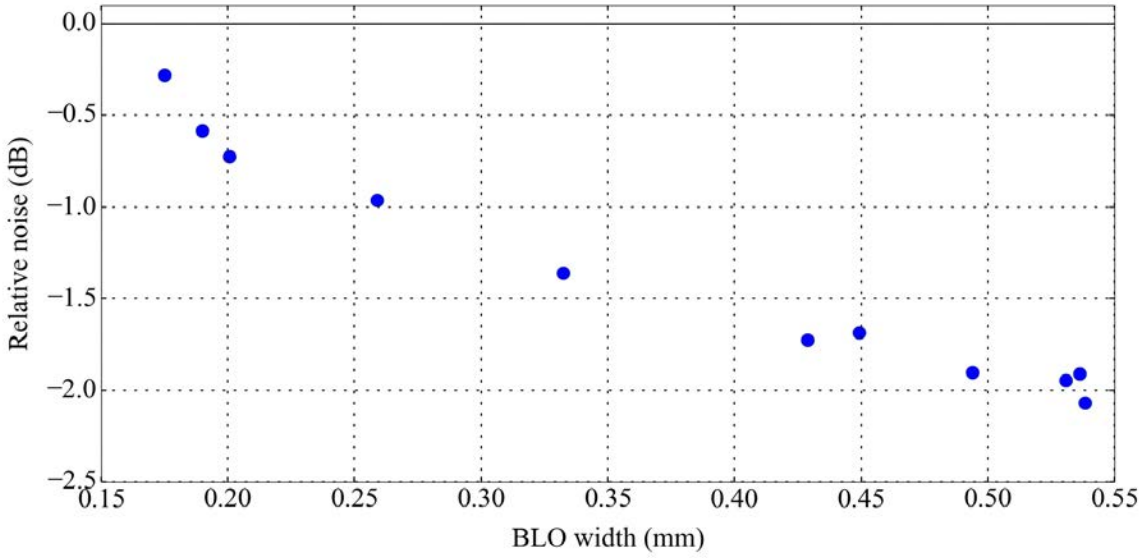

Figure 4.29: How the squeezing level changes as a slit, imaged in the centre of the 4WM cell, is closed within the beam path. The widths are extracted from a series of images where the near field, in the centre of the cell, is imaged on a camera. The coherence area can be extracted as the point where the level of squeezing begins to drop significantly.

using equation (2.39) as

$$\begin{aligned} N_{exp} &= l^2/4l_{coh}^2 \\ &= 75. \end{aligned} \tag{4.4}$$

Given that the cell length is 12.5 mm, and using equation (2.39), we can calculate the theoretical maximum number of modes as

$$N_{theo} = 315. \tag{4.5}$$

The theoretical number of spatial modes is thus much larger than the experimentally measured value. This is primarily due to geometric constraints. In the experiment, only part of the conical emission spectrum is collected. This is shown as the RGRs in figure 2.9. However, in the theoretical calculation the full conical emission spectrum is considered. Furthermore there is a slight ambiguity as to the exact definition of the coherence area. Theoretically, the coherence area is the length where the level of squeezing starts to drop significantly. This corresponds to the point where, in the far-field, a significant proportion of the probe region lies outside the RGR. Experimentally this is extracted by measuring the change in the level of squeezing with the local oscillator size, as in figure 4.29. However, the exact point where squeezing starts to drop significantly

is subjective, and as such may lead to some inaccuracies in the measured mode number.

I have been able to generate a MSM squeezed field, and directly measure its MSM character. The field proves to contain at least 75 squeezed modes, showing significant improvement over previous published measurements. Previous direct measurements, of MSM squeezed light, produced using PDC systems have been limited to only a few spatial modes [79, 126]. This result also offers significant improvement over the inferred 12 symmetric spatial modes produced using a 4WM process [84]. It also lifts the restriction that the squeezed modes must be symmetric (section 2.6.3). Thus, the presented system currently offers the best potential source of squeezed light, for the use of direct illumination quantum imaging.

CHAPTER 5

IMAGING SQUEEZED LIGHT

5.1 Introduction

In this thesis, I have presented the use of a 4WM gain process to generate MSM squeezed light (section 4.5). I discussed the potential application of such MSM squeezed light in quantum imaging (section 2.7), to achieve resolution below the QNL. Throughout this thesis, the characterisation of the squeezed light has been in the frequency domain. This shows that the total intensity fluctuates less than the QNL at some frequencies. In a super-resolution imaging system, using direct illumination with bright light, the measurements are made as a snapshot taken with a camera. Such a snapshot is a representation of the intensity of the field, integrated over a small period in time. Such measurements are in the time domain. For the resolution to be improved below the QNL, the bright light, in an imaging system, must be replaced with a bright quadrature squeezed field. The reduction of noise, in this field, must be observable in the time domain.

The goal of the experiment presented in this chapter is ultimately to perform a direct measurement of the QNR in the time domain. Previously, no technique has been developed to analyse the spatial nature of the quantum noise in the time domain. Thus, to investigate the MSM nature of the QNR in the time domain, such a technique must first be devised. The proposed method is to achieve this by imaging a bright squeezed field on a CCD camera. The reduced quantum noise will be evidenced by reduced intensity fluctuations across a series of images taken as snapshots in time. These snapshots will show the transverse spatial profile of the field. The spatial information of the image allows the MSM nature of the quantum noise to be directly analysed. This can be achieved by selecting regions, or modes, of the field, by analysing the fluctuations over a given set of pixels. This chapter focuses on my work to measure the spatial quantum noise of a field in the time domain, by developing such techniques.

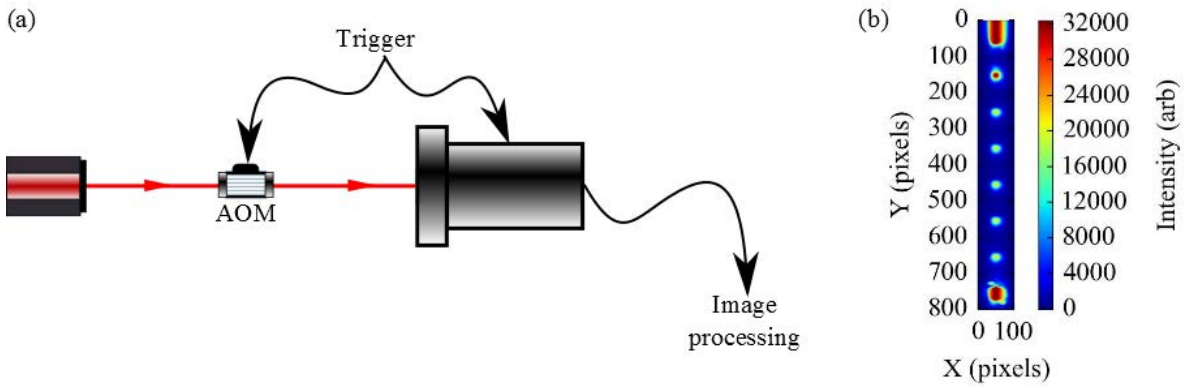

Figure 5.1: The simplest use of the camera to image a laser field. (a) shows the experimental setup, where the laser field is pulsed using an AOM, set to expose at the same time as the camera through a shared trigger. (b) shows a set of images measured experimentally.

5.2 Imaging noise at the quantum noise level

The aim of the experiment is to image the quantum noise of a laser field. This is achieved by using a high quantum efficiency camera with a low technical noise. The most simple setup for imaging the noise on a laser field is shown in figure 5.1(a). The laser field should be pulsed such that it only reaches the camera whilst the camera is exposing. This requires that there is an AOM (or other fast switching mechanism) in the beam path, and that the camera and AOM are triggered by the same input. A sample set of images is shown in figure 5.1(b), these images are taken using the camera's "kinetics" mode, as explained in section 5.2.2. The quantum noise on the images shown will be extracted by investigating how these images differ from an average intensity profile (section 5.3).

There are a number of noise sources that produce classical noise at a level above the QNL. The additional classical noise makes imaging the quantum noise experimentally difficult. To measure the quantum noise, the classical noise must first be significantly reduced, or removed entirely. In the frequency domain the effect of the classical noise sources was significantly reduced by the use of balanced detection (section 3.7.2). To prove the usefulness of the squeezed light, for quantum imaging, the squeezing must be measured on a single bright field. As such, only direct detection of a single bright signal beam is used, in the time domain. Thus, there is no common mode rejection of any classical noise, and, consequently, the classical noise sources have a much more significant effect. In this section, I will discuss the classical noise sources and how the effects can be mitigated in the time domain.

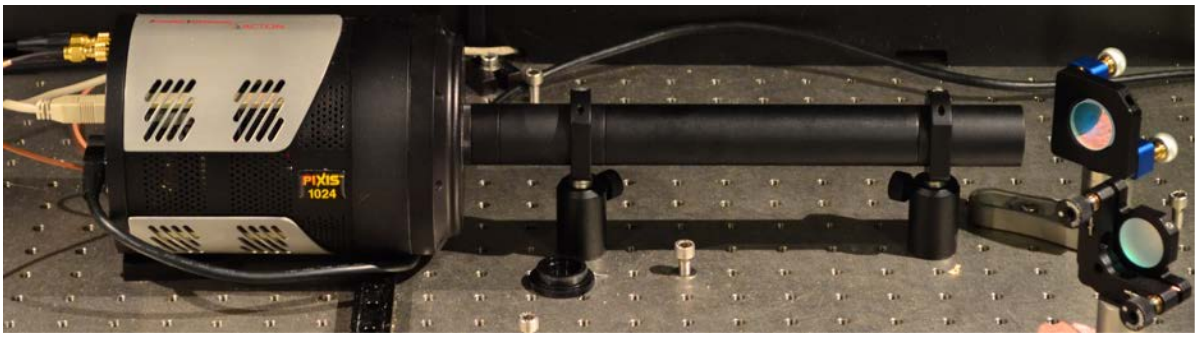

Figure 5.2: The PIXIS camera, with the attached long lens tube, used to reduce the angle of acception for the camera, and hence reduce the background light.

5.2.1 Background light

The first classical noise source is background light. This can come from any light source within the lab, such as the room lighting, or screens on instruments and computers. In the frequency domain, such background light was not important due to the use of a bright LO to amplify the noise in the selected mode, defining both the spatial mode and the frequency measured, and the small size of a photodetector. This background light becomes a problem in the time domain due to the large size of the CCD chip. Here, the bright signal beam must be expanded over a large number of pixels of the CCD, reducing the power incident on each pixel. The background light has no such reduction in the intensity, making it more significant on the CCD than on the photodetector.

The experiment, and especially the camera, must be shielded from any background light to minimise its effect on the results. To achieve this, a long lens tube is attached to the front of the camera (figure 5.2), which reduces the acceptance angle for the background light. The detection part of the experiment is placed away from the powerful pump beams. The camera, and immediate surrounding optics, are boxed up to further reduce incident stray light. Finally, the whole experiment is surrounded by blackout curtains. Despite all of this light protection, the effect of the background light can still be seen on long exposure images. This light could be further reduced using optical filters. However, any filter that sufficiently attenuates the background light will also absorb some of the signal light, which will act as a loss, thus making the quantum noise harder to measure.

5.2.2 Technical noise

Any detection system will add noise to the signal that it is measuring. In the case of a homodyne detector and spectrum analyser system, this is the electronic noise floor, introduced by imperfect electronics. The

noise floor was discussed in section 4.2.5, and shown in figure 4.11. This noise floor was the reason for the use of detector C, for the balanced homodyne detection measurements, throughout this thesis. The same care must be taken to choose a camera with low noise. The technical noise on measurements with a CCD chip is made up of two factors. The first source of noise is the dark current. This is the rate at which charge builds up in each pixel when there is no light incident on the CCD chip. The second noise source is conversion noise, arising from the process where the charge in each pixel well is converted into a digital signal. In order for a camera to achieve a low noise floor, both of these noise sources must be small.

A low quantum efficiency can be treated as a loss. Such a loss will reduce the level of squeezing that could be measurable with the camera (see section 3.7.1). Thus the camera must have a high quantum efficiency for converting incident photons into electrons in the pixel wells. The CCD camera chosen to meet these requirements is the Princeton Instruments PIXIS-1024BR eXcelon, and its relevant specifications can be found in table 5.1.

Item	Specification
Shutter open/close time	8 ms
Operating temperature	$-70°$C
Frame size	1024×1024
Pixel Size	13 μm
Analogue to Digital conversion rate, fast readout	2 MHz
Analogue to Digital conversion rate, slow readout	100 KHz
Analogue to Digital conversion noise, fast read out	9 e^- per pixel
Analogue to Digital conversion noise, slow read out	3 e^- per pixel
Dark Current	0.02 e^- per pixel per second
Quantum efficiency @λ =795 nm	99%
Vertical shift rate	3.2 μS per row

Table 5.1: The specifications of the PIXIS high quantum efficiency camera

In addition to the measurement noise, the bright field will have some classical noise due to fluctuations in the laser power and from vibrations on mirrors within the optical setup. The 4WM gain can fluctuate due to changing pump power, or temperature of the rubidium vapour, which will add further classical noise to the bright field. In balanced homodyne detection, this classical noise is removed by common mode rejection. Direct detection of a single beam has no such common mode rejection. Thus, the classical noise on the bright field becomes very important. The fluctuations are low frequency fluctuations and as such become more evident with longer time frames. This is a typical characteristic of technical noise, where the noise roughly falls as $1/f$. Thus, this noise is minimised by minimising the time elapsed between subsequent images.

There is an inverse relationship between the speed of readout from the CCD chip and the level of noise introduced in the readout process. Thus, the minimisation of the CCD chip readout noise, required to

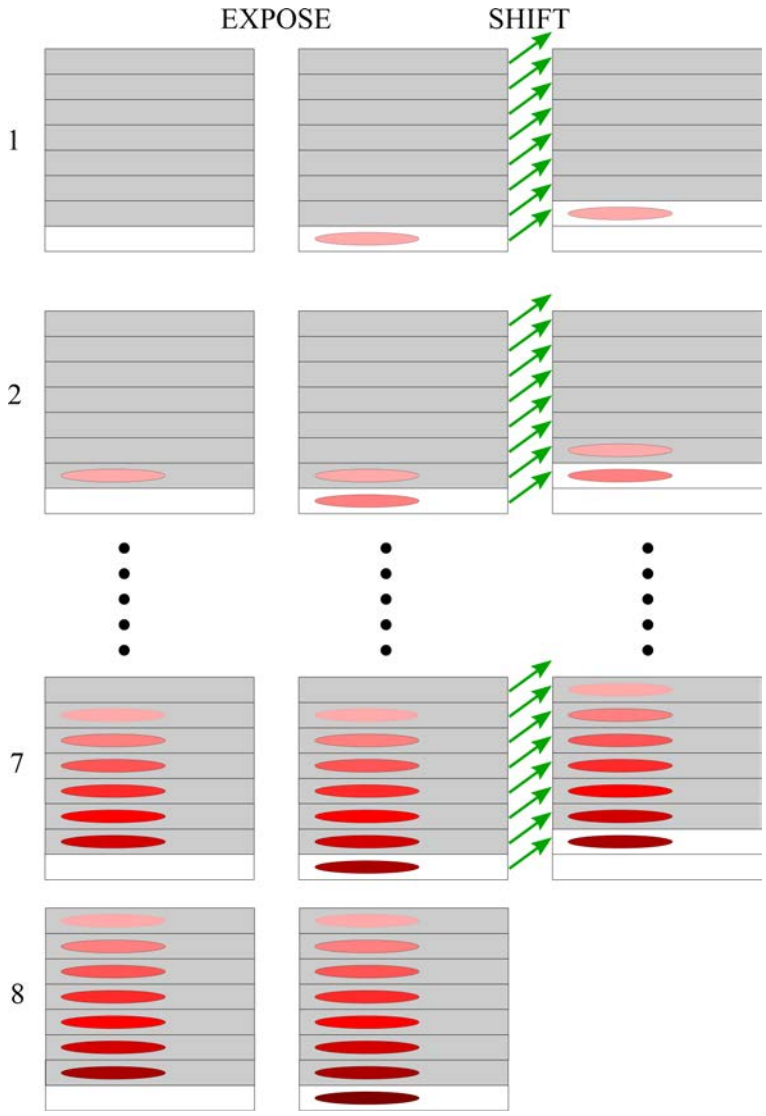

Figure 5.3: The kinetics mode of the PIXIS camera. The first column shows a schematic of the data on the CCD chip before each slice is exposed, the second shows the data on the CCD chip after the exposure, and the third graph shows the data after the shift. The first, second, seventh and eighth exposures are shown for a frame containing 8 slices. Each image is shown in red, with the lightest shade depicting the first image to be exposed, and the darkest the last.

minimise the measurement noise, increases the readout time. Additionally, the majority of cameras including the PIXIS camera have a slow shutter speed, taking around 8 ms to open or to close. Together the readout time and shutter speed create an upper limit to the image repetition rate. This repetition rate limit means that any noise measurement is limited by the classical noise.

The slow frame repetition rate can be overcome by using a camera with a "kinetics" mode. In "kinetics" mode only a small region of the CCD chip, called here a slice, is used. After each exposure the camera

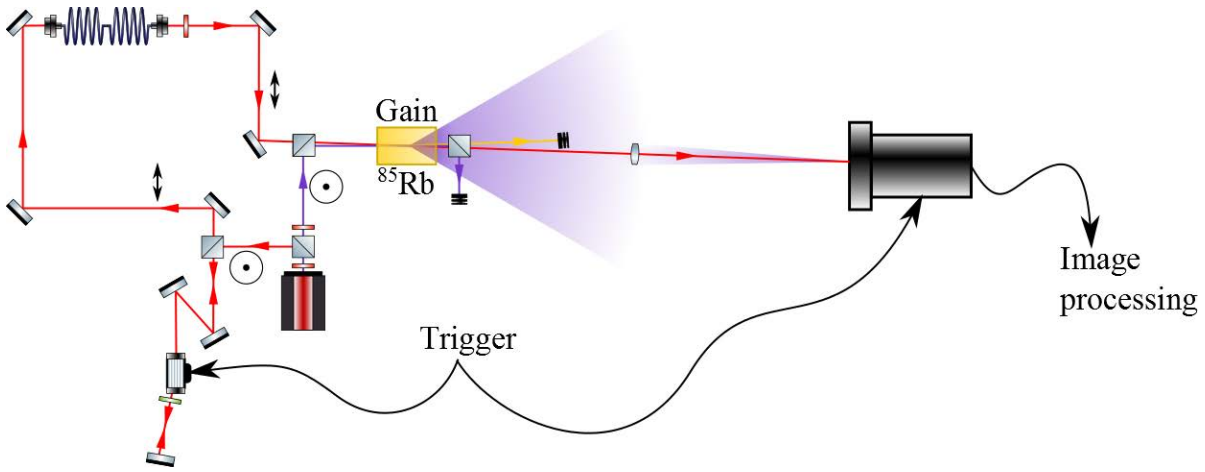

Figure 5.4: The use of the camera to image a light field generated in the 4WM process. The red line is the probe field. The yellow line is the conjugate field, which is ignored at present. The purple line is the pump field, and the purple cones represent the scattered pump light. Here the near field is imaged onto the camera, with an imaging system represented by a single lens.

shifts data up the CCD chip. This prepares the same region of the chip for subsequent exposures without superimposing over the original picture. Thus, multiple slices can be taken in each readout cycle. The size of the slices can be chosen in the camera control. Each full CCD readout cycle is referred to as a frame. The operation of this mode is shown in figure 5.3. Using this mode allows a much faster slice repetition rate than either the readout speed or the shutter speed would allow.

With CCD technology there is no way to electronically mask a region of the chip. This means that at all times, when the shutter is open, the whole frame is reading photons, even during the shifting process. Thus, to use this mode effectively, the bright field incident on the chip must be pulsed such that there is no incident signal whilst the camera is shifting data. This is achieved by using an AOM in the present experiment.

5.2.3 Pump light contamination

The 4WM gain process requires a strong pump field to be used. In order to achieve optimum gain, this pump field must propagate at only a small angle to the signal field. In the earlier experiments in this thesis, the pump field has been removed using polarisation selection. Even so, it can be seen that a small amount of pump light still reaches the detection stage (figure 4.11(b)). A large pump leakage can significantly reduce the measurable level of squeezing. To include the pump field effects but keep the simplest possible setup, we can return to the 4WM system, and only investigate the seeded probe field, as shown in figure 5.4. Since we are interested in the near field we also need an imaging system, here this is represented by a single lens.

When the laser frequency is tuned to the 4WM resonance, the pump field is tuned close to a rubidium transition. This means that the pump field produces a significant amount of scattered light, represented in figure 5.4 by a purple cone. However, the optics are required to be large in order to gather the full RGR. If the optics are small, then they act as a spatial filter, removing high spatial frequencies, and making the fluctuations impossible to measure at these larger spatial frequencies. This forms a cone of emission, limited in part due to the size of the optics used. When the near field in the cell is imaged on the camera, so is the scattered pump light. This leaves a relatively intense region of pump light, centred entirely around the investigated seed field. This pump noise is further increased from scattering off the glass walls of the vapour cell and vacuum chamber.

The noise from the pump leakage light can be made insignificant by increasing the power of the bright signal field relative to that of the pump field. In the case of balanced homodyne detection with photodetectors, this was easily achieved, due to the relatively high saturation threshold of the photodetector. However, each pixel in the CCD chip has a significantly lower saturation limit, which limits the incident bright signal power per pixel to a relatively low power.

This limit can be addressed by expanding the signal over a large number of pixels. The expansion reduces both the leaked pump power and the bright signal power incident on each pixel. The signal power can then be increased, such that the new signal power per pixel is once again close to the saturation threshold. The overall result is an increase in the relative intensity of the signal to pump. Thus, the noise resulting from pump contamination is minimised by expanding the signal field in all directions.

As explained in the previous section, the camera operates in "kinetics" mode for the best results. As such, the area available for each slice is reduced in the vertical direction. Thus, the natural shape available for the each image slice has a large aspect ratio. To accommodate this, the bright signal field should be expanded in the horizontal direction much more than the vertical. This requires the use of a pair of cylindrical lens imaging systems, one for the horizontal and one for the vertical. These imaging systems, and the resulting images are shown in figure 5.5.

Since we want to measure the fluctuations in the near-field, located within the 4WM cell, it is necessary to image the near field on the camera. The imaging systems shown in figure 5.5 are designed to achieve this both in the horizontal and vertical axes. In addition the cylindrical lenses are kept large, such that they do not act as spatial filters.

As already discussed, it is important that the images are close together, and that the pump light is very weak compared to the signal light. A further method to help meet both of these requirements is to reduce the

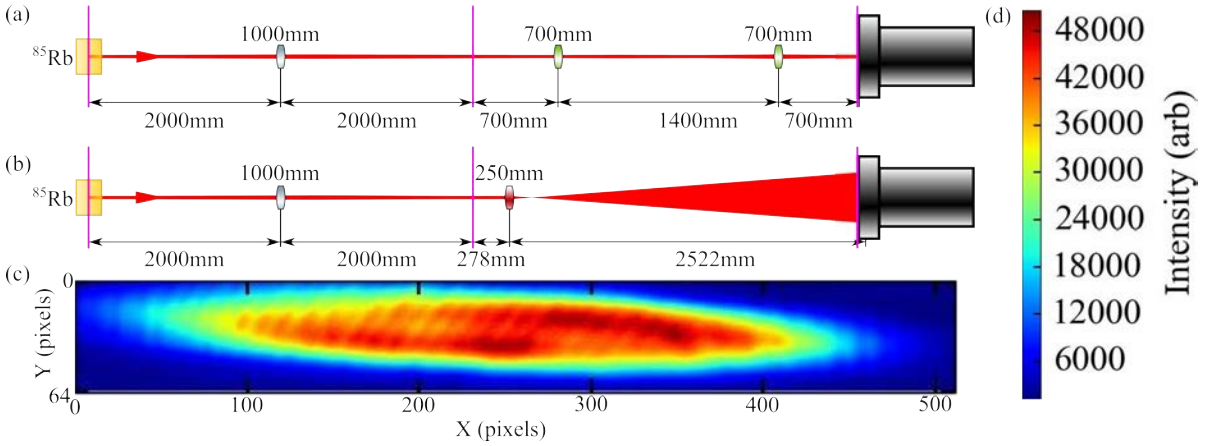

Figure 5.5: The imaging system for the camera. (a) Shows the imaging system, including vertically focussing cylindrical lenses, and how the beam size changes in the vertical direction, (b) shows the imaging system, including horizontally focussing cylindrical lenses, and how the beam size changes in the vertical direction. (c) Shows the final beam shape, with the colour scale given in (d). The magenta lines show the object and image planes.

exposure time. This will reduce the amount of pump light. The bright signal power can again be increased to compensate the loss of light to the signal field. In the current arrangement the exposure time is set to 1 μs. A total of 16 slices are taken for each frame, which results in slice dimensions of 1024×64 pixels. The shift time required to move the images up the CCD chip between each exposure is 210 μs.

It is legitimate to consider whether the pump can be frequency filtered, to reduce the power incident on the camera, or pulsed, to reduce the time that it is incident on the camera. Filtering of the pump is difficult, due to its proximity to the probe and conjugate frequencies, and applying a filter to remove the pump frequency, but not the probe or conjugate, is not practical. The pump has a high power, and as such any pulsing method must be able to handle this large power. In order to achieve the fast switching speeds required, an AOM would be used, and this switching AOM must be able to support the high pump power. Furthermore, the 4WM process requires some initial pumping of the rubidium before the 4WM can occur. Due to the short lifetime of the upper state (approximately 25 ns [123]) this process should be relatively quick. Thus, some improvement should be achievable using pump pulsing, however, this has not yet been implemented. Thus the ratio of exposure time to shift time results in a significantly longer pump exposure compared to the signal exposure. This still results in some significant pump leakage. The Glan-Thompson polarisers caused a significant amount of scattered light when used on the pump beams at approximately 1 W. To reduce this, the pump light must first be spatially separated from the bright signal field, physically blocked, and finally the polariser only used on the remaining light, caused by the scattering of the pump

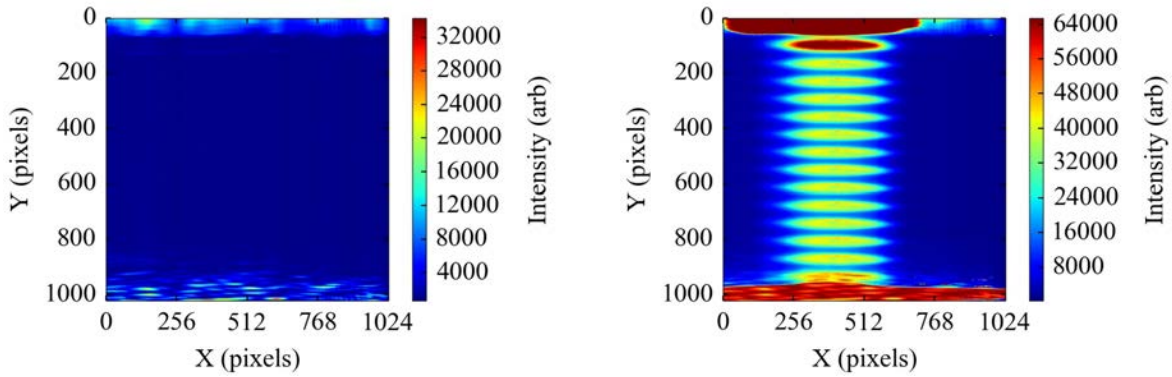

(a) A frame with only the pump beam leakage light incident on the camera.

(b) A frame with the signal light incident on the camera.

Figure 5.6: Some typical frames taken from the camera, with 16 slices, 12 of which are usable.

light. This allows the pump noise to be reduced to a level shown in figure 5.6(a), with 16 slices and the exposure time set to 1 μs, and the shift taking 210 μs per exposure. The image, and that with the signal field in figure 5.6(b), are is the average of the 200 frames that would be used for noise analysis in a single data run. The centre of the field is deliberately located off centre in each slice. This allows for the right hand side of the image to be used to measure the background light reaching each image, as shown in figure 5.3.

5.2.4 Shutter control timing

As can be seen in figure 5.6 the first and last two slices in each frame are overexposed. The slices are synchronised to expose when the AOM pulses from a trigger input to the camera. The shutter speed (8 ms) corresponds to the time taken for 38 AOM pulses (each of 211 μs). Thus, the first and last slices in the frame are always overexposed, from imaging 38 pulses instead of the usual single pulse. The penultimate slice is harmed by the leakage from the final slice, both from the signal field, and from the remaining pump light that bleeds across the final slice during its long exposure. The shutter time does not take exactly the same time on each run. On occasion this can lead to the second slice containing two AOM pulses, instead of the desired single pulse. Hence the increased brightness of this slice in figure 5.6(b).

These problems can be resolved with a better timing sequence as shown in figure 5.7. The top panel shows the speed of the camera shutter, and the middle panel shows a continually repeated trigger signal controlling the AOM and camera exposures. The bottom panel shows the improved trigger signal. In this improved trigger sequence the first trigger pulse tells the camera to start the exposure of each slice. In reality this corresponds to telling the camera to open the shutter. The subsequent 15 pulses are those required to expose

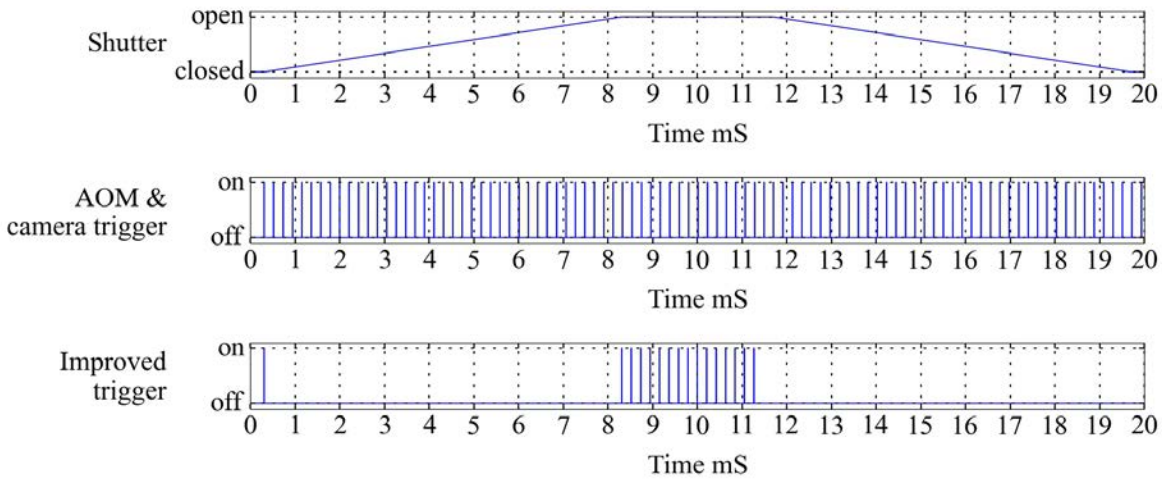

Figure 5.7: A schematic of the control signals for the camera. The camera shutter and the trigger signal, used for both camera and AOM, are shown. The bottom panel shows the form of an improved trigger control sequence to remove the effect of overexposure of the first and last images.

the remaining slices. The delay between the first and second trigger pulse allows the camera shutter sufficient time to open before continuing. This delay removes the over exposed first image, and the timing issues with the second image. The AOM will then stop pulsing after the final image, which will remove the excess signal field from the final overexposed image. However, the extra pump light and noise will still remain present in these final 2 images since the pump is not separately pulsed. Furthermore a physical block could be placed directly in front of the CCD chip, such that only the desired region of the chip can be exposed at any one time.

The modified trigger sequence was due to be controlled by an FPGA. After the shutter closes at the end of each frame the FPGA would wait for a signal from the camera to say that the readout process has finished. Once this signal is received the FPGA would start the sequence for the acquisition of the next frame. Unfortunately the use of the FPGA has not been simple, and has not yet been implemented due to the requirements of matching the FPGA output signal to the required camera input trigger.

5.3 Image processing and noise analysis

Previously, in the frequency domain, a spectrum analyser was used to measure the noise of the light. The equivalent for a series of images taken with a camera is an analysis process. The spectrum analyser calculates the fluctuations on the total intensity of the field over time. To perform exactly the same calculation, with image analysis, the sum of all pixel values can be taken. This gives the total intensity of the field and the

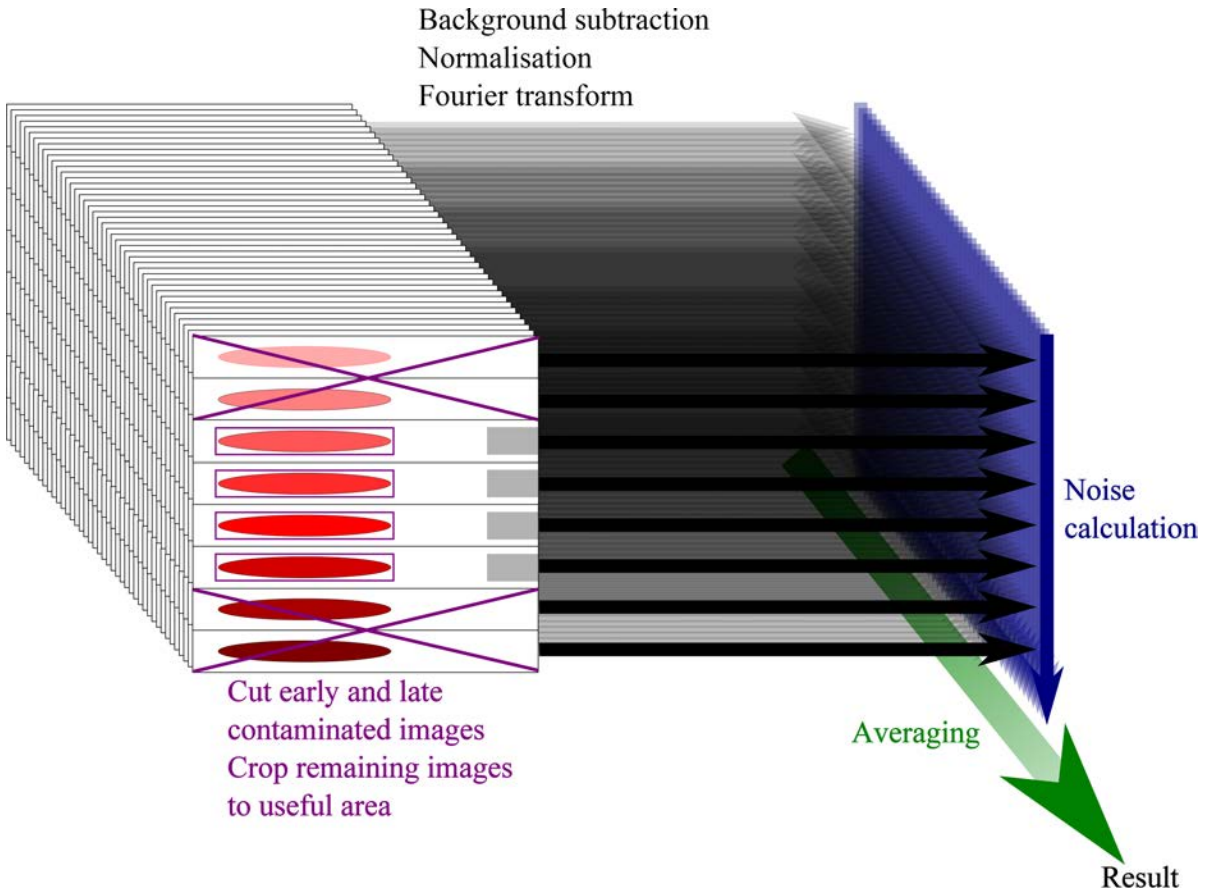

Figure 5.8: The image analysis process. In this case only 8 slices are shown in each frame. In all the experiments 16 slices have been used, with the first pair and the last pair being cut due to contamination. The small grey areas in the images are the areas used to calculate the background for subtraction.

variance of this total intensity is the equivalent of the noise measured with the spectrum analyser. However the measurements of this mode in the time domain are strongly restricted by technical noise. The image analysis can be improved by making use of the spatial information provided by the many pixels on the camera. The Fourier spectrum of the images can be taken, as a decomposition of harmonic waves, and the noise can be computed at all spatial frequencies. This gives an analysis of the spatial character of the noise of the light field.

The full analysis process is more complicated, and is shown in schematic form in figure 5.8. Each frame must be prepared; the first pair and last pair of slices are cut, due to the over exposure in these images (see figure 5.6(b)). Each usable slice is then cropped into an area around the centre of the signal field. Usually, a region of 32×512 pixels is used. The background, due to an offset in the digitisation process, must then be removed. The level of this background light is measured for each slice by taking an unexposed region to

the right hand side of the image, and subtracting the average pixel value within this region from all pixels within the cropped image. The region used for the background calculation is shown in grey in figure 5.8.

After the images are cropped, and the backgrounds removed, they are all normalised to be the same total energy, by equalising the sum of the pixel values in each frame. This is to remove the effects of drifting power in the main laser beam, drifting AOM efficiency, and drifting 4WM gain. After this preparation the fluctuations in the images can finally be analysed. The Fourier transform of each image is then taken, in the x direction, using a fast Fourier transform technique. This results in a series of coefficients defined by

$$A_k(y) = \sum_{x=0}^{n-1} p(x,y)\, e^{-2\pi i \frac{xk}{n}}, \tag{5.1}$$

where n is the number of pixels in the x direction, $p(x,y)$ is the pixel value at position (x,y), and $k \in (0,1,...,n-1)$ is the spatial frequency per pixel. For a given mode the spatial frequency can be converted into units of mm^{-1} using

$$sf = \frac{k}{0.013n}, \tag{5.2}$$

where 0.013 mm is the pixel size. Finally the variance, taken as the sum of the variances of the real and imaginary parts, across the images' Fourier transform coefficients, $A_k(y)$, is taken to calculate the noise, and plotted against their spatial frequency, sf.

The noise can be calculated on a single frame of 16 slices. This provides 12 slices over which to compute the fluctuations. As such, the analysis on a single frame has poor statistics. To improve on the statistics, a number of frames can be taken. However, due to the slow readout of the CCD chip subsequent frames will be subject to some significant delay. This means that between frames classical noise will dominate.

To benefit from the better statistics of a many frame data set, and not be limited by classical noise between frames, the fluctuations can be calculated in a batch process. That is, the fluctuations are calculated between the slices in a frame, for many frames. This process is similar to the effect of the video bandwidth on a spectrum analyser, where the video bandwidth sets the number of samples over which the spectrum analyser will average the signal. These fluctuations, across each frame, can then be averaged over a number of frames, to take advantage of the better statistics. To further improve the statistics, instead of only computing the noise in a frame by taking fluctuations of the whole slice, $\sum_y A_k(y)$, the noise can be calculated separately for each row in the slices, $A_k(y)$. This results in better statistics, and thus better results. The variation in fluctuations across the frames allows for an error on the measured noise to be calculated. It should be noted that a single row in the y direction will be smaller than the coherence length, and as such it will be

impossible to measure squeezing with sampling each row separately.

The resulting fluctuations must then be compared to the SN, in order to extract any QNR. The SN is calculated from the total energy collected in each image. It is white noise, and, as such, is at the same level for all spatial frequencies. Since noise powers are considered here, the SN is equal to this total energy in each image. In the case of balanced homodyne detection, a direct measurement of the QNL, with any given LO, was taken. In the case of the camera, the SN is an absolute calibration, taken by calculating the total intensity of the prepared images, and using this to calculate the QNL. This form of absolute calibration does not account for any technical noise offsets caused by the measurement technique. This is because the technical noise will be measured in the signal data, but not included in the calibration calculation.

These calculations in principal will calculate the fluctuations that occur on any time scale. However, in practice, each slice is exposed to the field for 1 μs, and as such any fluctuations faster 1 MHz will be averaged out. Similarly, a whole frame, including shifting processes, takes 3.166 ms to gather the information. Due to the discarding of the first and last pairs of slices, this reduces to 2.322 ms. As such any fluctuations slower than 430 Hz will equally not be measured.

5.4 Analysis of a laser field

In the previous section I explained an image analysis process, whereby the fluctuations across a series of images can be calculated, in many spatial modes. This analysis technique allows the noise of a laser field to be analysed in the time domain, using a camera. Furthermore, this technique allows the spatial nature of the noise on field to be analysed.

If the camera and image analysis is to be used to measure QNR on a light field, it must first be shown that the technique can indeed measure noise on the light field at the QNL. The simplest demonstration of the use of this noise analysis technique, to measure noise at the QNL, is to measure the noise of a field directly produced from a laser. An ideal single-mode laser would produce a perfect coherent state, entirely within a single spatial mode, and all surrounding modes would be in the vacuum state. In this case, the spatial spectrum should be at the QNL at all spatial frequencies. In any realistic experiment, there will be some classical technical noise on any laser field, introduced through the detection with the camera. In addition, the camera will have an imperfect quantum efficiency, which will introduce further white noise.

To form the series of images of the beam, the laser must be pulsed. The image slices must be triggered to expose whilst the laser field is “on”. In the experiment, this is most easily achieved by passing the laser field through an AOM. The RF drive signal for the AOM can then be switched at the same time as sending

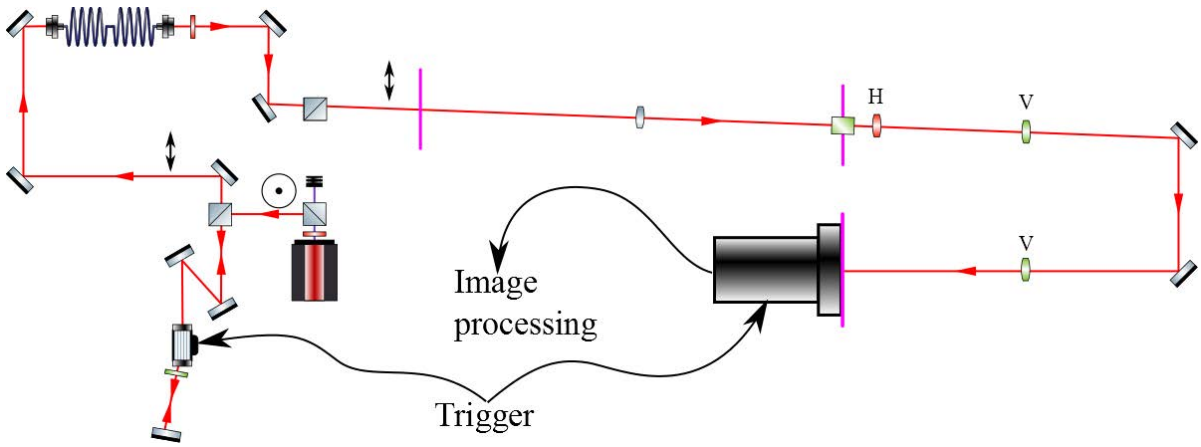

Figure 5.9: The modified setup for the use of the camera to measure the noise of a light field with no gain. The setup is slightly complicated by parts of the system left in place for the 4WM experiments. The lenses are cylindrical and are labelled "H" if they focus in the horizontal direction, and "V" if they focus in the vertical direction.

a trigger signal to the camera, telling it to acquire each slice. The experimental setup used is shown in figure 5.9, and is slightly complicated by the arrangement left in place for future 4WM experiments.

Figure 5.10 shows a typical result after such an experiment imaging the noise on a laser field, using the fast readout mode on the camera. The technical noise is evident at low spatial frequencies, as would be expected, due to each pixel being readout sequential. However, it can also be seen that the noise quickly drops close to the shot noise level, at a spatial frequency of $2 - 3$ mm^{-1}. At very large spatial frequencies the raw data can be seen to drop below the SN level. Clearly this is a measurement error, since the field is a coherent field, and as such cannot exhibit QNR. This effect is explored further in the following section.

5.4.1 Blooming

The drop below SN in figure 5.10 is due to the effect of blooming. This is where the photons received in one quantum well, or pixel, on the CCD chip "blooms" across to the next pixel. This can occur during the image exposure, especially if the pixel wells begin to become saturated. It can also occur during the readout process, due to the incomplete readout of one pixel well leaving some electrons to be added to the value of the next pixel well. In either case, the blooming can be thought of as a blurring effect on the images. The effect of blooming can be shown through using simulated data.

Data at the SN level can be simulated by allowing each pixel, within a given transverse intensity profile, to be a random value following the poissonian distribution. This simulated data is shown in purple in figure 5.11 for an intensity profile taken to be the average profile from the raw data. Here, the sample displays a noise

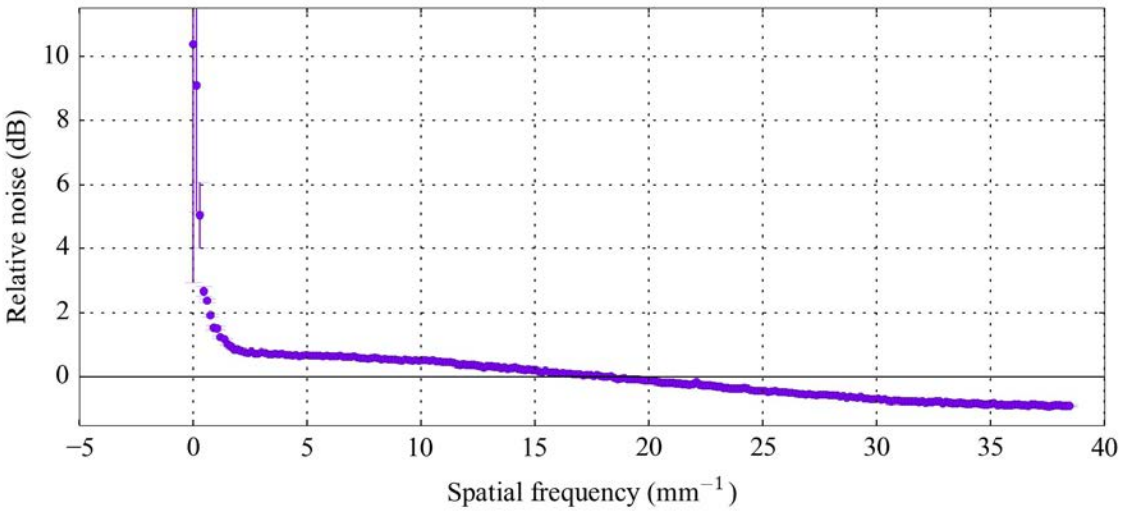

Figure 5.10: The noise extracted from a set of images, plotted against the spatial frequency of that noise. The graph shows the noise dropping down to the SN level at large spatial frequencies. The drop below the SN at extremely large spatial frequencies, and the general shape beyond a spatial frequency of approximately 5 mm^{-1} are due to a measurement error, explored in section 5.4.1.

above the SN due to not subtracting the background before applying the simulated noise. This simulated SN data can be allowed to "bloom", such that any given pixel value, $p(x, y)$, is given by

$$p(x, y) = p(x, y) + b_x \times p(x \pm 1, y) + b_y \times p(x, y \pm 1), \tag{5.3}$$

where $p(x, y)$ is the value of the pixel at position (x, y) and $b_{x,y}$ are the fractions of blooming in the x and y directions. Whilst this transformation does not conserve current, this is unimportant as the data is renormalised as part of the analysis process. If the pixel values are allowed to bloom in the x direction, $b_x > 0$, the noise at low spatial frequencies is increased whilst that at high spatial frequencies it is reduced. An example of this is shown for $b_x = 0.045$ and $b_y = 0$ as the blue data in figure 5.11. This level of blooming corresponds almost exactly to that seen on the raw data, as evidenced by the shape of the noise at large spatial frequencies. Any blooming introduced in the y direction, $b_y > 0$ does not affect the noise calculation, due to the noise only being analysed along the x direction. This can be seen in the yellow and cyan data, where blooming in the y direction of $b_y = 0.045$ is allowed on top of blooming in the x direction of $b_x = 0.045$ and $b_x = 0$ respectively.

The noise measured experimentally can be corrected for this blooming, by appropriately adjusting the

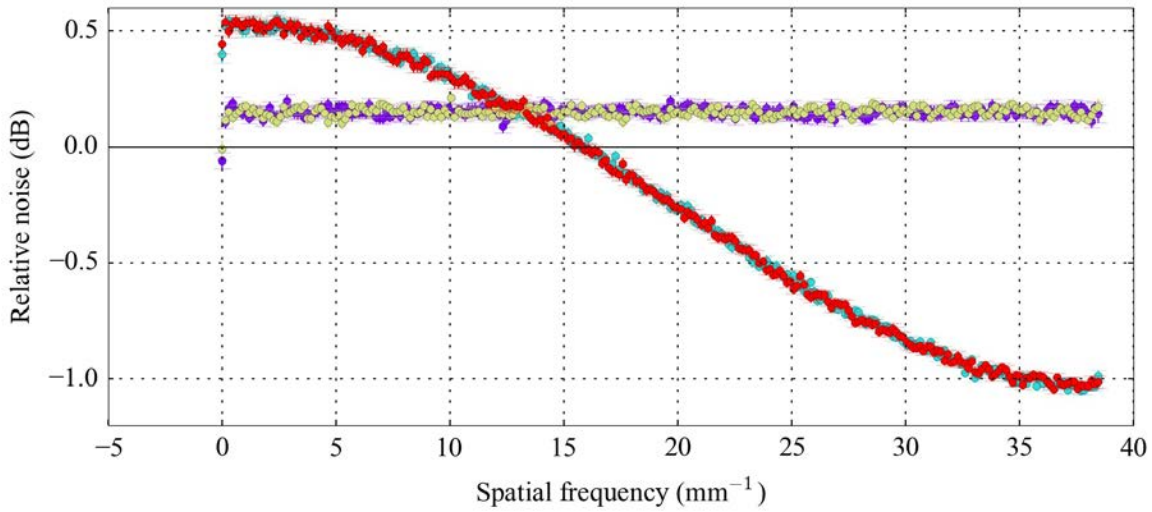

Figure 5.11: The effect of pixel blooming on the simulated data. The purple line is the simulated shot noise data, the yellow is the data with $b_y = 0.045$ and $b_x = 0$, the cyan data is with $b_x = 0.045$ and $b_y = 0$, finally the red data is with $b_x = b_y = 0.045$.

SN noise. This is shown in figure 5.12, where the red data shows the data corrected for the blooming effect. Here, the added (and reduced) noise due to blooming, included in the x direction at 4.5% (the cyan data), is subtracted from the raw data (the purple data). The subtraction is undertaken in Fourier space, with the result being the red data. The data shows that it is possible to image a light field and measure its fluctuations down to levels close to the SN level. This provides promise for the intention of imaging a bright amplitude squeezed light field.

In this case, the blooming arises during the process of reading the data off the CCD chip. As such, if the camera is operated with the slow readout mode, then the effect of the blooming is removed, shown in the yellow data in figure 5.12. The down side of the slow readout mode is simply the long time elapsed for an experimental run, during which time all other parameters must be held constant. It is therefore useful to note that, despite the drop off due to blooming effects at larger frequencies, any additional low frequency noise features can still be seen with the fast readout mode.

5.5 Four-wave mixing spatial bandwidth

The first significant step, in the use of a camera, to measure the QNR of a squeezed light field, is to demonstrate that the quantum noise of a light field can be measured. This was demonstrated in the previous

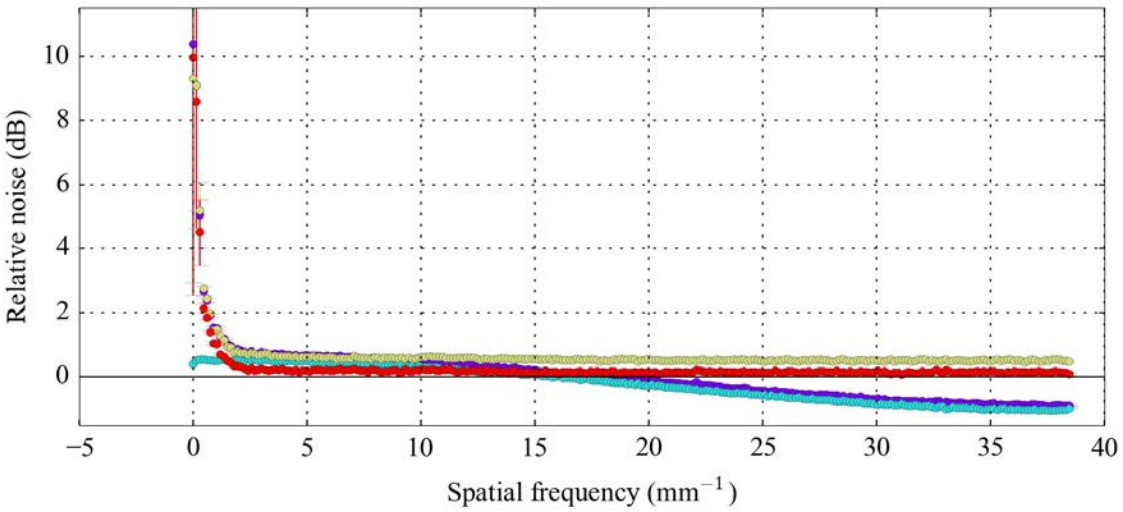

Figure 5.12: The noise extracted from a set of images, plotted against the spatial frequency of that noise. The graph shows the noise dropping down to the SN level at large spatial frequencies. The purple data is raw experimental data, with a fast readout speed. The cyan data is a model system, with the same intensity profile as the experimental data, with 4.5% blooming in the x direction. The red data is the experimental data corrected for this blooming. The yellow data is the raw data with a slow readout speed.

section with measurements made at the SN level. However, it is evident from figure 5.12 that, at low spatial frequencies, the noise is limited by the technical noise. This technical noise presents a lower limit to the spatial frequency where any squeezing will be measurable of aprroximately 0.5 mm^{-1}. Thus, in order to progress to measuring squeezing with such a system, it must be demonstrated that the squeezing spatial bandwidth is larger than this technical noise bandwidth.

Thus, the next step towards measuring squeezing with this method is to ascertain the spatial bandwidth of the squeezing process. In the previous chapter, I demonstrated that the squeezing process has a finite spatial bandwidth through the demonstration that it contains a number of spatial modes. I showed the results of an experiment to measure the coherence area of the squeezed field (figure 4.29). These results show that the coherence length is given by $l_{coh} \approx 0.2$ mm in the near field. The imaging system, from the 4WM cell to the camera, magnifies the near field horizontally by a factor of 4. This means that the coherence length, as imaged on the camera would be 0.8 mm, corresponding to a spatial frequency of approximately 2.5 mm^{-1}, given by $2/l_{coh}$. This value suggests that measuring the squeezing could be possible.

Whilst using the previously measured coherence area provides a good estimate of the squeezing spatial bandwidth, it can also be directly measured. The squeezing spatial bandwidth is defined by the spatial

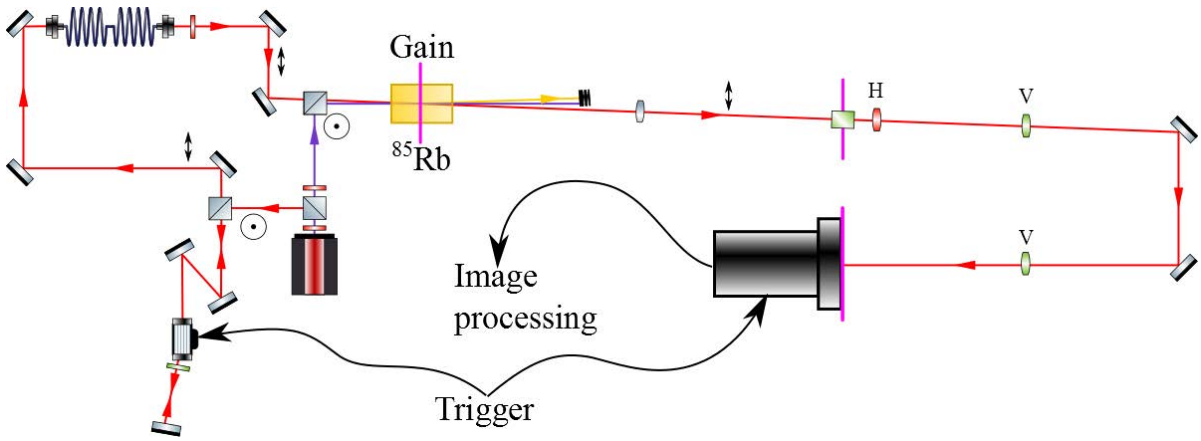

Figure 5.13: The modified use of the camera to image a light field generated in the 4WM process. The red line is light at the probe frequency. The yellow line is light at the conjugate frequency, which is ignored at present. The purple line is pump light. The lenses are cylindrical and are labelled "H" if they focus in the horizontal direction, and "V" if they focus in the vertical direction.

bandwidth of the 4WM gain process. Further, it is well known that a light field cannot be amplified without adding excess noise in the process [135, 136]. This allows the squeezing spatial bandwidth to be directly measured, by measuring the excess noise introduced by 4WM gain. In order to complete this observation, a single bright probe beam is imaged on the camera. The probe passes through the 4WM system on the way to the camera (figure 5.13). A comparison is then made between when the gain is applied to the probe field, and when there is no gain.

The gain can crudely be controlled by removing the 4WM cell, or by blocking the pump field. Both of these methods have the potential to significantly affect the noise results due to reduced scattering of pump light off the glass walls of the 4WM cell. Instead, the gain can be controlled by changing the laser frequency (one-photon detuning) between the 4WM resonance, causing amplification of the seed beam, and a frequency far detuned from the 4WM resonance, where there will be no gain to the seed field. The noise measured in the two cases can be compared. To keep all other external conditions as similar as possible the pump should be present in both cases, and the final probe power should be similar, ie. a lower initial probe power should be used to compensate for the gain.

The results of this preliminary measurement are shown in figure 5.14. The excess noise from gain is measured both at $\delta = 4$ MHz (figure 5.14(a)) and at $\delta = -4$ MHz (figure 5.14(b)). In these measurements the amplified field has a higher noise level than the unamplified field, up to a given spatial frequency. The noise difference between the two measurements is shown in red. These sets of results both show a significant increase in noise when the laser frequency is tuned to resonance, as compared to the far detuned case, at low

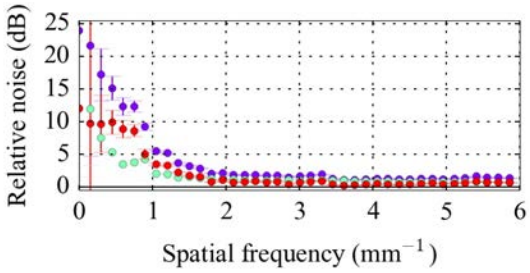

(a) $\delta = 4$ MHz.

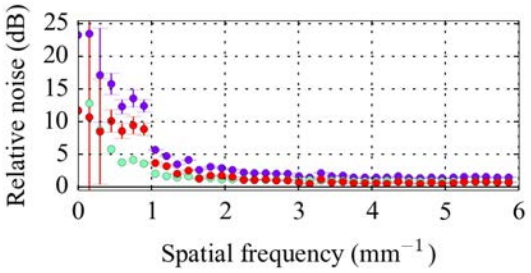

(b) $\delta = -4$ MHz.

Figure 5.14: In both graphs the noise is plotted against the spatial frequency for two cases. The noise is scaled relative to the SN, calculated from the total intensity in each frame. Each graph shows a different two-photon detuning, δ, with a) showing the data taken with $\delta = 4$ MHz, and b) showing the data taken at $\delta = -4$ MHz. The purple data shows the noise when the laser frequency is set such that the system is on 4WM resonance, ie. with gain. In this case the pump power is set to give a gain of 4. The cyan data shows the noise when the laser frequency is far detuned from the 4MW resonance, ie. no gain. The red data shows the difference between these two sets of noise, ie. the excess noise caused by gain.

spatial frequencies.

When $\delta = 4$ MHz the gain in the system was measured to be approximately 5. Using the noise figure, the initial expected excess noise can be calculated to be approximately 9.5 dB [135]. When the two-photon detuning is changed to $\delta = -4$ MHz, the gain is roughly doubled (figure 4.14(b)) and, as such, the expected excess noise would be 12.7 dB. With the lower two-photon detuning, the spatial bandwidth of the 4WM is also expected to be wider, as can be seen from the theory and data in our paper discussing the phase matching condition [124] (also shown in figure 3.4).

The slight increase in spatial bandwidth, with the change from $\delta = 4$ MHz to $\delta = -4$ MHz, suggests that the measured increase in noise may indeed be that caused by the 4WM gain. However, if this were the case, then a significant change in the level of the excess noise might be expected. It is also worth noting that, whilst the gain increases with the change from $\delta = 4$ MHz to $\delta = -4$ MHz, so does the absorption, which will also effect the excess noise.

The increase in noise, between off-resonant and on-resonant, cases may also be due to the change in the scattering rate of the pump in the rubidium vapour, between on resonant and off resonant one-photon detunings. This leads to a change in the pump noise, which can be significant despite all attempts to keep experimental parameters as similar as possible between the gain and no-gain cases. The pump noise is particularly significant because it arises from incoherent fluorescence. Thus, it is super poissonian, and produces a large noise contribution, despite being a very small amount of light. As such, a more detailed investigation needs to be undertaken, and the pump noise needs to be reduced if at all possible.

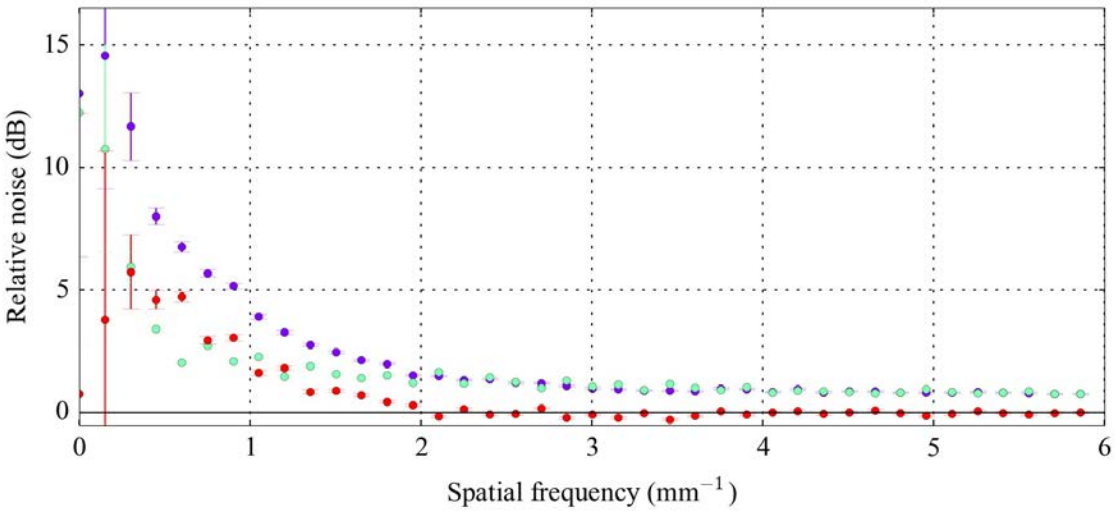

Figure 5.15: The noise is plotted against the spatial frequency for two cases. The purple data shows the noise when the laser frequency is set such that the system is on 4WM resonance, ie. with gain. In this case the pump power is set to give a gain of 5. The cyan data shows the noise when the laser frequency is far detuned from the 4MW resonance, ie. no gain. The red data shows the difference between these two sets of noise, ie. the excess noise caused by gain.

In these measurements, and in the previous chapters in this thesis, including the coherence area measurement, the seed is roughly half the size of the pump beam. If the seed size is increased to a size comparable to the pump beam size within the 4WM cell, roughly doubling its size, then the number of squeezed modes within the bright signal field will be increased. If the expanded seed is then imaged to the same size on the CCD, thus enlarging it only by a factor of 2 horizontally, then the coherence area on the camera would become 0.4 mm. Note that the coherence area is still the same size in the 4WM gain medium, in the near field, and it is just the change in imaging system that changes the imaged size of the coherence area on the CCD camera. As such, the spatial bandwidth of the 4WM gain will be roughly doubled, to 5 mm^{-1}, as measured in the camera image. This broadens the region where any squeezing could be expected to be measured.

With the enlarged seed beam, at the 4WM cell, the post cell imaging system must be changed. It now images the larger seeded area within the 4WM cell on the same area on the CCD chip. Consequently there is a larger region of the pump also imaged onto the same size on the CCD chip, leading to an increase pump noise per pixel. The experiment for measuring excess noise can be repeated as before. The results are shown in figure 5.15, again with a gain of approximately 5. Initially these results seem promising, with

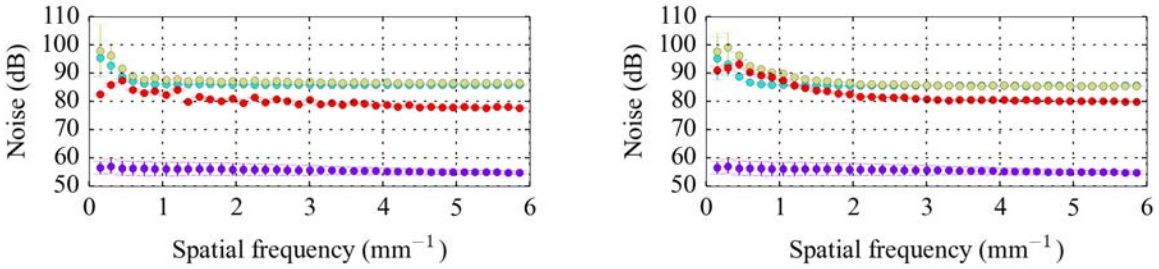

(a) Far detuned from resonance.

(b) On 4WM resonance.

Figure 5.16: The absolute noise, taken as a varience, with an arbitrary offset, arising from different sources. Here the noise is not normalised to the shotnoise of the light. The noise is plotted both in the case of the laser frequency is far detuned from 4WM resonance (a) and when it is tuned to 4WM resonance (b). The purple data is the background noise, taken with the laser beam blocked. The cyan data is noise on the seed field, with the pump field blocked before the 4WM medium. The red data is the pump noise, and the yellow data is the noise with both seed and pump.

some increased noise from the 4WM gain. However, this is less than the 9.5 dB of excess noise that would be expected from a gain of 5.

A closer inspection of the noise sources is preformed by blocking each of the fields in turn. The results (figure 5.16) reveal the effect of the pump noise (red data). In both the detuned case (figure 5.16(a)), and the on-resonance case (figure 5.16(b)), the noise of the seed field, taken with the pump field blocked, is plotted (cyan data) and can be compared to the pump noise, taken when the seed field is blocked, (red data) and the noise measured when both the seed and the scattered pump light are incident on the camera (yellow data). The noise of the seed and scattered pump together is that plotted in figure 5.15. In the ideal case the pump noise would be significantly lower than the other noise sources. For a noiseless amplifier, the noise measured when both the pump and seed are incident in the cell should be the sum of the pump noise and probe noise. However, the 4WM process is not noiseless, but instead introduces excess noise. As such the amplified signal should have significantly larger noise than the unamplified signal. It can be seen that, at low frequencies, in the on-resonance case the pump noise (red data) is larger than the seed noise (cyan data), and as such dominates the measured noise (yellow data). This suggests that at least a reasonable proportion of the increased noise, from the 4WM gain, is in fact due to the increased noise from scattered pump light. As such, more work needs to be done to further reduce the pump noise, before any significant results can be recorded.

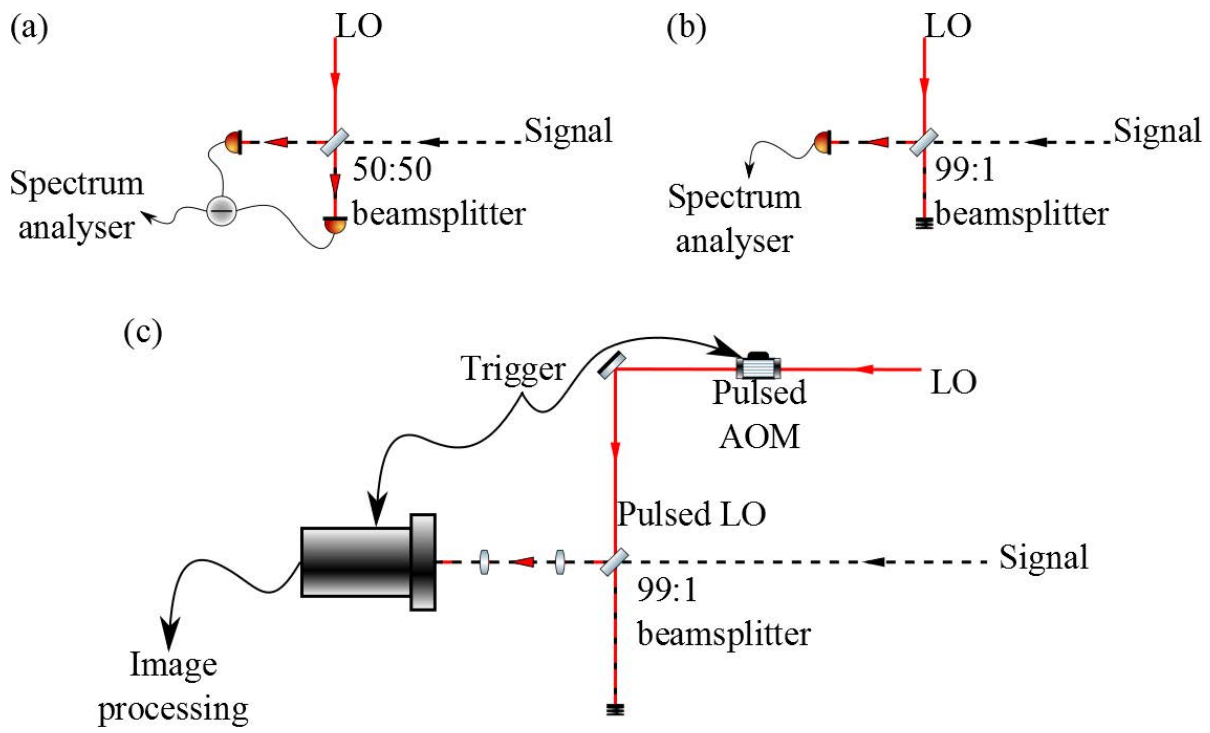

Figure 5.17: The change in detection setup from balanced homodyne detection in (a), through unbalanced homodyne detection using a photodetector in (b), finally to unbalanced homodyne detection in the time domain with a CCD camera in (c). In (c) the LO is pulsed using an AOM, triggered by the same source as the camera slice exposures. When a BLO is used it can be pulsed using the AOM that is used to generate the seed frequency.

5.6 Measuring quantum noise reduction in time domain

The initial testing of the camera revealed that the technical noise drops quickly with increasing spatial frequency. The preliminary results and calculations suggest that this drop-off occurs faster than the drop-off of excess noise from 4WM gain. Fundamentally, the squeezing process and the amplification process are the same. Thus, the spatial bandwidth of the squeezing should be comparable to that of the excess noise from gain. As such, the results of the preliminary experiments are indications that it will be possible to investigate the spatial structure of the squeezed light using this method. The methods presented here should be sufficient for an initial measurement, even so, some further development will be necessary. The most significant work required will be in the further reduction of the pump noise. The biggest change to improve this would be the replacement of the AOM with an AOM that can handle a higher power. This would allow for a much larger seed power, and hence allow for shorter exposure times. Additionally, it may be possible to employ a pumping scheme to reduce the scattering rate of pump light, in the rubidium vapour, and hence reduce the pump noise.

Theoretically, the change from measuring squeezing in the frequency domain to the time domain is relatively simple. A bright quadrature squeezed field is formed by mixing a bright coherent field with a squeezed vacuum field on a beam splitter. In effect, to achieve this, balanced homodyne detector is exchanged for an unbalanced homodyne detector, and the photodetectors are exchanged for a camera. The different measurement systems are shown in figure 5.17, with (a) showing the balanced homodyne detection used in the earlier chapters of this thesis. Figure 5.17(b) shows an unbalanced homodyne method of measuring the noise on a light field, where the 50:50 beam splitter is exchanged for one with a higher transmission. This beam splitter forms a single bright quadrature squeezed field, which is then subsequently detected.

As discussed in section 3.7.1, the beam splitter acts as a source of loss on the squeezing. The higher the transmission of the beam splitter, the more squeezing will be present at the camera, and hence the better the measurement. However, the higher the transmission the lower the reflection must be, and hence the less the squeezed vacuum field will be amplified by the LO. As such, the beam splitter transmission is limited by the input power of the seed light used to generate the BLO through the 4WM process. As explained in section 4.2.2, the BLO power is limited by the seed power that can be obtained with the AOM and fibre system. Ideally, the BLO should be strong enough to employ a 99:1 beam splitter. With such a beam splitter, the squeezed signal is more faithfully transmitted with a 99% transmission, thus, it retains most of its squeezed character. The BLO field is also attenuated to 1% of its original power. This attenuation helps to limit any classical noise on the BLO field, and bring it closer to the QNL.

Figure 5.17(c) shows the unbalanced homodyne detection method with a CCD camera in place of the photodetector. In this case, the near-field bright quadrature squeezed field should be imaged onto the camera. The asymmetric imaging setup should be used as previously explained. To control the exposure on the camera, the LO needs to be pulsed. The pulsing of the LO field is controlled by an AOM. The AOM and camera must be synchronised with a shared trigger, such that the AOM is only "on" when the camera is exposing. In the present experiment, this is achieved using the AOM that shifts the frequency of the seed field to the probe frequency.

In the MSM characterisation of the squeezed field, in the frequency domain (section 4.5), the spatial mode under investigation was defined by the mode of the LO. As such, the method for investigating the MSM character of the squeezed light was to use a small LO, translated to many positions across the squeezed field. In the time domain, using the camera, the noise can be investigated on many different modes within the squeezed field. This means that a single LO field must cover all the transverse spatial modes in the squeezed field. As such, the LO field needs to be expanded to the largest possible mode size, in the near field. This

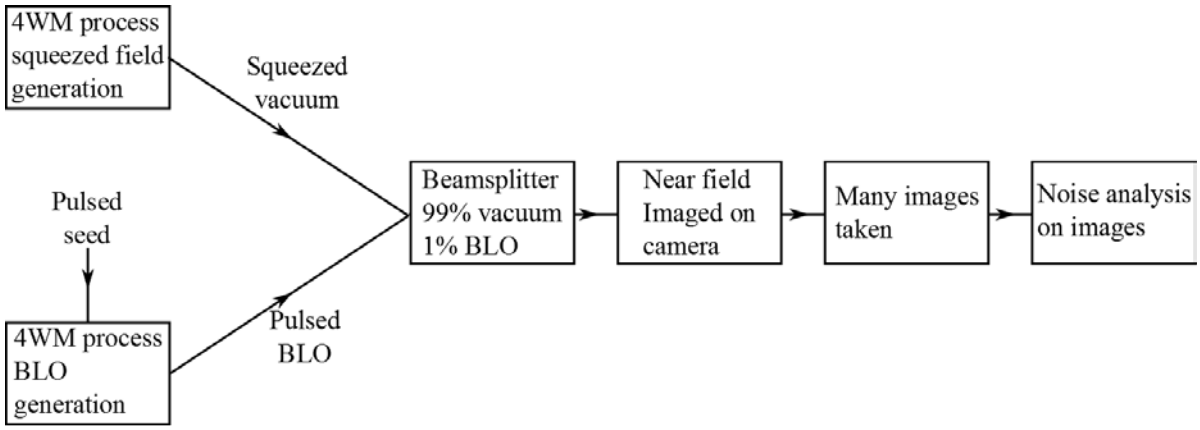

Figure 5.18: The modified block diagram for a squeezing experiment aiming to image the noise of a signal field at the quantum level. The generation of the BLO and signal fields have been contracted, and the detection method using the camera expanded.

has already been completed for the measurements in figure 5.15 and figure 5.16.

The BLO and the signal field can both still be produced using the 4WM process, and aligned using a bichromatic interferometer, as has been done earlier in this thesis (section 4.3). The change of detection will only affect the homodyne detection stage in the block diagram, shown in figure 4.1. The new block diagram with the introduction of the camera is shown figure 5.18. Here, the early stages of BLO production and squeezed vacuum production are simplified, and the detection stage is expanded. The full updated experimental setup, for making QNR measurements with the camera in the time domain, is shown in figure 5.19.

When performing measurements in the frequency domain, it was important to scan the LO phase to measure the full noise ellipse of the squeezed field. The phase relation between the LO and NEP of the squeezed vacuum field is still important when measuring squeezing in the time domain using a camera. In this case, it becomes difficult to scan the LO phase, since each slice must be taken at the same phase. Instead, there are two alternative options. The first is to employ a phase locking technique, whereby the phase of the LO is held constant, with respect to the NEP, such that it always amplifies the squeezed quadrature. The second alternative is to slightly misalign the LO and squeezed field in the vertical direction. This will cause a phase difference gradient to form on the camera, between the LO and the squeezed field. The result will be that different pixel rows on the camera measure different quadratures of the NEP, and hence the squeezing spectrum should be recovered.

These changes to the experimental setup and alignment procedures, to change from measuring in the frequency domain to measuring in the time domain, are complicated and have not yet been fully realised. This is left as future work for the continuing PhD student.

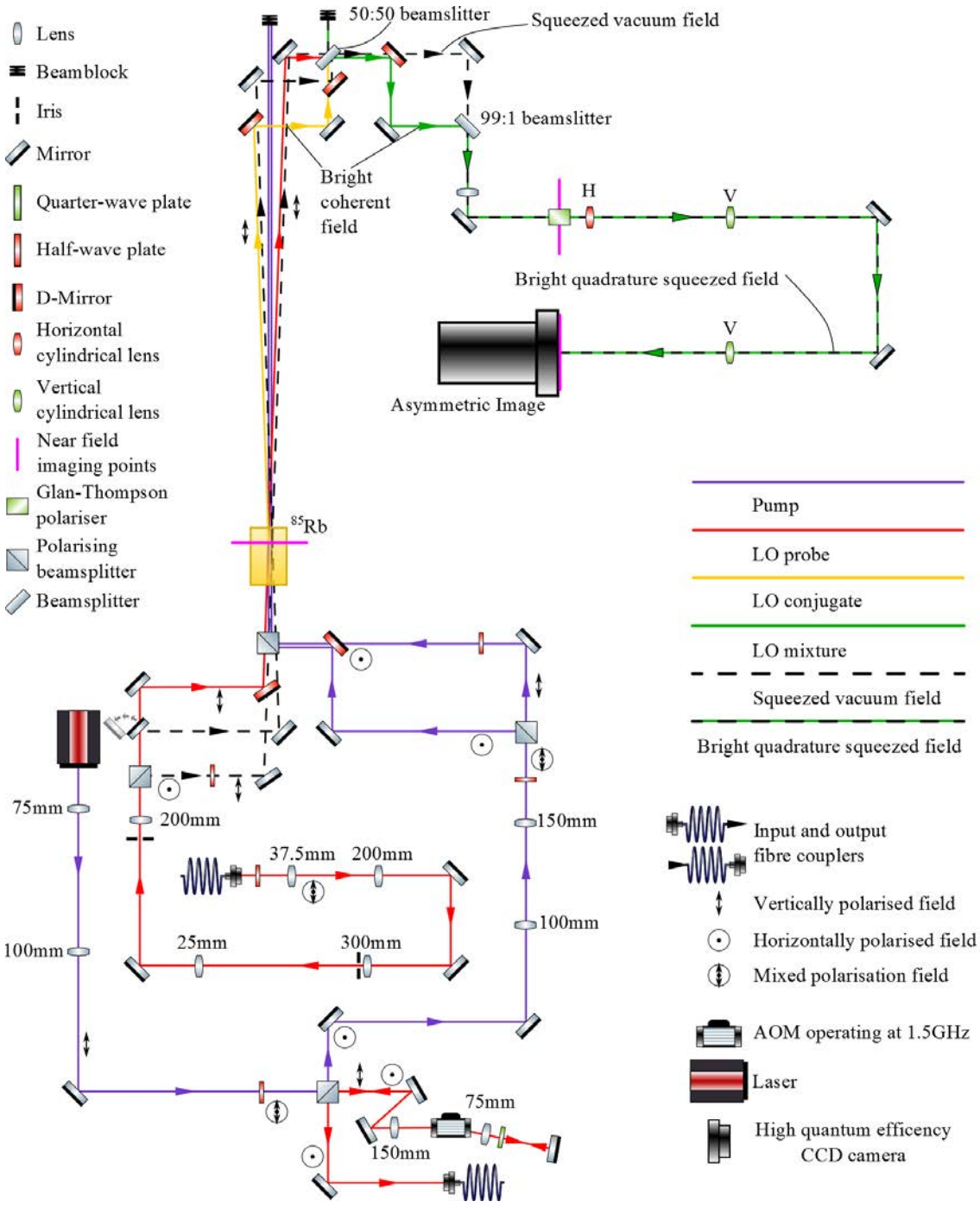

Figure 5.19: The experimental setup, as modified to include the CCD Camera, for the imaging of the QNR. Where, on the diagram, the signal and LO fields are slightly separated, they are split vertically in the experiment.

Ultimately, this work will result in the generation and characterisation, in the time domain, of a bright multi-spatial-mode quadrature squeezed field. Such a field can be used in imaging techniques (see section 2.7.2) to achieve optical measurement accurate beyond the standard quantum limit. The ability to improve the accuracy of such measurements allows a significant improvement of understanding in numerous scientific fields.

CHAPTER 6

CONCLUSION

In this thesis, I have introduced and explained how TMSSs and SMSSs can be generated using amplifiers. I have explained the effect of propagation on the squeezed states, and the methods of converting between the two different types of squeezed state. I have introduced theoretically the use of a bichromatic LO for homodyne detection of squeezed states with distant sidebands, and how such a BLO might be generated. I discussed the use of a 4WM process in hot rubidium vapour to generate squeezed light and have implemented such a source experimentally. I have manipulated the TMSS into a SMSS and have generated and used a BLO to experimentally measure squeezed light produced from this source.

I introduced the concept of using squeezed light for improving the accuracy of an interferometer below the SQL. I discussed the type of squeezed state required to improve the accuracy at both low and high frequencies, and the theoretical state required to increase the accuracy across a broad frequency range. I characterised the frequency dependence of the squeezed state produced using 4WM, and have shown that the amplitude can be squeezed at one frequency, whilst simultaneously the phase is squeezed at a different frequency. I discussed how, with the correct LO phase, the SMSS generated experimentally could be used to increase the accuracy of an interferometer, below the SQL, across a broad frequency range.

I discussed the spatial mode structure of squeezed light, and the difference between a SSM and MSM quadrature squeezed state. I also introduced the limitations of many current implementations of PDC for MSM squeezed light sources, and discussed how 4WM in hot vapours can improve upon these limitations. I investigated the MSM nature of the squeezed light generated through a 4WM gain medium. I directly evidenced the presence of squeezing on multiple independent spatial modes within a single squeezed field. I found there to be 75 separate squeezed spatial modes within the present implementation, significantly improving on previous measurements. I explained how this source differs from previous experimental implementations,

by improving on mode number, and removing restrictions on the mode shape.

I explained the potential use of the MSM squeezed light to improve super-resolution imaging, below the QNL, with a direct illumination method. I discussed how such measurements must be made in the time domain, and introduced the concept of imaging squeezed light. I have investigated the use of a high quantum efficiency, low noise camera, and the use of a "kinetics" mode to investigate the intensity fluctuations within a light field. I have designed and implemented an image analysis technique, equivalent to a spatial spectrum analyser. I have used this image analysis to measure the noise on a sequence of images at the quantum noise level, in the time domain. I have used this technique to investigate the spatial bandwidth of the 4WM process, and hence the potential squeezing bandwidth. I have shown strong indications that this noise analysis is suitable for further use to investigate the MSM quadrature squeezed light in the time domain, and to investigate its spatial nature.

I have discussed the requirements on the phase of the LO and NEP of the squeezed field to measure squeezing in the time domain. I have introduced two potential methods to achieve such a squeezing measurement, namely relative phase locking, and use of a vertical phase gradient. This thesis leaves, as future work, the generation of a bright quadrature squeezed field, and the full characterisation of its spatial properties in the time domain.

Once a bright quadrature squeezed field has been generated and fully characterised this field can be used for direct quantum imaging. The field can be used, along with super-resolution analysis techniques to demonstrate the improved super-resolution beyond the standard quantum limit. Ultimately this bright quadrature squeezed light could improve the accuracy of many multi-spatial-mode optical measurement techniques.

APPENDIX A

DERIVATION OF THE NEP IN TERMS OF THE PHASES OF THE PROBE AND CONJUGATE COMPONENTS

In section 4.4, I investigated the phase delay caused by the 4WM process, and how this changes for the probe and conjugate frequencies with changing two-photon detuning. In order to convert these phase delays, on individual frequencies, into the NEP of the combined squeezed vacuum, we must first derive the relation. Consider a 4WM system that produces entangled operators,

$$\hat{b}_p = U\hat{a}_1 e^{-i\omega_1 t} + V\hat{a}_2^\dagger e^{i\omega_2 t} \tag{A.1}$$

$$\hat{b}_c = U\hat{a}_2 e^{-i\omega_2 t} + V\hat{a}_1^\dagger e^{i\omega_1 t}, \tag{A.2}$$

where $U = \cosh s$ and $V = \sinh s$, and $\omega_1 = \omega_0 - \omega_p$ and $\omega_2 = \omega_0 - \omega_c$ are the probe and conjugate frequencies with respect to the pump frequency. Here $\hat{a}_1$ and $\hat{a}_2$ are vacuum photon annihilation operators, and so are frequency independent. This is exactly that field produced by the TMSS amplifier discussed in 2.4.

If we work in the rotating wave approximation, at the pump frequency, ω_0, we can make use of the conservation of energy required within the 4WM system to know that $\omega_1 = -\omega_2 = \Delta_{sb}$, as in section 3.8. As such, we can re-write the entangled operators as

$$\hat{b}_p = U\hat{a}_1 e^{-i\Delta_{sb} t} + V\hat{a}_2^\dagger e^{-i\Delta_{sb} t} \tag{A.3}$$

$$\hat{b}_c = U\hat{a}_2 e^{i\Delta_{sb} t} + V\hat{a}_1^\dagger e^{i\Delta_{sb} t}. \tag{A.4}$$

Here it is clear the $\hat{b}_p$ is the probe and $\hat{b}_c$ is the conjugate.

When the two-photon detuning in the 4WM system is changed, the probe and conjugate experience different phase delays given by θ_p and θ_c respectively. As such when these phase delays are introduced the

entangled operators become described by

$$\hat{b}_p = U\hat{a}_1 e^{-i\Delta_{sb}t+i\theta_p} + V\hat{a}_2^\dagger e^{-i\Delta_{sb}t+i\theta_p} \tag{A.5}$$

$$\hat{b}_c = U\hat{a}_2 e^{i\Delta_{sb}t+i\theta_c} + V\hat{a}_1^\dagger e^{i\Delta_{sb}t+i\theta_c}. \tag{A.6}$$

These fields are then interfered on a beam splitter to produce a squeezed field given by

$$\hat{a}_{squ} = \frac{Ue^{-i\Delta_{sb}t+i\phi_p}\hat{a}_1 + Ve^{-i\Delta_{sb}t+i\phi_p}\hat{a}_2^\dagger + Ue^{i\Delta_{sb}t+i\phi_c}\hat{a}_2 + Ve^{i\Delta_{sb}+i\phi_c}\hat{a}_1^\dagger}{\sqrt{2}}, \tag{A.7}$$

where it is assumed that the phase delay introduced from different path lengths of the entangled fields is zero, as is ensured by the alignment in section 4.2.4.

To investigate this squeezed field a BLO is required that, in the case of this experiment, is generated by a second similar 4WM system. The BLO would have the form

$$\hat{a}_{BLO} = \frac{\hat{a}_{bp}e^{-i\Delta_{sb}t} + \hat{a}_{bc}e^{i\Delta_{sb}t}}{\sqrt{2}}, \tag{A.8}$$

where $\hat{a}_{bp}$ and $\hat{a}_{bc}$ are the annihilation operators for bright probe and conjugate fields, with expectation values $\langle\hat{a}_{bp}\rangle = \beta e^{i\phi_p}$ and $\langle\hat{a}_{bc}\rangle = \beta e^{i\phi_c}$. When such a BLO is used to measure this squeezed field, in a homodyne detection scheme, the detection operators, at each of the two photodetectors, will be given by

$$\hat{E}d_1 = \frac{\hat{a}_{BLO} + \hat{a}_{squ}}{\sqrt{2}} \tag{A.9}$$

$$\hat{E}d_2 = \frac{\hat{a}_{BLO} - \hat{a}_{squ}}{\sqrt{2}}, \tag{A.10}$$

as in section 3.7.3.

The subtracted signal from the homodyne detector will be given by $\hat{i} = \hat{E}d_1^\dagger\hat{E}d_1 - \hat{E}d_2^\dagger\hat{E}d_2$, with fluctuations given by

$$\left\langle\Delta\hat{i}\right\rangle = \beta^2 e^{2s}\cos^2\left(\frac{\phi_p + \phi_c - \theta_p + \theta_c}{2}\right) + \beta^2 e^{-2s}\sin^2\left(\frac{\phi_p + \phi_c - \theta_p + \theta_c}{2}\right). \tag{A.11}$$

This can be re-written with a single phase for the BLO and a phase of the NEP of the squeezed vacuum field as

$$\langle\Delta i\rangle = \beta^2 e^{2s}\cos^2(\phi - \theta) + \beta^2 e^{-2s}\sin^2(\phi - \theta). \tag{A.12}$$

Thus the overall phase of the BLO is given by $\phi = \frac{\phi_p + \phi_c}{2}$, and more importantly the NEP of the squeezed vacuum field is given by $\theta_{NEP} = \frac{\phi_p + \phi_c}{2}$. As such we can convert the phase delay of the two frequency components of the squeezed vacuum into the phase delay of the NEP by taking their average.

It is also worth noting that the phases of the BLO and NEP in equation (A.12) are always subtracted. These means that any phase delay change common to the BLO and NEP, such as changing the two-photon detuning in the 4WM system, is cancelled. This is indeed the reason that the phase of the BLO tracks the phase of the NEP, as found in section 4.4.2.

LIST OF REFERENCES

[1] J. Kitching, S. Knappe, and E.A. Donley. Atomic Sensors #x2013; A Review. *IEEE Sensors Journal*, 11(9):1749–1758, September 2011.

[2] J. Vanier. Atomic clocks based on coherent population trapping: a review. *Appl. Phys. B*, 81(4):421–442, July 2005.

[3] S. Bize, P. Laurent, M. Abgrall, H. Marion, I. Maksimovic, L. Cacciapuoti, J. Grünert, C. Vian, F. Pereira dos Santos, P. Rosenbusch, P. Lemonde, G. Santarelli, P. Wolf, A. Clairon, A. Luiten, M. Tobar, and C. Salomon. Cold atom clocks and applications. *J. Phys. B: At. Mol. Opt. Phys.*, 38(9):S449, May 2005.

[4] N. Poli, C. W. Oates, P. Gill, and G. M. Tino. Optical atomic clocks. *arXiv:1401.2378 [physics]*, January 2014. arXiv: 1401.2378.

[5] M. de Angelis, A. Bertoldi, L. Cacciapuoti, A. Giorgini, G. Lamporesi, M. Prevedelli, G. Saccorotti, F. Sorrentino, and G. M. Tino. Precision gravimetry with atomic sensors. *Meas. Sci. Technol.*, 20(2):022001, February 2009.

[6] A. Pace, M. Collett, and D. Walls. Quantum limits in interferometric detection of gravitational radiation. *Phys. Rev. A*, 47(4):3173–3189, April 1993.

[7] Harry Collins. *Gravity's Shadow: The Search for Gravitational Waves*. University of Chicago Press, Chicago, 2nd edition edition, October 2004.

[8] H. Grote, K. Danzmann, K. L. Dooley, R. Schnabel, J. Slutsky, and H. Vahlbruch. First Long-Term Application of Squeezed States of Light in a Gravitational-Wave Observatory. *Phys. Rev. Lett.*, 110(18):181101, May 2013.

[9] S. S. Y. Chua, B. J. J. Slagmolen, D. A. Shaddock, and D. E. McClelland. Quantum squeezed light in gravitational-wave detectors. *Class. Quantum Grav.*, 31(18):183001, September 2014.

[10] Mark Bates, Bo Huang, Graham T. Dempsey, and Xiaowei Zhuang. Multicolor Super-Resolution Imaging with Photo-Switchable Fluorescent Probes. *Science*, 317(5845):1749–1753, September 2007.

[11] Bo Huang, Wenqin Wang, Mark Bates, and Xiaowei Zhuang. Three-Dimensional Super-Resolution Imaging by Stochastic Optical Reconstruction Microscopy. *Science*, 319(5864):810–813, February 2008.

[12] Waseem S. Bakr, Jonathon I. Gillen, Amy Peng, Simon Fölling, and Markus Greiner. A quantum gas microscope for detecting single atoms in a Hubbard-regime optical lattice. *Nature*, 462(7269):74–77, November 2009.

[13] Bo Huang, Hazen Babcock, and Xiaowei Zhuang. Breaking the Diffraction Barrier: Super-Resolution Imaging of Cells. *Cell*, 143(7):1047–1058, December 2010.

[14] Jacob F. Sherson, Christof Weitenberg, Manuel Endres, Marc Cheneau, Immanuel Bloch, and Stefan Kuhr. Single-atom-resolved fluorescence imaging of an atomic Mott insulator. *Nature*, 467(7311):68–72, September 2010.

[15] Jonathan Simon, Waseem S. Bakr, Ruichao Ma, M. Eric Tai, Philipp M. Preiss, and Markus Greiner. Quantum simulation of antiferromagnetic spin chains in an optical lattice. *Nature*, 472(7343):307–312, April 2011.

[16] Marek Piliarik and Vahid Sandoghdar. Direct optical sensing of single unlabelled proteins and super-resolution imaging of their binding sites. *Nat Commun*, 5, July 2014.

[17] Richard Van Noorden. Nobel for microscopy that reveals inner world of cells. *Nature*, 514(7522):286–286, October 2014.

[18] W. Heisenberg. Über den anschaulichen Inhalt der quantentheoretischen Kinematik und Mechanik. *Z. Physik*, 43(3-4):172–198, March 1927.

[19] E. H. Kennard. Zur Quantenmechanik einfacher Bewegungstypen. *Z. Physik*, 44(4-5):326–352, April 1927.

[20] Prof B. H. Bransden and Prof C. J. Joachain. Chapter 5.4. In *Quantum Mechanics*, pages 210–216. Prentice Hall, Harlow, England ; New York, 2 edition edition, January 2000.

[21] Vittorio Giovannetti, Seth Lloyd, and Lorenzo Maccone. Quantum-Enhanced Measurements: Beating the Standard Quantum Limit. *Science*, 306(5700):1330–1336, November 2004.

[22] Rodney Loudon. *The Quantum Theory of Light*. OUP Oxford, Oxford ; New York, 3 edition edition, September 2000.

[23] H. J. Kimble and L. Mandel. Theory of resonance fluorescence. *Phys. Rev. A*, 13(6):2123–2144, June 1976.

[24] H. J. Carmichael and D. F. Walls. A quantum-mechanical master equation treatment of the dynamical Stark effect. *J. Phys. B: At. Mol. Phys.*, 9(8):1199, June 1976.

[25] H. J. Kimble, M. Dagenais, and L. Mandel. Photon Antibunching in Resonance Fluorescence. *Phys. Rev. Lett.*, 39(11):691–695, September 1977.

[26] M. D. Reid, D. F. Walls, and B. J. Dalton. Squeezing of Quantum Fluctuations via Atomic Coherence Effects. *Phys. Rev. Lett.*, 55(12):1288–1290, September 1985.

[27] R. E. Slusher, L. W. Hollberg, B. Yurke, J. C. Mertz, and J. F. Valley. Observation of Squeezed States Generated by Four-Wave Mixing in an Optical Cavity. *Phys. Rev. Lett.*, 55(22):2409–2412, November 1985.

[28] Mari W. Maeda, Prem Kumar, and Jeffrey H. Shapiro. Observation of squeezed noise produced by forward four-wave mixing in sodium vapor. *Opt. Lett.*, 12(3):161–163, March 1987.

[29] M. G. Raizen, L. A. Orozco, Min Xiao, T. L. Boyd, and H. J. Kimble. Squeezed-state generation by the normal modes of a coupled system. *Phys. Rev. Lett.*, 59(2):198–201, July 1987.

[30] Ling-An Wu, H. J. Kimble, J. L. Hall, and Huifa Wu. Generation of Squeezed States by Parametric Down Conversion. *Phys. Rev. Lett.*, 57(20):2520–2523, November 1986.

[31] Tobias Eberle, Sebastian Steinlechner, Jöran Bauchrowitz, Vitus Händchen, Henning Vahlbruch, Moritz Mehmet, Helge Müller-Ebhardt, and Roman Schnabel. Quantum Enhancement of the Zero-Area Sagnac Interferometer Topology for Gravitational Wave Detection. *Phys. Rev. Lett.*, 104(25):251102, June 2010.

[32] Moritz Mehmet, Stefan Ast, Tobias Eberle, Sebastian Steinlechner, Henning Vahlbruch, and Roman Schnabel. Squeezed light at 1550 nm with a quantum noise reduction of 12.3 dB. *Opt. Express*, 19(25):25763–25772, December 2011.

[33] Carlton M. Caves. Quantum-mechanical noise in an interferometer. *Phys. Rev. D*, 23(8):1693–1708, April 1981.

[34] The LIGO Scientific Collaboration. A gravitational wave observatory operating beyond the quantum shot-noise limit. *Nat Phys*, 7(12):962–965, December 2011.

[35] Kirk McKenzie, Daniel A. Shaddock, David E. McClelland, Ben C. Buchler, and Ping Koy Lam. Experimental Demonstration of a Squeezing-Enhanced Power-Recycled Michelson Interferometer for Gravitational Wave Detection. *Phys. Rev. Lett.*, 88(23):231102, May 2002.

[36] Carlton M. Caves. Quantum-Mechanical Radiation-Pressure Fluctuations in an Interferometer. *Phys. Rev. Lett.*, 45(2):75–79, July 1980.

[37] William G. Unruh. Quantum Noise in the Interferometer Detector. In Pierre Meystre and Marlan O. Scully, editors, *Quantum Optics, Experimental Gravity, and Measurement Theory*, number 94 in NATO Advanced Science Institutes Series, pages 647–660. Springer US, 1983.

[38] M. T. Jaekel and S. Reynaud. Quantum Limits in Interferometric Measurements. *EPL*, 13(4):301, October 1990.

[39] H. Kimble, Yuri Levin, Andrey Matsko, Kip Thorne, and Sergey Vyatchanin. Conversion of conventional gravitational-wave interferometers into quantum nondemolition interferometers by modifying their input and/or output optics. *Phys. Rev. D*, 65(2):022002, December 2001.

[40] Eugeniy Mikhailov, Keisuke Goda, Thomas Corbitt, and Nergis Mavalvala. Frequency-dependent squeeze-amplitude attenuation and squeeze-angle rotation by electromagnetically induced transparency for gravitational-wave interferometers. *Phys. Rev. A*, 73(5):053810, May 2006.

[41] Thomas Corbitt, Nergis Mavalvala, and Stan Whitcomb. Optical cavities as amplitude filters for squeezed fields. *Phys. Rev. D*, 70(2):022002, July 2004.

[42] Farid Khalili, Haixing Miao, and Yanbei Chen. Increasing the sensitivity of future gravitational-wave detectors with double squeezed-input. *Phys. Rev. D*, 80(4):042006, August 2009.

[43] Travis Horrom, Gleb Romanov, Irina Novikova, and Eugeniy E. Mikhailov. All-atomic generation and noise-quadrature filtering of squeezed vacuum in hot Rb vapor. *Journal of Modern Optics*, 60(1):43–49, January 2013.

[44] Neil V. Corzo, Quentin Glorieux, Alberto M. Marino, Jeremy B. Clark, Ryan T. Glasser, and Paul D. Lett. Rotation of the noise ellipse for squeezed vacuum light generated via four-wave mixing. *Phys. Rev. A*, 88(4):043836, October 2013.

[45] J. Laurat, T. Coudreau, G. Keller, N. Treps, and C. Fabre. Compact source of Einstein-Podolsky-Rosen entanglement and squeezing at very low noise frequencies. *Phys. Rev. A*, 70(4):042315, October 2004.

[46] Ulrich Vogl, Ryan Glasser, and Paul D. Lett. A compact source for quantum image processing with four-wave mixing in Rubidium-85. In *Complex Light and Optical Forces VI*, volume 8274, pages 82740C–82740C–6, 2012.

[47] Zhongzhong Qin, Jietai Jing, Jun Zhou, Cunjin Liu, Raphael C. Pooser, Zhifan Zhou, and Weiping Zhang. Compact diode-laser-pumped quantum light source based on four-wave mixing in hot rubidium vapor. *Opt. Lett.*, 37(15):3141–3143, August 2012.

[48] M. I. Kolobov and I. V. Sokolov. Spatial behavior of squeezed states of light and quantum noise in optical images. *Sov. Phys. JETP*, 69:1097, 1989.

[49] M. I. Kolobov and I. V. Sokolov. Multimode Squeezing, Antibunching in Space and Noise-Free Optical Images. *EPL*, 15(3):271, June 1991.

[50] Prem Kumar and Mikhail I. Kolobov. Degenerate four-wave mixing as a source for spatially-broadband squeezed light. *Optics Communications*, 104(4–6):374–378, January 1994.

[51] Mikhail I. Kolobov. The spatial behavior of nonclassical light. *Rev. Mod. Phys.*, 71(5):1539–1589, October 1999.

[52] Michal Irani and Shmuel Peleg. Improving resolution by image registration. *CVGIP: Graphical Models and Image Processing*, 53(3):231–239, May 1991.

[53] Mikhail I. Kolobov and Prem Kumar. Sub-shot-noise microscopy: imaging of faint phase objects with squeezed light. *Opt. Lett.*, 18(11):849–851, June 1993.

[54] Ivan V. Sokolov and Mikhail I. Kolobov. Squeezed-light source for superresolving microscopy. *Opt. Lett.*, 29(7):703–705, April 2004.

[55] O. Jedrkiewicz, Y.-K Jiang, E. Brambilla, A. Gatti, M. Bache, L. A. Lugiato, and P. Di Trapani. Detection of Sub-Shot-Noise Spatial Correlation in High-Gain Parametric Down Conversion. *Phys. Rev. Lett.*, 93(24):243601, December 2004.

[56] Eric Yao, Sonja Franke-Arnold, Johannes Courtial, Miles J. Padgett, and Stephen M. Barnett. Observation of quantum entanglement using spatial light modulators. *Opt. Express*, 14(26):13089–13094, December 2006.

[57] Wojciech Wasilewski, A. I. Lvovsky, Konrad Banaszek, and Czesław Radzewicz. Pulsed squeezed light: Simultaneous squeezing of multiple modes. *Phys. Rev. A*, 73(6):063819, June 2006.

[58] B. Jack, A. M. Yao, J. Leach, J. Romero, S. Franke-Arnold, D. G. Ireland, S. M. Barnett, and M. J. Padgett. Entanglement of arbitrary superpositions of modes within two-dimensional orbital angular momentum state spaces. *Phys. Rev. A*, 81(4):043844, April 2010.

[59] Miles Padgett, Jonathan Leach, Barry Jack, Mary J. Romero, Daniele Giovannini, Sonja Franke-Arnold, and Stephen M. Barnett. Spatial Light Modulators: Single-Photon, Spatial-Mode Analyzers. In *International Conference on Quantum Information*, OSA Technical Digest (CD), page QTuE2. Optical Society of America, June 2011.

[60] J. Romero, D. Giovannini, M. G. McLaren, E. J. Galvez, A. Forbes, and M. J. Padgett. Orbital angular momentum correlations with a phase-flipped Gaussian mode pump beam. *J. Opt.*, 14(8):085401, August 2012.

[61] Kentaro Wakui, Yujiro Eto, Hugo Benichi, Shuro Izumi, Tetsufumi Yanagida, Kazuhiro Ema, Takayuki Numata, Daiji Fukuda, Masahiro Takeoka, and Masahide Sasaki. Ultrabroadband direct detection of nonclassical photon statistics at telecom wavelength. *Sci. Rep.*, 4, April 2014.

[62] E. Brambilla, L. Caspani, O. Jedrkiewicz, L. A. Lugiato, and A. Gatti. High-sensitivity imaging with multi-mode twin beams. *Phys. Rev. A*, 77(5):053807, May 2008.

[63] Giorgio Brida, Lucia Caspani, Alessandra Gatti, Marco Genovese, Alice Meda, and Ivano Ruo Berchera. Measurement of Sub-Shot-Noise Spatial Correlations without Background Subtraction. *Phys. Rev. Lett.*, 102(21):213602, May 2009.

[64] Giorgio Brida, Ivo Pietro Degiovanni, Marco Genovese, Maria Luisa Rastello, and Ivano Ruo Berchera. Detection of multimode spatial correlation in PDC and application to the absolute calibration of a CCD camera. *Opt. Express*, 18(20):20572–20584, September 2010.

[65] G. Brida, M. Genovese, and I. Ruo Berchera. Experimental realization of sub-shot-noise quantum imaging. *Nat Photon*, 4(4):227–230, April 2010.

[66] Giorgio Brida, Marco Genovese, Alice Meda, and Ivano Ruo Berchera. Experimental quantum imaging exploiting multimode spatial correlation of twin beams. *Phys. Rev. A*, 83(3):033811, March 2011.

[67] Seth Lloyd. Enhanced Sensitivity of Photodetection via Quantum Illumination. *Science*, 321(5895):1463–1465, September 2008.

[68] Si-Hui Tan, Baris I. Erkmen, Vittorio Giovannetti, Saikat Guha, Seth Lloyd, Lorenzo Maccone, Stefano Pirandola, and Jeffrey H. Shapiro. Quantum Illumination with Gaussian States. *Phys. Rev. Lett.*, 101(25):253601, December 2008.

[69] E. D. Lopaeva, I. Ruo Berchera, I. P. Degiovanni, S. Olivares, G. Brida, and M. Genovese. Experimental Realization of Quantum Illumination. *Phys. Rev. Lett.*, 110(15):153603, April 2013.

[70] Michael A. Taylor, Jiri Janousek, Vincent Daria, Joachim Knittel, Boris Hage, Hans-A. Bachor, and Warwick P. Bowen. Subdiffraction-Limited Quantum Imaging within a Living Cell. *Phys. Rev. X*, 4(1):011017, February 2014.

[71] Chien-Hung Lu and Jason W. Fleischer. Quantitative Phase Imaging using Quantum Light. In *Imaging and Applied Optics 2014*, OSA Technical Digest (online), page DM4B.2. Optical Society of America, July 2014.

[72] C. Fabre, J. B. Fouet, and A. Maître. Quantum limits in the measurement of very small displacements in optical images. *Opt. Lett.*, 25(1):76–78, January 2000.

[73] Mikhail I. Kolobov and Claude Fabre. Quantum Limits on Optical Resolution. *Phys. Rev. Lett.*, 85(18):3789, October 2000.

[74] Mikhail I. Kolobov. Quantum limits of superresolution for imaging discrete subwavelength structures. *Opt. Express*, 16(1):58–66, January 2008.

[75] M. Lassen, V. Delaubert, C. C. Harb, P. K. Lam, N. Treps, and H. A. Bachor. Generation of Squeezing in Higher Order Hermite - Gaussian Modes with an Optical Parametric Amplifier. *Journal of the European Optical Society: Rapid Publications*, 1, June 2006.

[76] M. Lassen, V. Delaubert, J. Janousek, K. Wagner, H.-A. Bachor, P. K. Lam, N. Treps, P. Buchhave, C. Fabre, and C. C. Harb. Tools for Multimode Quantum Information: Modulation, Detection, and Spatial Quantum Correlations. *Phys. Rev. Lett.*, 98(8):083602, February 2007.

[77] M. Lassen, G. Leuchs, and U. L. Andersen. Continuous Variable Entanglement and Squeezing of Orbital Angular Momentum States. *Phys. Rev. Lett.*, 102(16):163602, April 2009.

[78] J. Janousek, K. Wagner, J.-F. Morizur, N. Treps, P. K. Lam, C. C. Harb, and H.-A. Bachor. Optical entanglement of co-propagating modes. *Nat Photon*, 3(7):399–402, July 2009.

[79] Benoît Chalopin, Francesco Scazza, Claude Fabre, and Nicolas Treps. Direct generation of a multi-transverse mode non-classical state of light. *Opt. Express*, 19(5):4405–4410, February 2011.

[80] C. F. McCormick, V. Boyer, E. Arimondo, and P. D. Lett. Strong relative intensity squeezing by four-wave mixing in rubidium vapor. *Opt. Lett.*, 32(2):178–180, January 2007.

[81] V. Boyer, C. F. McCormick, E. Arimondo, and P. D. Lett. Ultraslow Propagation of Matched Pulses by Four-Wave Mixing in an Atomic Vapor. *Phys. Rev. Lett.*, 99(14):143601, October 2007.

[82] Vincent Boyer, Alberto M. Marino, Raphael C. Pooser, and Paul D. Lett. Entangled Images from Four-Wave Mixing. *Science*, 321(5888):544 –547, July 2008.

[83] Quentin Glorieux, Luca Guidoni, Samuel Guibal, Jean-Pierre Likforman, and Thomas Coudreau. Quantum correlations by four-wave mixing in an atomic vapor in a nonamplifying regime: Quantum beam splitter for photons. *Phys. Rev. A*, 84(5):053826, November 2011.

[84] Neil Corzo, Alberto M. Marino, Kevin M. Jones, and Paul D. Lett. Multi-spatial-mode single-beam quadrature squeezed states of light from four-wave mixing in hot rubidium vapor. *Opt. Express*, 19(22):21358–21369, October 2011.

[85] A. M. Marino, J. B. Clark, Q. Glorieux, and P. D. Lett. Extracting spatial information from noise measurements of multi-spatial-mode quantum states. *Eur. Phys. J. D*, 66(11):1–9, November 2012.

[86] C. S. Embrey, M. T. Turnbull, P. G. Petrov, and V. Boyer. Observation of Localized Multi-Spatial-Mode Quadrature Squeezing. *Phys. Rev. X*, 5(3):031004, July 2015.

[87] N. Treps, U. Andersen, B. Buchler, P. K. Lam, A. Maître, H.-A. Bachor, and C. Fabre. Surpassing the Standard Quantum Limit for Optical Imaging Using Nonclassical Multimode Light. *Phys. Rev. Lett.*, 88(20):203601, May 2002.

[88] Mikhail I. Kolobov. *Quantum Imaging*. Springer, New York, October 2006.

[89] Mark Fox. *Quantum Optics: An Introduction*. Oxford University Press, USA, Oxford ; New York, June 2006.

[90] Simon Hooker and Colin Webb. *Laser Physics*. OUP Oxford, Oxford ; New York, August 2010.

[91] Hans-A. Bachor and Timothy C. Ralph. *A Guide to Experiments in Quantum Optics*. Wiley-VCH, Weinheim, 2nd, revised and enlarged edition edition edition, March 2004.

[92] A. Gatti, E. Brambilla, L. A. Lugiato, and M. I. Kolobov. Quantum Entangled Images. *Phys. Rev. Lett.*, 83(9):1763–1766, August 1999.

[93] Lu-Ming Duan, G. Giedke, J. I. Cirac, and P. Zoller. Inseparability Criterion for Continuous Variable Systems. *Phys. Rev. Lett.*, 84(12):2722–2725, March 2000.

[94] L. Lopez, S. Gigan, N. Treps, A. Maître, C. Fabre, and A. Gatti. Multimode squeezing properties of a confocal optical parametric oscillator: Beyond the thin-crystal approximation. *Phys. Rev. A*, 72(1):013806, July 2005.

[95] Simon Hooker and Colin Webb. Laser Physics: non-linear optics chapter. In *Laser Physics*, Oxford Master Series, pages 400–430. Oxford University Press, first edition edition, 2010.

[96] L. Lopez, B. Chalopin, A. Riviére de la Souchére, C. Fabre, A. Maître, and N. Treps. Multimode quantum properties of a self-imaging optical parametric oscillator: Squeezed vacuum and Einstein-Podolsky-Rosen-beams generation. *Phys. Rev. A*, 80(4):043816, October 2009.

[97] Liu Kui, Cui Shu-Zhen, Yang Rong-Guo, Zhang Jun-Xiang, and Gao Jiang-Rui. Experimental Generation of Multimode Squeezing in an Optical Parametric Amplifier. *Chinese Phys. Lett.*, 29(6):060304, June 2012.

[98] Matthew Turnbull. *Multi-spatial-mode quadrature squeezing from four-wave mixing in a hot atomic vapour*. Ph.D. Thesis, University of Birmingham, July 2014.

[99] Charles H. Bennett and Gilles Brassard. Quantum cryptography: public key distribution and coin tossing. *Proceedings of IEEE International Conference on Computers, Systems and Signal Processing, pp.*, December 1984.

[100] Charles H. Bennett. Quantum cryptography using any two nonorthogonal states. *Phys. Rev. Lett.*, 68(21):3121–3124, May 1992.

[101] Charles H. Bennett, Gilles Brassard, Claude Crépeau, Richard Jozsa, Asher Peres, and William K. Wootters. Teleporting an unknown quantum state via dual classical and Einstein-Podolsky-Rosen channels. *Phys. Rev. Lett.*, 70(13):1895–1899, March 1993.

[102] Horace P. Yuen and J.H. Shapiro. Optical communication with two-photon coherent states–Part I: Quantum-state propagation and quantum-noise. *IEEE Transactions on Information Theory*, 24(6):657–668, November 1978.

[103] Y. Yamamoto and H. A. Haus. Preparation, measurement and information capacity of optical quantum states. *Rev. Mod. Phys.*, 58(4):1001–1020, October 1986.

[104] Carlton M. Caves and P. D. Drummond. Quantum limits on bosonic communication rates. *Rev. Mod. Phys.*, 66(2):481–537, April 1994.

[105] C. D. Nabors and R. M. Shelby. Two-color squeezing and sub-shot-noise signal recovery in doubly resonant optical parametric oscillators. *Phys. Rev. A*, 42(1):556–559, July 1990.

[106] E. S. Polzik, J. Carri, and H. J. Kimble. Atomic spectroscopy with squeezed light for sensitivity beyond the vacuum-state limit. *Appl. Phys. B*, 55(3):279–290, September 1992.

[107] Wang Hai, Xie Changde, Pan Qing, Xue Chenyang, Zhang Yun, and Peng Kunchi. Optical Measurements of Weak Absorption Beyond Shot-Noise Limit. In O. Hirota, A. S. Holevo, and C. M. Caves, editors, *Quantum Communication, Computing, and Measurement*, pages 445–453. Springer US, 1997.

[108] Yong-qing Li, Peter Lynam, Min Xiao, and Paul J. Edwards. Sub-Shot-Noise laser Doppler Anemometry with Amplitude-Squeezed Light. *Phys. Rev. Lett.*, 78(16):3105–3108, April 1997.

[109] Matthew Pitkin, Stuart Reid, Sheila Rowan, and James Hough. Gravitational Wave Detection by Interferometry (Ground and Space). *Living Reviews in Relativity*, 14, 2011.

[110] N. A. Massie, editor. *Interferometric Metrology.* Society of Photo Optical, Bellingham, Wash., USA, June 1988.

[111] Eric Oelker, Tomoki Isogai, John Miller, Maggie Tse, Lisa Barsotti, Nergis Mavalvala, and Matthew Evans. Audio-band frequency-dependent squeezing. *arXiv:1508.04700 [physics, physics:quant-ph]*, August 2015. arXiv: 1508.04700.

[112] Pierre Meystre and Marian O. Scully, editors. *Quantum Optics, Experimental Gravity, and Measurement Theory.* Springer, New York, 1983 edition edition, July 1983.

[113] Eugene Hecht. Chapter 10.2. In *Optics*. Addison-Wesley, 4 edition edition, 2001.

[114] John William Strutt Rayleigh. *The Collected Optics Papers of Lord Rayleigh*. Optical Society of America, Washington, DC, January 1994.

[115] Mikhail I. Kolobov. Chapter 6: Quantum Limits of Optical Super-Resolution. In Mikhail I. Kolobov, editor, *Quantum Imaging*, pages 113–139. Springer New York, New York, NY, October 2006.

[116] Andrey N. Tikhonov and Vasiliy Y. Arsenin. *Solutions of Ill-posed Problems*. John Wiley & Sons Inc, Washington : New York, August 1977.

[117] D. Slepian and H. O. Pollak. Prolate Spheroidal Wave Functions, Fourier Analysis and Uncertainty — I. *Bell System Technical Journal*, 40(1):43–63, January 1961.

[118] B. Roy Frieden. VIII Evaluation, Design and Extrapolation Methods for Optical Signals, Based on Use of the Prolate Functions. In E. Wolf, editor, *Progress in Optics*, volume 9, pages 311–407. Elsevier, 1971.

[119] Ivan N. Agafonov, Maria V. Chekhova, and Gerd Leuchs. Two-color bright squeezed vacuum. *Phys. Rev. A*, 82(1):011801, July 2010.

[120] David J. Griffiths. *Introduction to Electrodynamics*. Addison Wesley, Upper Saddle River, N.J, 3 edition edition, December 1998.

[121] Christopher C. Davies. Lasers and Electro-Optics:-chapters on non-linear optics. In *Lasers and Electro-Optics*, pages 508–560. Cambridge University Press, fourth printing edition, 2006.

[122] Christopher C. Davis. *Lasers and Electro-optics: Fundamentals and Engineering: Written by Christopher C. Davis, 1996 Edition, Publisher: Cambridge University Press*. Cambridge University Press, May 1996.

[123] Daniel Steck. *Rubidium 85 D Line Data*. http://steck.us/alkalidata, revision 2.1.4 edition, December 2010.

[124] M. T. Turnbull, P. G. Petrov, C. S. Embrey, A. M. Marino, and V. Boyer. Role of the phase-matching condition in nondegenerate four-wave mixing in hot vapors for the generation of squeezed states of light. *Phys. Rev. A*, 88(3):033845, September 2013.

[125] M. D. Lukin, P. R. Hemmer, and M. O. Scully. Resonant Nonlinear Optics in Phase-Coherant Media. *Advances in Atomic, Molecular, and Optical Physics*, 42:347–386, 1999.

[126] Nicolas Treps, Nicolai Grosse, Warwick P. Bowen, Claude Fabre, Hans-A. Bachor, and Ping Koy Lam. A Quantum Laser Pointer. *Science*, 301(5635):940–943, August 2003.

[127] V. Boyer, A. M. Marino, and P. D. Lett. Generation of Spatially Broadband Twin Beams for Quantum Imaging. *Phys. Rev. Lett.*, 100(14):143601, April 2008.

[128] Rodney Loudon. The photon Intensity Operator: Chapter 4.11. In *The Quantum Theory of Light*, page 448. OUP Oxford, Oxford ; New York, 3 edition edition, September 2000.

[129] Rodney Loudon. Quantization of the Electromagnetic Field: Chapter 4.4. In *The Quantum Theory of Light*, page 448. OUP Oxford, Oxford ; New York, 3 edition edition, September 2000.

[130] Rodney Loudon. Quantum Theory of Direct Detection: Chapter 6.10. In *The Quantum Theory of Light*, page 448. OUP Oxford, Oxford ; New York, 3 edition edition, September 2000.

[131] R. Loudon and P.L. Knight. Squeezed Light. *Journal of Modern Optics*, 34(6-7):709–759, 1987.

[132] Alberto M. Marino, Jr. Stroud, C. R., Vincent Wong, Ryan S. Bennink, and Robert W. Boyd. Bichromatic local oscillator for detection of two-mode squeezed states of light. *J. Opt. Soc. Am. B*, 24(2):335–339, February 2007.

[133] L. A. Lugiato and Ph. Grangier. Improving quantum-noise reduction with spatially multimode squeezed light. *J. Opt. Soc. Am. B*, 14(2):225–231, February 1997.

[134] Lorenzo Adlai Sadun. *Topology of Tiling Spaces*. American Mathematical Society, Providence, R.I, October 2008.

[135] R. C. Pooser, A. M. Marino, V. Boyer, K. M. Jones, and P. D. Lett. Low-Noise Amplification of a Continuous-Variable Quantum State. *Phys. Rev. Lett.*, 103(1):010501, June 2009.

[136] N. V. Corzo, A. M. Marino, K. M. Jones, and P. D. Lett. Noiseless Optical Amplifier Operating on Hundreds of Spatial Modes. *Phys. Rev. Lett.*, 109(4):043602, July 2012.